Multi-mechanisms in proton-induced nucleon removal from ^{14}O at 94 MeV/nucleon

Vielfältige Mechanismen in der Proton induzierten Entfernung eines Nukleons von ^{14}O bei 94 MeV/Nukleon
Zur Erlangung des Grades eines Doktors der Naturwissenschaften (Dr. rer. nat.)
Genehmigte Dissertation von Thomas Pohl aus Hadamar
Tag der Einreichung: 15. November 2022, Tag der Prüfung: 19. Dezember 2022

1. Gutachten: Prof. Dr. A. Obertelli
2. Gutachten: Prof. Dr. T. Aumann
Darmstadt, 2. Auflage

TECHNISCHE
UNIVERSITÄT
DARMSTADT

Physics Department
Institut für Kernphysik
AG Obertelli

Multi-mechanisms in proton-induced nucleon removal from ^{14}O at 94 MeV/nucleon
Vielfältige Mechanismen in der Proton induzierten Entfernung eines Nukleons von ^{14}O bei 94 MeV/Nukleon

Accepted doctoral thesis by Thomas Pohl

Date of submission: 15. November 2022
Date of thesis defense: 19. Dezember 2022

Darmstadt, 2. Auflage

Bitte zitieren Sie dieses Dokument als:
URN: urn:nbn:de:tuda-tuprints-232460
URL: http://tuprints.ulb.tu-darmstadt.de/23246
Jahr der Veröffentlichung auf TUprints: 2023

Erklärungen laut Promotionsordnung

§ 8 Abs. 1 lit. c PromO

Ich versichere hiermit, dass die elektronische Version meiner Dissertation mit der schriftlichen Version übereinstimmt.

§ 8 Abs. 1 lit. d PromO

Ich versichere hiermit, dass zu einem vorherigen Zeitpunkt noch keine Promotion versucht wurde. In diesem Fall sind nähere Angaben über Zeitpunkt, Hochschule, Dissertationsthema und Ergebnis dieses Versuchs mitzuteilen.

§ 9 Abs. 1 PromO

Ich versichere hiermit, dass die vorliegende Dissertation selbstständig und nur unter Verwendung der angegebenen Quellen verfasst wurde.

§ 9 Abs. 2 PromO

Die Arbeit hat bisher noch nicht zu Prüfungszwecken gedient.

Darmstadt, 15. November 2022

T. Pohl

Zusammenfassung

Die Entfernung eines Nukleons von einem Atomkern ist ein starkes Werkzeug zur Untersuchung der Einteilchenstruktur. Durch Vermessen des übrigen Kerns kann der Bahndrehimpuls von dem entfernten Nukleon bestimmt werden. In den letzten Jahrzehnten wurde systematische Studien über die Reduzierung der Einzelteilchenstärke und der parallelen Impulsverteilung des entfernten Nukleons durchgeführt. Eine asymmetrische Impulsverteilung und Diskrepanzen zwischen den gemessen und vorhergesagten Wirkungsquerschnitten, im speziellen der stark gebundenen Nukleonen, zeigten, dass der Reaktionsmechanismus noch weiter verstanden werden muss. Bei theoretischen Studien mit einem Protontarget bei 100 MeV/Nukleon kam heraus, dass die asymmetrische Verteilung von der Interaktion des übrig gebliebenen Kerns mit den anderen Teilchen, die den Kern verlassen, stammt. Eine Bestätigung dieser theoretischen Ergebnisse würde die Bedeutung der Endzustandinteraktion bestätigen. Jedoch wurde ein Großteil der experimentellen Daten mit leichten Ionentargets aufgenommen und es gibt keine Daten mit Protonentargets in diesem Energiebereich.

Deswegen wurde die Reaktion bei der ein Nukleon von einem ^{14}O Kern mit einem Wasserstofftarget bei 100 MeV/Nukleon durchgeführt. Der ^{14}O Kern hat eine große Asymmetrie in der Protonen- und Neutronen-Separationsenergie von $S_n - S_p = 18.55(1)$ MeV. Der ^{14}O Sekundärstrahl ist auf ein 2.4 mm dickes Target aus festem Wasserstoff aufgetroffen. Die daraus resultierenden Fragmente wurden mit dem SAMURAI Spektrometer gemessen. Im speziellen waren die Rückstände ^{13}O and ^{13}N von Interesse. Der gemessene inklusive Wirkungsquerschnitt und die parallele Impulsverteilung (PMD) werden mit theoretischen Berechnungen verglichen. Inelastische Steuung, distorted-wave impule approximation und Quanten-Transfer zum Kontinuum werden für die theoretischen Berechnungen berücksichtigt. Spektroskopische Faktoren vom Schalenmodell werden für den Vergleich mit den experimentellen Daten verwendet. Eine symmetrische Verteilung wird für die Entfernung eines Protons beobachtet, für welche der (p,pn) Abschlag und (p,p') inelastische Kanal zu fast gleichen Teilen beitragen. Bei der Entfernung eines Neutrons ergibt sich eine stark asymmetrische Verteilung, welche durch die Kombination von den Ergebnisse aus (p,pn) Abschlag und (p,d) Transfer rekonstruiert werden kann. Die Reduktion der Einzelteilchenstärke wird mit dem Reduktionsfaktor quantifiziert, welche durch das Verhältnis von experimentellen zu theoretischem Wirkungsquerschnitt definiert ist. Die Reduktionsfaktoren R_s können bestimmt werden und werden mit Ergebnissen aus Schwerionen Abschlag- und Transferreaktionen verglichen. Die Ergebnisse dieser Arbeit zeigen, dass die Proton induzierte Entfernung eines Nukleons von seltenen Isotopen bei Energien von ~ 100 MeV/Nukleon viele Reaktionsmechanismen auslöst, darunter quasi-freie Streuung, inelastische Streuung und Transfer.

Abstract

The one-nucleon removal reaction from nuclei is a strong tool to investigate the single-particle structure. From the measurement of the residual nucleus, the orbital angular momentum of the removed nucleon can be determined. In the last decades, systematic studies on the quenching of the single-particle strength and the parallel momentum distribution of the removed nucleons have been performed. Asymmetric momentum distributions and discrepancies between measured cross sections and predictions, in particular for the deeply-bound nucleons, demonstrated, that the reaction mechanism needs to be further understood. From theoretical studies with a proton target at 100 MeV/nucleon the asymmetric distribution is attributed to stem from the interaction of the outgoing particles with the residual core nucleus. A confirmation of these theoretical results would emphasize the significance of the final state interactions. However, most of the experimental data was taken with light-ion targets and there is no data with proton targets in this incident-energy region.

This is why the one-nucleon removal reaction from ^{14}O at 94 MeV/nucleon from a hydrogen target was performed. The nucleus ^{14}O has a large asymmetry in proton and neutron separation energies $S_n - S_p = 18.55(1)$ MeV. The ^{14}O secondary beam was impinged on a 2.4 mm thick solid hydrogen target. The resulting fragments were measured with the SAMURAI spectrometer. In particular, the one-nucleon removal residues ^{13}O and ^{13}N are of interest. Their measured inclusive cross sections and parallel momentum distributions (PMDs) are compared to theoretical calculations. Inelastic scattering, the distorted-wave impulse approximation and quantum transfer to the continuum are considered for theoretical calculations. Shell-model spectroscopic factors are applied for the comparison with the experimental data. A symmetric shape is observed for the proton removal channel, for which the (p,2p) knockout and the (p,p') inelastic channel are found contributing almost equally. The neutron removal channel exhibits a strongly asymmetric PMD, which is reproduced well by combining the results from (p,pn) knockout and (p,d) transfer. The quenching of the single-particle strength is quantified by the reduction factor R_s, which is defined by ratio of the experimental to the theoretical cross section. The reduction factors R_s are obtained and are compared to heavy-ion induced knockout and transfer reaction results. The results of this work show that the proton-induced nucleon removal from rare isotopes at energies of ~ 100 MeV/nucleon originates in several reaction mechanisms, including quasi-free scattering, inelastic scattering and transfer.

Acknowledgement

Here, I would like to thank everyone, who accompanied and supported me on my path to make this thesis possible. In particular, I would like to highlight the following persons:

- Alexandre Obertelli as my supervisor, who gave me the opportunity for this thesis in his group and for his advice, guidance and support over the last years.
- Yelei Sun, who started as my co-supervisor and became a friend for me on this journey. I will be forever grateful for everything you taught me about data analysis, programming in nuclear physics and the basics of scientific writing. Your guidance and advices in the analysis were of immeasurable value.
- Mario Gómez Ramos, Kazuyuki Ogata and Kazuki Yoshida for the theoretical calculations for my data and the various discussions over the interpretation. Without you the nice conclusions of this work would not be possible.
- Hongna Liu and Yuki Kubota for their discussions and input on the analysis, when there was an issue.
- Yelei Sun, Isabelle Brandherm and Sebastian Kloth for proofreading the drafts of this thesis and Mario Gómez Ramos for proofreading the draft of the theory section.
- Giovanna Umberti Caroli, Catja Noll, Carina Seeger, Ute Hasenzahl und Astrid Link for solving every organizatoric issue over the last years.
- My family and friends, who were there for me the last years during my studies. Especially my parents, who always supported me in any situation.
- The members of the AG Obertelli, former and present, for a nice working group environment and the time spent together. In particular Alexander Schmidt, Jonas Fischer and Clara Klink for the comfortable working environment.
- Prof. Dr. Thomas Aumann for agreeing to be the second reviewer of this thesis.
- Prof. Dr. Robert Roth and Prof. Dr. Regine von Klitzing to be examiners during my defense.
- This work was supported by the Deutsche Forschungsgemeinschaft (DFG, German Research Foundation) - Projektnummer 279384907-SFB 1245.

Contents

List of Figures

List of Tables

Introduction

1. Context of this Work

The structure of the nucleus and the interaction of its constituents is an interesting and manifold topic. Its exploration started as early as 1911, when Rutherford did one of the most famous nuclear physics experiments, the scattering of α-particles on a gold foil. Still over 100 years later, the nucleus is not yet fully understood despite massive scientific efforts and progress in nuclear physics. In the past, models have been developed to successfully describe stable nuclei. However, these models failed to describe the properties of unstable nuclei, which again started to question our understanding of the nucleus. It is a present topic to describe the complexity of the nucleus and the interaction between nucleons correctly. This work tries to deliver a small but significant contribution in the exploration of the nucleus with direct reactions. The central topic of this thesis is the one-nucleon removal reaction from ^{14}O at 94 MeV/nucleon with a 2.4-mm thick solid hydrogen target. To put this work into the context of nuclear physics, a brief introduction on *nuclear structure*, the exploration and quantification of properties of a nucleus and nucleons with *direct reactions* and *recent experimental and theoretical results* will be given in the following.

1.1. Structure of Nuclei

In the past, much progress has been made to successfully describe the properties of stable nuclei with well established models. One of the first models, which has been used to describe the nucleons inside the nucleus, is the Fermi-Gas model [1]. Here, the neutrons and protons are described as independent systems. They fill energy levels separately according to the Fermi-Dirac statistics and restricted by Pauli blocking. Afar from these restrictions, it is assumed, that a nucleon can move freely inside the volume of the nucleus. This is described as well potential generated by all nucleons. The model is successful in explaining many basic phenomena, e.g. binding energies, the surplus of neutrons in heavy nuclei, etc.. However, the Fermi-Gas model is not able to describe the occurrence of very stable nuclei at certain number of protons and/or neutrons. These special numbers are 2, 8, 20, 28, 50, 82, 126 and referred to as *magic numbers*. An explanation for those numbers was found with the suggestion of the shell model[2, 3]. It introduces energy levels as shells, which are occupied by the nucleons and separated from other shells. The different energy levels originate from the radial position and the angular orientation of the particles in the nucleus. The first successful potential to describe the energy levels was the Woods-Saxon potential [4]. Furthermore, the coupling of spin and orbit is necessary to describe magic numbers from 28 and higher. The shell model describes nuclei with magic numbers and neighboring nuclei with one nucleon more or less very well. The maximum occupancy of an energy level is $(2j + 1)$, where j is total angular momentum. In this simplest version, the shell model with the spin-orbit extension and the mean field approach is often referred to as independent particle model (IPM). The name stems from the key property, that the nucleons do not interact with each other, thus there are no correlations among nuclei included in this model. A level scheme including the spin-orbit coupling and a listing of the magic numbers is given in Fig. 1.1. From the figure it becomes obvious, that magic numbers arise at shell closures with a large energy gap to the next shell. There are extension of this model such as the interacting shell model (ISM)[5], where the residual interaction between nucleons in the valence space is involved.

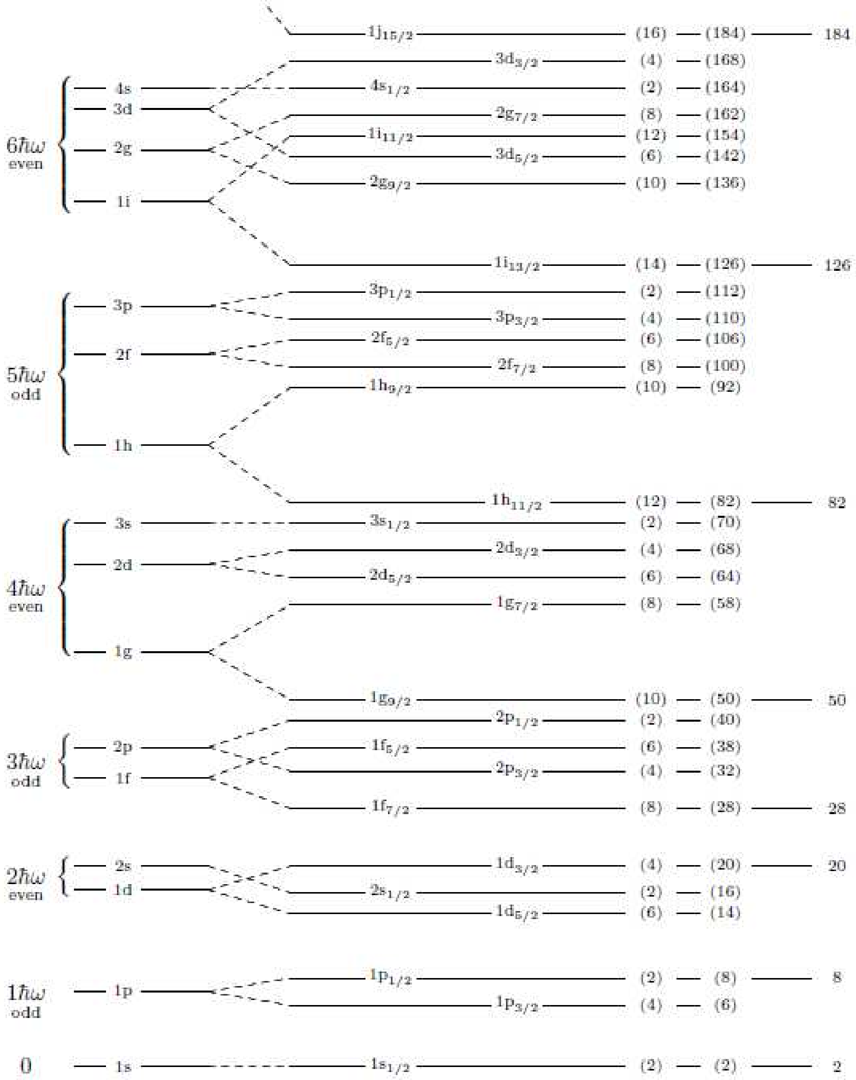

Figure 1.1.: Level scheme of the shell model showing the single-particle orbitals. The break of the degeneracy is due to the spin-orbit coupling. The magic numbers are the result of shell closures. Figure from Ref. [6].

Neutrons and protons can only be added up to a certain threshold, which is referred to as *dripline*. Nuclei beyond the *dripline* are unbound and decay via nucleon emission. It was soon found out, that systems with a large amount of neutrons or protons have a different structure than stable nuclei. This is clearly observed when magic numbers disappear and new ones arise, such as N = 16 [7]. This change of nuclear shell structure for exotic nuclei is called *shell evolution*. Apparently, the models and calculations, which were successful in the past for stable nuclei, are insufficient to describe exotic nuclei and thus question the understanding of the nucleus and the interaction between its constituents.

With the advance of modern nuclear physics facilities the investigation of exotic nuclei, nuclei with a large excess of either neutrons or protons, in inverse kinematics became possible. The first observation of a change compared to stable nuclei was found in the inversion of energy levels in the isotones for N = 7 and N = 9 [8, 9]. For the nuclei ^{11}Be, ^{12}B and ^{13}C it was shown, that the $s_{1/2}$- and $p_{1/2}$-orbitals are inverted and for the nuclei ^{15}C, ^{16}N and ^{17}O the inversion of the $s_{1/2}$- and $d_{5/2}$-orbitals was proven. The change was mainly attributed to the monopole drift, which later has been confirmed to be one of the driving forces for shell evolution.

The effect of the monopole drift was further studied [10–13]. The shell structure changes through the monopole interaction, which itself depends on the neutron or proton richness of a nucleus. Eq. (1.1) is the potential for the monopole interaction. The nominator averages the effect of an interaction V over all possible orientation normalized by the denominator. Orientation in this context means the various combination of the different magnetic momenta m and m' from the total angular momenta j and j'.

$$V^T_{j,j'} = \frac{\sum_j (2J+1)\langle (jj')JT|V|(jj')JT\rangle}{\sum_j (2j+1)} \tag{1.1}$$

The shift of the new effective single particle energies (ESPE) can be calculated with Eq. (1.2) using the determined $V^T_{j,j'}$ from Eq. (1.1). In Eq. (1.1) $n_n(j')$ is the occupation probability of the neutron in the j' orbit.

$$\epsilon_p(j) = \frac{1}{2}(V^{T=0}_{j,j'} + V^{T=1}_{j,j'} n_n(j')) \tag{1.2}$$

Depending on the isospin, the monopole interaction is more or less strong. For an isospin of $T = 0$ the central force is much stronger than for the isospin $T = 1$. This means, that the coupling is much stronger between pn orbitals, than for pp or nn orbitals. The central force acts always attractive. However, if the total interaction is attractive or repulsive is decided by the tensor force. The tensor force adds an attractive contribution for the coupling of $j_>(j'_>)$ and $j'_<(j_<)$ and a repulsive contribution for the coupling of $j_>(j'_<)$ and $j'_>(j_<)$ orbitals. Here, the index $>$ and $<$ indicates, if the spin quantum number s of the orbital is $+1/2$ or $-1/2$. Thus, for a large occupation number of the neutron orbit $j'_>$, the proton orbit $j_<$ is bound stronger and the $j_>$ is bound weaker.

An example for the monopole drift are the nuclei ^{62}Ni and ^{54}Ca. The level schemes of the nuclei are shown in Fig. 1.2. The levels of ^{62}Ni are consistent with the shell structure for stable nuclei in Fig. 1.1. Due to the deficiency of protons or a surplus of neutrons in ^{54}Ca a strong attractive interaction between the $1f_{7/2}$ proton and the $1f_{5/2}$ neutron orbit arises, because the central and tensor force contribute additively. The energy levels rearrange, so that new magic numbers arise such as 32 and 34 in this case.

An other important phenomenon in shell evolution is the importance of three-body forces. As an example, its significance can be shown in the prediction of the oxygen dripline. For a long period

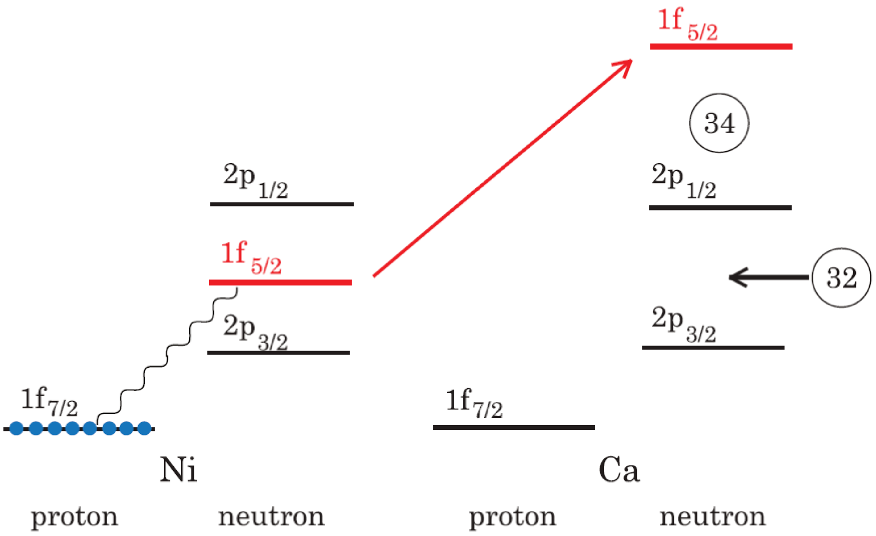

Figure 1.2.: Schematic illustration of shell evolution from ^{62}Ni to ^{54}Ca for neutron orbits. The wavy line implies the interaction between the proton $1f_{1/2}$ and the neutron $1f_{5/2}$ orbit. The blue circles are protons. The numbers in circles indicate the new magic numbers. Figure from Ref. [12].

of time, theory was unable to explain the experimental results. Recently, the dripline has been successfully predicted by the ab initio coupled cluster model approach with three-body forces [14]. The nucleon-nucleon interaction in this work is computed with the modern chiral effective field theory. The binding energies, excited states and radii of the oxygen isotopes are calculated. From the results it became evident, that three-nucleon forces and the particle continuum are crucial for the description of neutron-rich nuclei.

The modern approach for the treatment of the two- and three-body interaction is the chiral effective field theory (ChEFT) [15–17], which has been already mentioned in the previous paragraph. It is conceptional and qualitatively superior to the traditional approaches, which base on the meson exchange model and realistic NN-potentials. While the traditional approaches are mostly phenomenological, the ChEFT is derived ab initio based on the QCD. It is defined on a separated scale with degrees of freedom appropriate for low energy nuclear physics. The Lagrangian is constructed, so that all symmetries and symmetry breakings of the quantum chrono dynamics are fulfilled. A systematic extension of the interaction is possible. The accuracy can be improved by calculating the next order of the extension when necessary. Furthermore, three- and four-body forces develop consistently from the extension.

Modern approaches to solve the Schrödinger equation can be divided in two categories: ab initio and approximation models. The exact solution of the Schrödinger equation by ab initio methods has been developed during the recent decades with the advance of computational power. Two of the major representatives are the No-Core Shell Model (NCSM) [18] and Quantum Monte Carlo (QMC) method [19, 20]. However, due to the exponential rise of complexity with every additional nucleon, calculations are only possible up to nuclei with the mass number $A \leq 16$. For the calculation of heavier nuclei, models with approximations are necessary, which reduce the many-body Hilbert space. Here, two examples are the interacting shell model (ISM) [5] and self-consistent Greens function (SCGF) [21].

1.2. Direct Reactions

One possible way to classify nuclear reactions is in *compound* and *direct* reactions. In compound reactions, an intermediate system is produced and decays after some time with no information on the structure of the colliding nuclei left. In direct reactions, the reaction takes place between few nucleons of the projectile and the target. The reaction process takes only a few steps. Ideally, only the reacting nucleons are involved. Therefore, the reaction has to be peripheral and happens in a very short time of about 10^{-22} s (this is roughly the time, a projectile needs to pass the target nucleus). Due to these boundary conditions of direct reactions, it is possible to extract information on the original state of the nucleus by measuring the reaction products. The final state keeps part of the information of the initial wave function.

In the following it is shown, how direct reactions are used as a tool to investigate the shell structure using the quasi-free scattering assumption (QFS). Reactions under the QFS assumption are considered as one of the cleanest mechanisms. Fig. 1.3 shows a scheme of the process. A projectile (red) approaches the target nucleus A. The target nucleus consists of the core C and a nucleon N (blue). The nucleon N has the momentum $\vec{p}_n$ and due to momentum conservation the core must have the momentum $\vec{p}_C = -\vec{p}_n$. During the nucleon removal reaction only the projectile and nucleon N are interacting, which leaves the momentum of the core C unaltered. By measuring $\vec{p}_C$ one can then determine the momentum of the nucleon $\vec{p}_n$.

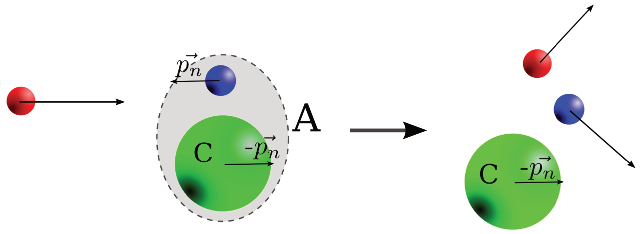

Figure 1.3.: (p,pN) reaction under the quasi-free scattering assumption. A projectile (red) approaches the target nucleus A. The target nucleus consists of the the core C and a nucleon N (blue). Figure from Ref. [22].

The extracted momentum distribution is then compared to theoretical single-particle removal calculations from a well-defined energy level. The momentum distribution is sensitive to the quantum numbers, especially to the orbital angular momentum, as is shown in Fig. 1.4. Here, the results of the nucleon removal reaction from ^{12}Be at 78 MeV/nucleon are given and one can clearly identify the two different states $1/2^+$ and $1/2^-$ from the distributions.

Naturally, that there is no interaction with the core is always an approximation, since the removed nucleon is bound in the nucleus in the first place. However, it is an indicator, which quantities have to be minimized or maximized for an experiment. The interaction of the projectile with the core has to be kept as low as possible, while at the same time the interaction with the removed nucleon must be strong. Light projectiles are the ideal candidate for this condition, since their interaction with the core should be small.

Another property, which can be minimized, is the final state interaction (FSI). It is the interaction between the removed nucleon and the core after the reaction. The nucleon-nucleon interaction has a minimum at several hundred MeV [24] and thus it is the preferred energy region for nucleon removal reactions. The ideal energy for the QFS condition is between 400 MeV and 700 MeV. However, it takes much effort to accelerate heavy nuclei to these energies. Only very few facilities are capable of this and so reactions are often performed at lower energies around 50 MeV - 200 MeV. Since this energy

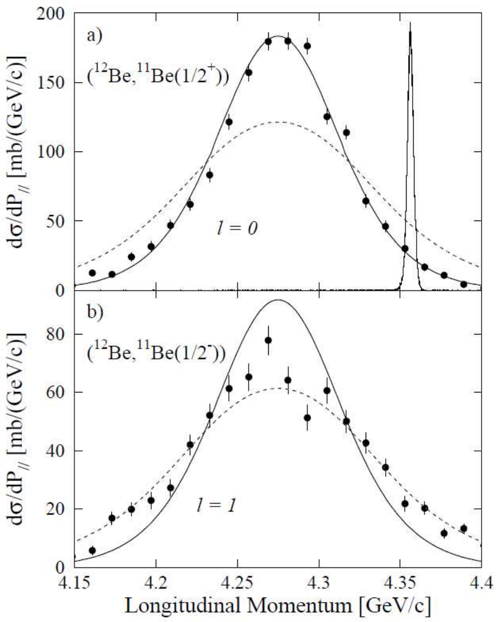

Figure 1.4.: Results of the nucleon removal from ^{12}Be at 78 MeV/nucleon. From the momentum distribution the two different states 1/2^{+} and 1/2^{-} of ^{11}Be can be identified. Figure from Ref. [23].

regime is clearly below the ideal QFS energy, an exact treatment of the above mentioned FSI becomes very important.

The minimization of the FSI also suggests the reaction mechanism to be peripheral. If the reaction would take place close to the core, the FSI naturally would be stronger. On its way out the nucleon would have more time to interact with the core.

1.3. Study of Stable Nuclei

Starting in the 1960s, (e,e'p) [25] and (p,pN) [26] reactions have been extensively studied as they are the ideal tool to extract single-particle properties from nuclei under the previous described circumstances. (e,e'p) reactions excel in smaller distortions on the removed nucleon. Electrons interact dominantly via the electromagnetic force with the nucleus. However, this means, that the interaction with the proton, which needs to be removed, is also weak. The removal of the proton has a small probability and thus high luminosities are necessary for compensation. Therefore, only experiments with stable targets have been possible so far. For the examination of unstable nuclei a beam of unstable nuclei has to be matched with an electron beam. There are plans to carry out such experiments in future campaigns [27]. On the other hand, in (p,pN) reactions the projectile proton interacts also via the strong interaction with the core and the nucleon to be removed. Thus, the cross section for the reaction is larger, but the distortion effects are stronger, too. It is possible to carry out reactions with stable and unstable nuclei. In this section, the focus is first on the results from experiments with stable targets. The study of unstable nuclei will be discussed in the next section.

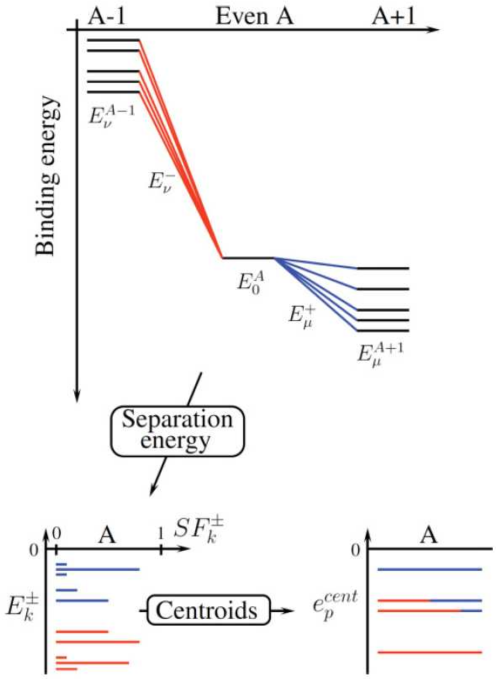

Figure 1.5.: Top: Total binding energies of three successive nuclei and associated one-nucleon addition and removal energies from the ground state of the initial system. Bottom left: spectral strength distribution. Bottom right: Single-particle energies from the centroid of the spectral strength distribution using Eq. (1.3). Figure from Ref. [28].

The main goal of (e,e'p) and (p,pN) is to study the structure of nuclei. Spectroscopy and information on the nucleon orbitals involved in the structure of nuclear states are important to understand the nuclear structure. The so called single particle energies predicted by the IPM can be calculated with the formula of Baranger [29]:

$$e_p = \frac{\sum_k S_k^{p+}(E_k - E_0) + S_k^{p-}(E_0 - E_k)}{\sum_k S_k^{p+} + S_k^{p-}} \quad . \tag{1.3}$$

Here, S_k^{p+} (S_k^{p-}) are the spectroscopic factors for the population of a final state k after the annihilation (creation) of a nucleon with the quantum numbers $p = nl$. To calculate the single-particle energies e_p, the E_k and S_k need to be determined experimentally.

Loosely speaking, the spectroscopic factor describes the probability of populating a certain state. Its definition for nucleon removal (+) and adding a nucleon (−) is as follows,

$$\begin{aligned} S_k^{p+} &= |\langle \Psi_0^A | a_p | \Psi_k^{A+1} \rangle|^2 \\ S_k^{p-} &= |\langle \Psi_0^A | a_p^\dagger | \Psi_k^{A-1} \rangle|^2 \end{aligned} \tag{1.4}$$

with $|\Psi_k^{A\pm1}\rangle$ being the wave function of the nucleus in state k consisting of $A \pm 1$ nucleons and a_p ($a_p^\dagger$) is the operator for the annihilation (creation) of a nucleon. If there would be no correlations between nucleons, the spectroscopic factor would be either 0 or 1 and the single-particle energies could be directly extracted from the separation energy of single nucleon excitations. In a real nucleus there are correlations between nucleons, so that a nucleon addition or removal reaction leads to a population of several states in the residue. This case is illustrated in Fig. 1.5 [28]. Here, the different separation energies to several states are given. The spectral strength distribution is calculated from the distribution onto the different states. Effective single-particle energies can then be obtained from the centroid of the spectral functions using Eq. (1.3). In general, the spectroscopic factors are extracted from direct reactions, where the cross sections from singular final states are determined.

For the quantification of the population of the single-particle states the reduction factor R_s is used. It is defined by the experimental σ_{exp} and theoretical σ_{th} cross section:

$$R_s = \frac{\sigma_{\text{exp}}}{\sigma_{\text{th}}} \ . \tag{1.5}$$

The calculation of the theoretical cross section is done using the following equation:

$$\sigma_{\text{th}} = \frac{A}{A-1} \cdot C^2 S \cdot \sigma_{\text{s.p.}}(\theta, E) \ . \tag{1.6}$$

Here, A is the atomic mass number, C the Clebsch-Gordan coefficient, S the spectroscopic factor and $\sigma_{\text{s.p.}}$ the single-particle cross section. $A/(A-1)$ is a center of mass correction factor. The Clebsch-Gordon coefficients are used to describe the coupling of spin-orbit interaction and the isospin formalism of the original and final state. The spectroscopic factor was introduced beforehand and is usually determined experimentally. The single-particle cross section is calculated from theoretical models. Some reaction models are introduced in Section 1.4 and the calculation is described within the section.

By comparing the experimental cross section from (e,e'p) reactions with theoretical results from the IPM, it was found, that the occupation of the levels is smaller than the predicted $(2j + 1)$. This reduction is often referred to as ”quenching”. It is shown in Fig. 1.6 [30], that the quenching is about 30 % - 40 %.

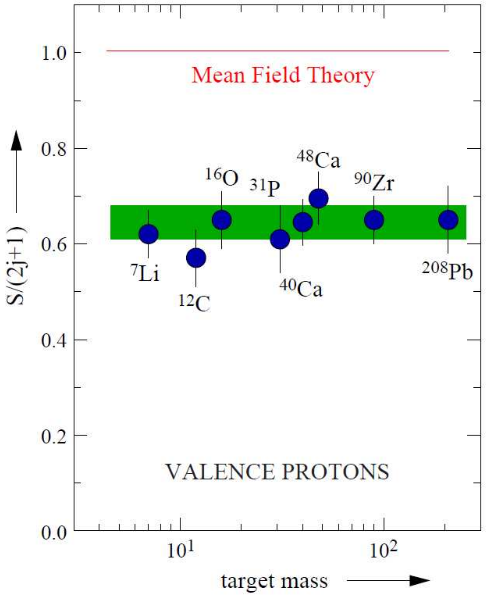

Figure 1.6.: Data of (e,e'p) reactions from stable nuclei [30]. Figure from Ref. [21].

The IPM is apparently not sufficient to describe the experimental data correctly, since it describes the average force on one nucleon with a mean field potential. It does not take into consideration, that there are correlations, which are not described by a mean field. These interactions lead to correlations between the nucleons, which induces a coupling of single-particle states. This coupling is the reason for reducing the occupancy of single-particle states below the Fermi energy ϵ_F. The Fermi energy is defined by the least bound nucleon in the nucleus. The removed nucleons are transferred to and occupy energy levels above the Fermi energy [31]. Fig. 1.7 shows the occupation probability and quasi-hole strength for nuclear matter and ^{208}Pb [32]. The correlated nucleons account for the whole occupation probability above the Fermi energy ϵ_F and also contributes partly to the occupation below the Fermi energy. Therefore, the quasi-hole strength is significantly smaller then the total occupation probability.

The correlations can be divided into short range correlations (SRC) and long range correlations (LRC). SRC couple the low energy states with the high energy states and originate from the strong tensor term and repulsive core of the nucleon-nucleon interaction. They contribute about 15 % to the quenching. LRC are due to the collective motion of the nucleons, which couple a single-particle motion to the motion of low lying states of the nucleus. They add another 20 %, so that the total quenching is about 35 % [21].

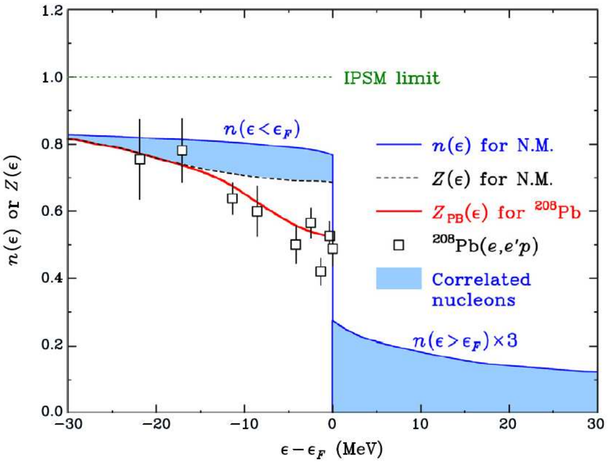

Figure 1.7.: Occupation probabilities $n(\epsilon)$ and quasi-hole strength $Z(\epsilon)$ for nuclear matter (N.M.) and ^{208}Pb. The blue shaded area is the contribution from the correlated nucleons. The experimental values of ^{208}Pb are shown as squares and the theoretical calculation for ^{208}Pb as red line. Figure from Ref. [32].

1.4. Study of Exotic Nuclei

In the last decades, nucleon removal experiments with various exotic nuclei at a large range of beam energies have become possible. A nucleus is called exotic, when it is has a large excess of one nucleon species, either neutrons or protons. Those nuclei are in general unstable and decay fast via β-decay. Nucleons of one species can only be added to a nucleus up to a certain threshold before it becomes unbound. This threshold is referred to as *dripline*. Adding nucleons beyond the dripline will not form bound nuclei and the system will decay fast via the strong interaction. One key property of exotic nuclei is, that the difference of the nucleon separation energies ΔS can be very large. It is defined as $\Delta S = S_p - S_n$ for proton removal and $\Delta S = S_n - S_p$ for neutron removal with $S_{n,p}$ being the neutron and proton separation energies. While in neutron-rich nuclei the neutrons are rather loosely-bound with a separation energy S_n of a few MeV, the separation energy S_p of the proton can be up to 20 MeV. For nuclei with a similar amount of neutron and protons ΔS is close to 0 as for the stable nuclei. Naturally, for proton-rich nuclei the opposite is the case. These extremes in separation energy make exotic nuclei an excellent probe to benchmark theoretical calculations, which themselves can depend on various assumptions and simplifications. It is possible to investigate, on which occasions assumptions are justified or when they fail to describe properties of nuclei.

The use of exotic nuclei is technically more difficult compared to stable nuclei, since experiments can only be performed in inverse kinematics due to their short life times. In inverse kinematics the exotic nuclei are produced in-flight from a stable ion beam by fragmentation. The fragmentation process allows only exotic beams with a small luminosity. The resulting beam is impinged on a target, which can be a light-ion target, such as ^{9}Be or ^{12}C, a carbon-hydrogen target or a proton target.

The two typical direct reaction processes to study exotic nuclei are transfer and knockout reactions, which have been already successfully applied in the past. The key properties and some recent results of those two reaction mechanism will be presented.

1.4.1. Knockout Reactions

The most popular probe for the study of exotic nuclei since the 90s has been knockout reactions. They are easier to perform, because they are carried out at higher energies than transfer reactions (see the following section). Due to the higher energies thicker targets can be used, which enhances the extraction of the cross section. When gamma-spectroscopy is applied, high resolution spectroscopy can still be performed. Thus, they can be used to study various exotic nuclei systematically.

Similar to the (e,e'p) and (p,2p) reactions with stable nuclei presented in the previous section, a nucleon is removed from the nucleus of interest A and the residual core $A-1$ is measured. The momentum of the nucleon can be reconstructed under the QFS as explained in Section 1.2. For knockout reactions, light-ion targets such as ^{9}Be and ^{12}C are used. They are easily to produce and have a low atomic number Z. The low Z guarantees that the interaction via the Coulomb force is reduced. In recent and future campaigns [33, 34], pure proton targets are used to reduce possible structure distortions from the light-ion targets. However, the production of the target is much more elaborated. The hydrogen needs to be liquified (21.15 K) or solified (14.01 K) to get a higher density for obtaining a reasonable cross section.

The reactions are performed at around 100 MeV/nucleon and occur on the surface of the nucleus. Therefore, two approximations are often applied in the theoretical description. The first one is the *sudden approximation*. It is assumed, that the reaction takes place in a single step in a very short time. Only the removed nucleon and the target do interact during the process. The remaining core is only spectating the reaction and does not change its state or momentum. The second approximation is the *eikonal approximation*. Here, the participants of the reactions follow straight lines. Especially the spectator core does not change its trajectory and leaves the target at forward scattering angles. This assumption is well justified for high energies and low Z target, because then the Coulomb interaction does not disturb the trajectory much. In addition, it assumes that there is no strong interaction between the projectile and the target. This is justified, because strong interaction would lead to absorption and thus is not measured. The two approximations simplify the theoretical calculation and are applied in Section 4.1, where a summary of the theoretical frameworks is presented.

The single-particle cross section $\sigma_{s.p.}$ from knockout reactions is calculated with Eq. (1.7). It is the sum of two components: an inelastic $\sigma^{\mathrm{inel}}_{s.p.}$ (stripping) and elastic $\sigma^{\mathrm{el}}_{s.p.}$ (diffraction) component. The two components can be calculated using Eq. (1.8) and Eq. (1.9). Here, $S = S_n S_c$ is the product of the elastic scattering matrices with S_n being the removed nucleon-target matrix and S_c the residue-target matrix. The other variables are defined as follows: j is the quantum number of the allowed angular momentum transfers, $\vec{b}$ is the impact parameter, ψ_{jm} is the wave function of the removed nucleon and $\delta_{m,m'}$ is the Kronecker delta.

$$\sigma_{s.p.} = \sigma_{s.p.}^{\text{inel}} + \sigma_{s.p.}^{\text{el}} \tag{1.7}$$

$$\sigma_{s.p.}^{\text{inel}} = \frac{1}{2j+1} \int d\vec{b} \sum_m \langle \psi_{jm} | (1 - |S_n|^2) |S_c|^2 | \psi_{jm} \rangle \tag{1.8}$$

$$\sigma_{s.p.}^{\text{el}} = \frac{1}{2j+1} \int d\vec{b} \sum_{m,m'} \left[\langle \psi_{jm} | |1 - S|^2 | \psi_{jm} \rangle \delta_{m,m'} - |\langle \psi_{jm'} | (1 - S) | \psi_{jm} \rangle|^2 \right] \tag{1.9}$$

$\sigma_{s.p.}^{\text{inel}}$ and $\sigma_{s.p.}^{\text{el}}$ are the single-particle cross sections of the two independent nucleon-removal processes, which can occur and count towards the knockout cross section. The inelastic or stripping component describes the reaction, when the removed nucleon interacts inelastically with the target and the target is excited. Eq. (1.8) gives an intuitively interpretation of this process. The term $(1 - |S_n|^2)$ is the probability, that a nucleon is removed, while $|S_c|^2$ is the probability that the core is preserved. The elastic or diffractive component describes the process, where the projectile breaks up into a core and a nucleon from the interaction with the target. The nucleon and the core are elastically scattered and the target remains in its ground state. There is no intuitive interpretation of Eq. (1.9) for this process as for the inelastic equation. The calculation of the S matrices is an elaborated process, which has to be done consistently, so that the calculated R_s can be compared systematically. For details on the calculation of the S matrices it is referred to Ref. [35] and references within.

From the calculated single-particle cross sections the theoretical cross section σ_{th} is calculated with Eq. (1.6) and so the reduction factor can be determined. From various experiments in the past it has been found, that the reduction factors depend strongly on the excess of neutrons and protons in nuclei. Fig. 1.8 shows experimental results from neutron and proton removal reactions in the last decades. For comparison, results from (e,e'p) reactions with stable nuclei are also given in the figure. The x-axis in the plot is the difference ΔS between the proton separation energy S_p and the neutron separation energy S_n. The σ_{exp} in the figure is the inclusive cross section to all bound states in the final nucleus. Therefore, the σ_{th} includes the spectroscopic factors C^2S to all bound states, which are obtained from effective shell model calculations.

The figure shows a clear linear anti-correlation between ΔS and R_s. While the removal of very loosely bound nucleons exhibit a R_s close to 1, the removal of deeply bound nucleons are reduced to as much as 0.2. The reason for the slope is still under debate [35]. A possible explanation is, that the deeply bound nucleon is stronger confined to the center of the nucleus, where the nucleon probability density of the nucleus is higher. The interaction and the correlation with other nucleons is then stronger. For the loosely bound nucleons it is assumed, that they have higher probabilities to be on the outside of the nucleus, where the density of nucleons is much smaller. Thus, the interaction and correlations with other nucleons is smaller. The reduction factor R_s is calculated with the shell model, which has been adjusted to describe the properties of valence nucleons. This would explain the values of R_s close to 1 for the removal of loosely-bound nucleons and the large discrepancy with the removal of deeply-bound nucleons.

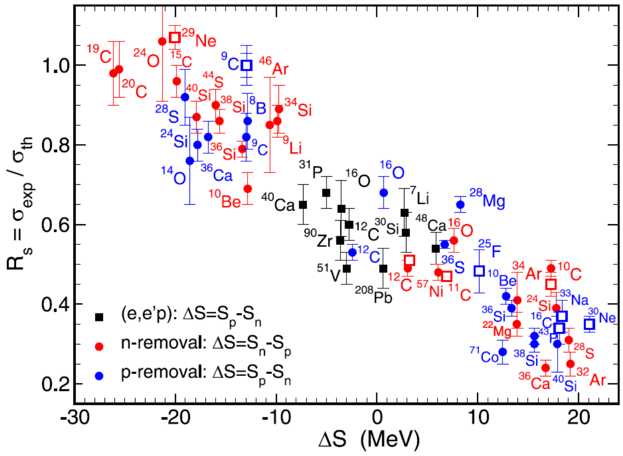

Figure 1.8.: R_s factor as a function of ΔS.The black squares are from electron-proton knockout, the red dots from neutron removal and the blue dots from proton removal. Figure from Ref. [36].

1.4.2. Transfer Reactions

In a transfer reaction a nucleon is either transferred from a nucleus (stripping) or to a nucleus (pick up). It has been used in the past to study single-particle states. In addition, two nucleon transfer can be used to study the two nucleon correlation effects inside a nucleus. The selection of experimental conditions play a major role in transfer reactions. The incident beam energy, the angles measured and the choice of nucleon removal or pick up reaction can have a significant role on the extracted cross sections and the reduction factors. The origin of this sensitivity is that the momentum of the beam needs to be matched to the momentum of the valence nucleon (removed nucleon) [37]. Ideal beam energies for transfer reactions are a few MeV/nucleon above the Coulomb barrier [35]. If the beam energy is below the Coulomb barrier, the cross section drops and becomes insensitive to the angular momentum l. For much higher beam energies, a poor momentum matching for the transferred nucleon can hinder the reaction or the process is not a single step anymore, which can be difficult for theory to describe. The impact of the choice of reaction is illustrated in Fig. 1.9. Here, the results from the nucleon removal reactions (p,d) and (^{3}He,α) from ^{76}Se are given [38]. The energy was 23 MeV/nucleon and 26 MeV/nucleon, respectively. The results show, that the (p,d) reaction prefers the $l = 1$ transfer, while the (^{3}He,α) reaction prefers the $l = 3$ and $l = 4$ transitions. This example points out the significance of momentum matching on transfer reactions. One has to carefully choose the reaction depending on the states one wants to populate. For the scattering angle, the cross section is optimized for forward scattering angles in the center of mass (c.m.) frame [35]. It is experimentally challenging, since the detector systems can struggle with the high luminosities and become rate limited for small angles. As indicated in the previous section, one key limitation of transfer reactions is the low incident energy. It allows only the use of thin targets, so that the recoil charged particles do not suffer too much from energy loss and angular straggling for the missing mass spectroscopy. Furthermore, to cover the full angular distributions a large statistic is necessary. For all this, a beam intensity of minimum 10^4 pps is usually necessary. Thus, transfer reactions can only access less exotic nuclei in comparison to knockout reactions.

In the past systematic transfer reaction studies have been performed despite the experimental difficulties. Here, some of the results will be presented and they will be compared with the results from knockout reactions.

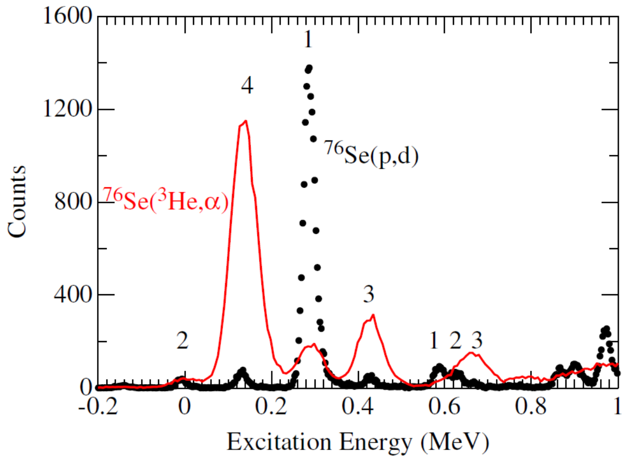

Figure 1.9.: Energy spectrum of the neutron-removal reactions from ^{76}Se. The numbers above the peaks indicate the l values of the transitions. The $l = 1$ transition is strong for the (p,d) reaction, while the $l = 3$ and $l = 4$ transitions are strong for (^{3}He,α). Figure from Ref. [38].

Fig. 1.10 (a) show the results of the (p,d) transfer reaction at 33 MeV/nucleon with the Argon isotopes ^{34}Ar, ^{36}Ar and ^{46}Ar [39, 40]. The R_s value is calculated for different optical potentials. The results for the optical potentials show large discrepancies, however they do not show a dependence on ΔS, despite covering a range of from -10 MeV to 15 MeV. This stands in contrast to the results from knockout reactions of argon isotopes [41–43], which are also given in Fig. 1.10 (a). Similar results can be seen in Fig. 1.10 (b) for the oxygen isotopes ^{14}O, ^{16}O and ^{18}O. The data is from $(d,{}^3\text{H})$ and $(d,\ {}^3\text{He})$ transfer reactions at 18 MeV/nucleon. The data is compared to theoretical calculations based on a Woods-Saxon potential and the shell model (WS + SM) and the self-consistent Green's function (SCGF). While both approaches show again differences in the R_s value, there is again no dependency on ΔS in the range from -20 MeV to 20 MeV.

The results from transfer reactions show, that the theoretical input for transfer calculation has a large impact and large uncertainties. Despite the uncertainties there are still systematic differences compared to knockout reactions. This is why in the next section a third reaction mechanism is considered for comparison.

1.4.3. QFS Nucleon Removal Reactions

Due to the large difference between the results from knockout from light-ion targets and from transfer reactions, a series of (p,pn) and $(p,2p)$ experiments have been carried out recently [45–48]. For these reactions, the nucleon-nucleon interaction is better understood, than for the light-ion targets, which makes the theoretical calculations more reliable. In addition, the experiments have been performed at beam energies from 200 MeV/nucleon to 450 MeV/nucleon. At these energies the QFS condition is likelier to be fulfilled and the mean free path is larger.

Fig. 1.11 shows the reduction factor results from different oxygen isotopes [48]. The nucleon-removal reactions from ^{14,22,24}O were performed with a beam energy of 250 MeV/nucleon in inverse kinematics and from ^{16,18}O with a beam energy of 200 MeV/nucleon in normal kinematics. A hydrogen target out of naphthalene was used for the inverse kinematics reaction. For the calculation of the single-particle cross section two different optical potentials were used: a potential from phenomeno-

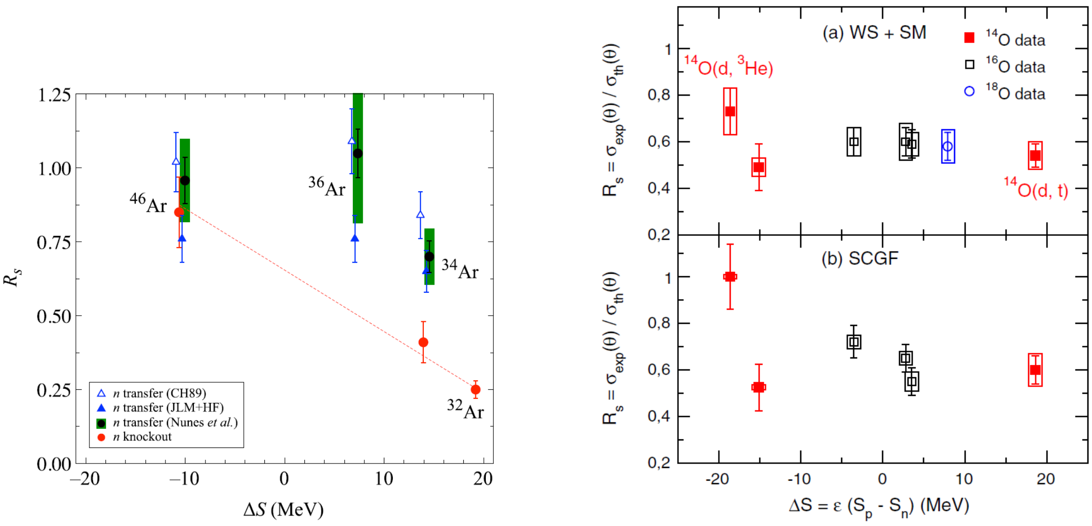

(a)

(b)

Figure 1.10.: (a) Results of (p,d) transfer reactions at 33 MeV/nucleon from Argon isotopes [39, 40] compared to intermediate energy knockout reactions from Argon [41–43]. Figure from Ref. [35]. (b) Results of $(d,^3\mathrm{H})$ and $(d,\,^3\mathrm{He})$ transfer reactions at 18 MeV/nucleon from oxygen isotopes. The top panel shows the WS + SM approach for the theoretical calculations, while the bottom panel uses the SCGF. Figure from Ref. [44].

logical Dirac parametrization and from the folding of nuclear densities with the Melbourne G-matrix interaction. Details on the potentials are given in Ref. [48] and references within. The use of both potentials results in similar reduction factors R_s, which show no dependence on ΔS as found in the results from transfer reactions. For comparison the R_s from $^{16}\mathrm{O}(e,e'p)$ [49] and $^{\mathrm{nat}}\mathrm{C}(^{14}\mathrm{O},^{13}\mathrm{N})$ [50] reactions are given in the plot, which confirm the reliability of the presented results.

The different results from the three reaction mechanisms have not been understood yet. It is assumed, that the reduction of the single-particle occupancies is induced from nucleon-nucleon correlations. The correlations should only depend on the observed nucleus and not on the reaction mechanism used to examine the nucleus. This indicates that some of the assumptions used in the theoretical descriptions of the nucleus are not justified. For knockout reactions it can be doubted, that the sudden and eikonal approximations are valid for the removal of deeply-bound nucleons, which are very unlikely to be removed without changing the core. Experimental results on the parallel momentum distribution, presented in the next section (Section 1.4.4), strengthen these doubts. For transfer reactions there are large uncertainties on the R_s value from the input of the theoretical calculations. These uncertainties can be seen in the large variation of R_s depending on the used potential (see Fig. 1.10). However, in the nuclear physics community it is agreed on that they can not explain the large systematic differences between transfer and knockout reactions.

1.4.4. Asymmetric Momentum Distribution

As described in Section 1.2 there have been fantastic results from the parallel momentum distribution from loosely-bound nucleons due to the sensitivity on the angular momentum (see Fig. 1.4). The theoretical calculations for those results are based on the sudden and eikonal approximation and predict a symmetric momentum distribution. However, in results from NSCL an asymmetric mo-

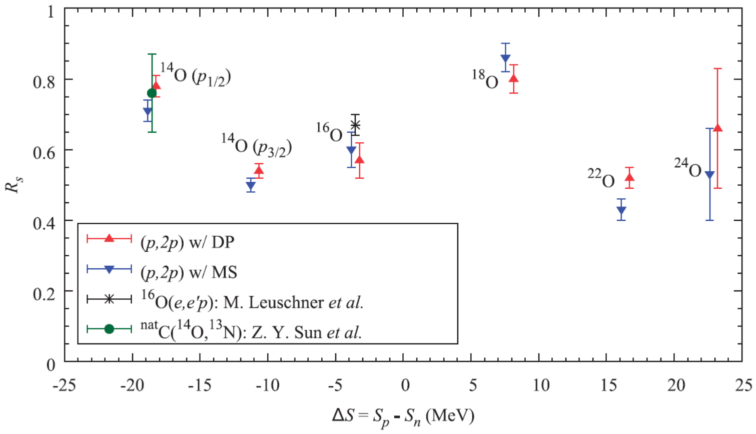

Figure 1.11.: QFS nucleon-removal results for several oxygen isotopes. The red and blue triangles were calculated with different optical potentials. For comparison the data from ^{16}O(e,$e'p$) [49] and $^{\mathrm{nat}}$C(^{14}O,^{13}N) [50] are given. Figure from Ref. [48].

mentum distribution from the removal of deeply-bound nucleons has been found [51]. The nucleon removal reactions ^{16}C(p,pN) at 75 MeV/nucleon and ^{14}O(p,pN) at 53 MeV/nucleon with a ^{9}Be target were performed. The separation energies for ^{16}C are $S_n = 4.25$ MeV and $S_p = 22.6$ MeV and for ^{14}O they are $S_n = 23.2$ MeV and $S_p = 4.63$ MeV. Both nuclei have a large ΔS of $\sim$20 MeV and so the removed nucleons are either very loosely-bound or deeply-bound. The resulting momentum distributions from the reactions are given in Fig. 1.12. Fig. 1.12 (a) and (c) show the loosely-bound nucleon removal distributions. The proton removal from ^{14}O exhibits a symmetric momentum distribution, which is described perfectly from theoretical calculations with the SE approximation. For the removal of the neutron from ^{16}C there is a slight asymmetry on the low momentum side, which the SE approximation cannot reproduce. The rest of the distribution is symmetric and reproduced well from the theoretical calculations. Fig. 1.12 (b) and (d) show the momentum distributions of the deeply-bound nucleon removal reactions. In both cases the distributions are strongly asymmetric and the SE approximation calculations fail to reproduce the experimental data. Both distributions show similar properties with the difference, that they are more pronounced in the neutron-removal from ^{14}O. They have a steep fall off on the high momentum side and a tail on the low momentum side. Theoretical transfer to the continuum (TC) calculations were applied on the neutron removal reactions. The calculation was able to predict the high momentum fall off, which has been attributed to energy conservation. However it was not able to reproduce the low momentum tail correctly.

The results for ^{14}O were measured with a beam energy of 53 MeV/nucleon. It is questionable if at this energy the SE approximation is fulfilled sufficiently. As mentioned above it is believed, that the ideal energy for the SE approximation is at some hundreds of MeV/nucleon. However, it could be an explanation for the difference of the reduction factors R_s from transfer and knockout reactions, if the applied theory for the knockout reactions is not correct. The results question the applicability of the SE approximation for deeply-bound nucleon removal reactions. In addition, the TC calculations have not been able to reproduce the low momentum tail, which indicates, that the reaction mechanism is not yet fully understood. Therefore, it is extremely important to understand and be able to reproduce the asymmetric momentum distribution from deeply-bound nucleon removal reactions. In 2015, there have been theoretical calculations on ^{14}O nucleon-removal reactions at 100 MeV/nucleon and 200 MeV/nucleon using the distorted-wave impulse approximation (DWIA) with the eikonal approximation [52]. Those calculations exhibit an asymmetric momentum distribution, which is shown

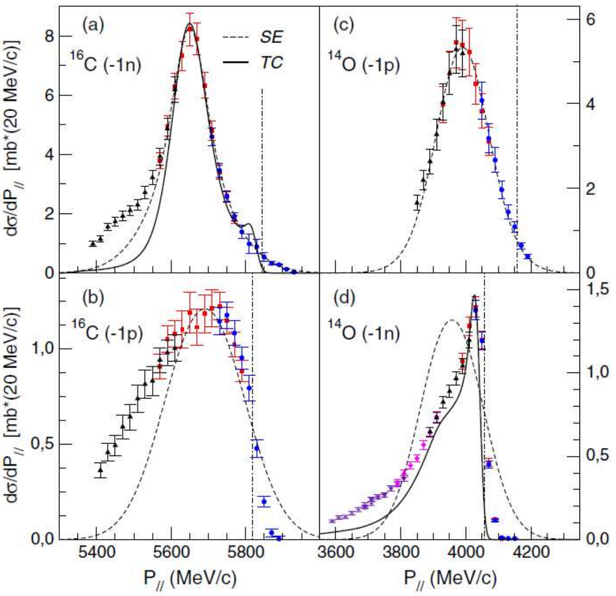

Figure 1.12.: (a) and (b) parallel momentum distribution (PMD) of nucleon removal from ^{16}C at 75 MeV/nucleon.(c) and (d) PMD of nucleon removal from ^{14}O at 53 MeV/nucleon. Figure from Ref. [51].

in Fig. 1.13 for 100 MeV/nucleon. Both distributions show similar features as the experimental distributions in Fig. 1.12. There is a low-momentum tail in both cases. However, the asymmetry in the case of the deeply-bound nucleon removal is far more pronounced. The low momentum tail is attributed to be from the final state interaction (FSI) from the attractive potential between the residue and the removed potential.

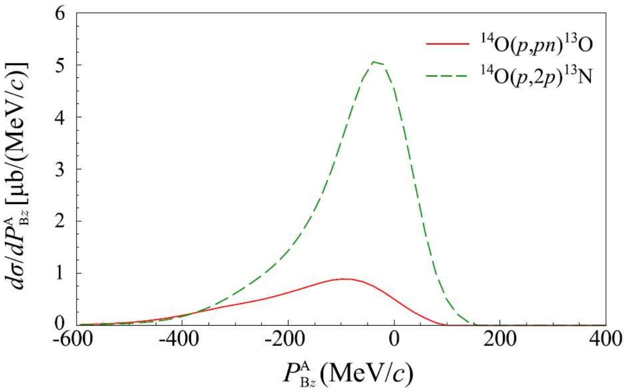

Figure 1.13.: PMD of ^{13}O (solid line) and ^{13}N (dashed line) after removal from ^{14}O at 100 MeV/nucleon. Figure from Ref. [52].

Up to now, there is no experimental data for nucleon-removal from ^{14}O at 100 MeV/nucleon or 200 MeV/nucleon for direct comparison. If it is possible to confirm these theoretical calculations with experimental data, it would be a significant step towards the understanding of the reaction mechanism. Despite the direct comparison to the theoretical calculations, there are several other reasons for the use of ^{14}O. First, ^{14}O is an ideal benchmark nucleus, since many experiments with different targets and energies have already been performed. Second, it has a doubly closed shell. The $1p_{1/2}$ shell for the protons and the $1p_{3/2}$ for the neutrons are fully occupied. Third, it has a large ΔS, which makes it a great probe to demonstrate the difference between loosely-bound and deeply-bound nucleon removal. The ΔS for proton removal is 4.63 MeV and for neutron removal 23.2 MeV. Finally, ^{13}O and ^{13}N have both no excited states, so that no gamma spectroscopy is necessary.

Therefore, a nucleon-removal experiment from ^{14}O with an incident energy of $\sim$100 MeV/nucleon with a thin hydrogen target has been performed at RIBF in 2018. In contrast to several previous experiments, where commonly a ^{9}Be or ^{12}C target was used, a structureless solid hydrogen target has been used during the experiment. This should have made the removal process cleaner, e.g. less disturbance from the target on the residue. The analysis of the data and the interpretation of the results are topic of this PhD thesis. The experimental cross sections and parallel momentum distributions for neutron and proton removal will be shown and compared to theoretical calculations. For the comparison inelastic scattering, the DWIA and the quantum transfer to continuum (QTC) theoretical frameworks are applied. They are briefly introduced in Section 4.1, where their main features are outlined.

Experiment

2. Experimental Setup

In this section the experimental setup and data analysis are presented. Since the nucleus ^{14}O is an unstable nuclei with a half-life of (70.621 ± 0.011) s [53], the experiment was performed in inverse kinematics at the Radioactive Ion Beam Facility (RIBF) in Japan. A graphical overview of the facility is shown in Fig. 2.1. The process to produce relativistic ion beams and the measurement of the ion beam and its reaction residues at the facility is explained. This includes explicitly the production and acceleration process of the beam at RIBF and the two spectrometers BigRIPS and SAMURAI.

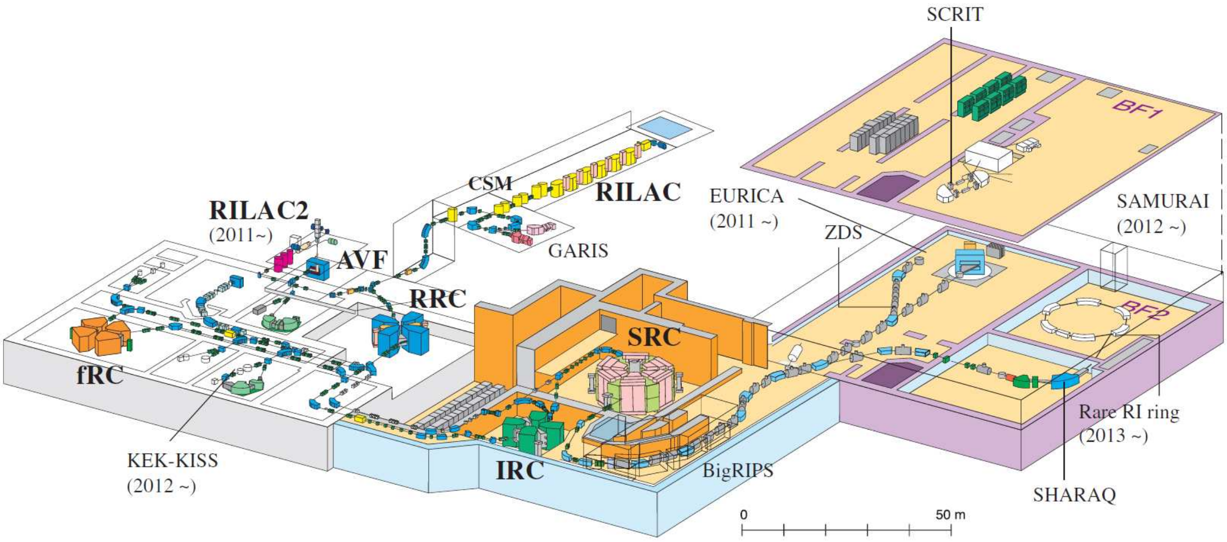

Figure 2.1.: Overview of the RIBF facility. Figure from Ref. [54].

2.1. Production of the ^{18}O Primary Beam

For the production of the ions different electron cyclotron resonance ion sources (ECRIS) are available at RIBF, which are used depending on the experiment. The primary accelerators for the produced ions are the two RIKEN ion linear accelerators (RILAC and RILAC2) and the azimuthally varying field (AVF) ring cyclotron. The secondary acceleration is then done by several cyclotrons: RIKEN Ring Cyclotron (RRC, K-value: 540 MeV), fixed-frequency Ring Cyclotron (fRC, K-value: 570 MeV), intermediate-stage Ring Cyclotron (IRC, K-value: 980 MeV), Superconducting Ring Cyclotron (SRC, K-value: 2600 MeV). The K-value of an accelerator characterizes the maximum beam energy of an accelerator due to its bending power. The definition is in Eq. 2.1, where E_{kin} is the kinetic energy, A is the mass number, Z is the atomic number and $B\rho$ is the magnetic rigidity of the accelerated particles. A summary and detailed description of the devices can be found in [54] and references within.

$$\frac{E_{\text{kin}}}{A} = \frac{(eB\rho)^2}{(\gamma+1)m_u} \cdot \left(\frac{A}{Z}\right)^2 = K \cdot \left(\frac{A}{Z}\right)^2 \tag{2.1}$$

The presented ion sources and accelerators can be combined in different ways depending on the task. Fig. 2.2 shows a schematic overview of the different acceleration modes. Currently, there are three commonly used schemes:

- The *Fixed-Energy Mode* is used to create beams of 345 MeV/nucleon (orange path).
- The *Variable Energy Mode* is for beams with different energies (yellow path).
- *AVF Injection Mode*, which is used for polarized deuteron beams at 880 MeV and low mass nuclei (blue path).

The *AVF Injection Mode* was used to produce the ^{18}O beam with an energy of 230 MeV/nucleon for this experiment. For the production of the ^{18}O ions, the 18 GHz super conducting ECRIS (18 GHz SR-ECRIS) was used. The ions are then accelerated by the AVF injector to an energy of 6 MeV/nucleon. After this first stage, the beam is accelerated by the three cyclotron accelerators RRC, IRC and SRC [55]. During the acceleration process, the ^{18}O beam passes through two carbon stripping foils (ST1 and ST4) to remove remaining electrons. The first foil is placed after the AVF injector and the second one after the RRC. The final energy of the beam is 230 MeV/nucleon and from the SRC it is guided to the RIKEN Projectile Fragment Separator (BigRIPS).

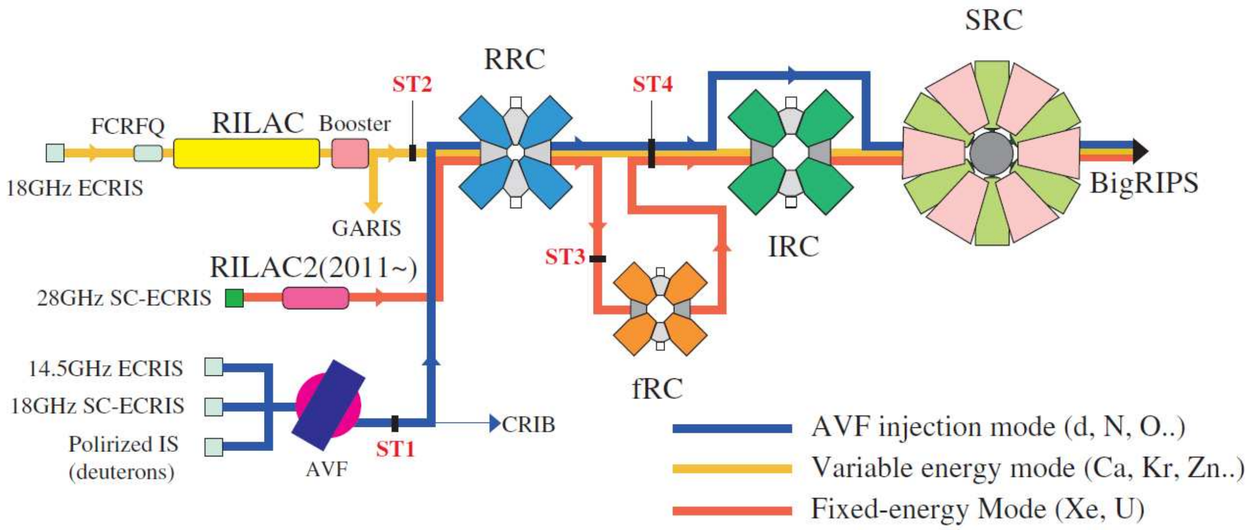

Figure 2.2.: Overview of the particle acceleration schemes at the RIBF. Figure from Ref. [54].

2.2. BigRIPS

The primary ^{18}O beam at 230 MeV/nucleon was impinged on a 14 mm thick beryllium target. The resulting fragments traversed through the BigRIPS spectrometer, which is designed as a two stage spectrometer consisting of a separator and an analyzer part. The setup of BigRIPS is shown in Fig. 2.3.

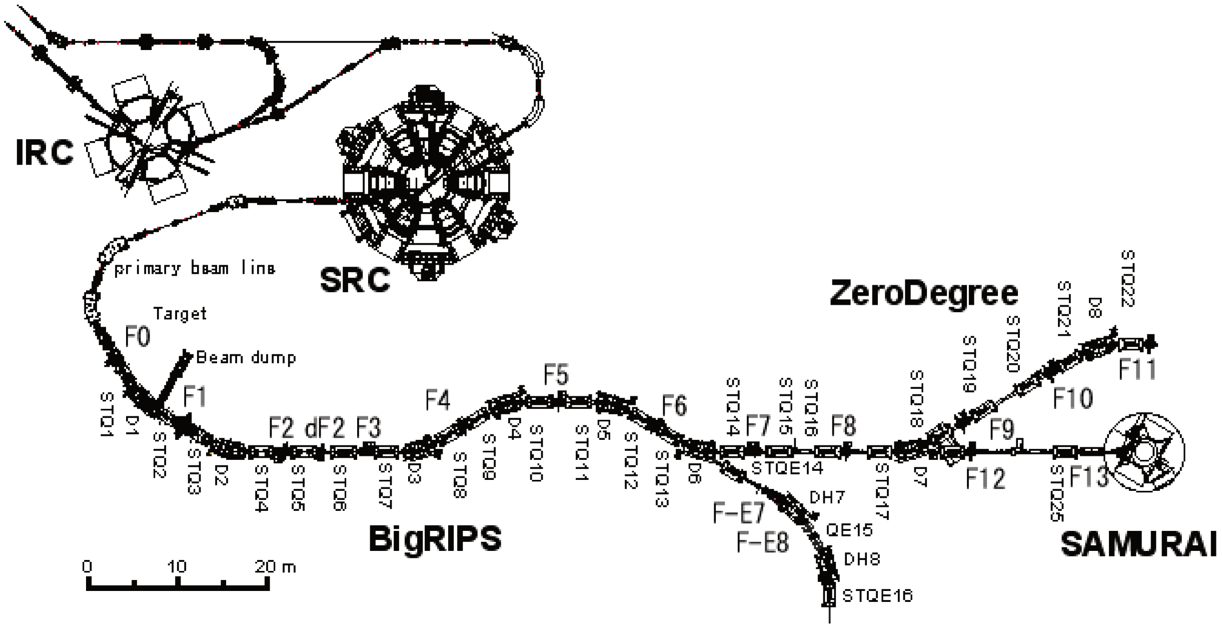

Figure 2.3.: BigRIPS separator and analyzer. Figure from Ref. [56].

The first stage is an achromatic spectrometer, which separates the different produced fragments. Achromatic in ion optics means, that the position in the focal plane is independent of the momentum of the beam particles. It includes four superconducting quadrupole magnet tripleds (SQT1 - SQT4), two dipole magnets (D1 and D2) and a wedge at the focal point F1. The separation process can be described in three steps, which is referred to as $B\rho - \Delta E - B\rho$ selection. A detailed explanation of the procedure is given in [57, 58]. The trajectory of an ion in a dipole magnet can be derived from the Lorentz and the centrifugal force:

$$\begin{aligned} q \cdot \gamma \cdot \vec{v} \times \vec{B} &= m\frac{(\gamma v)^2}{\rho} \\ \Leftrightarrow \frac{A}{q} &= \frac{B\rho c}{m_u \gamma \beta} \quad . \end{aligned} \tag{2.2}$$

Here, A is the mass number, q is the charge of the particle, $B\rho$ is the magnetic rigidity, c is the speed of light, m_u is the atomic mass unit, γ is the Lorentz factor and $\beta = v/c$ with v the velocity of the particle. For a fully stripped ion the charge q can be replaced by the atomic number Z

$$\frac{A}{Z} = \frac{B\rho c}{m_u \gamma \beta} \quad . \tag{2.3}$$

The magnetic rigidity $B\rho$ depends on the ratio of A/Z and on v. Thus, the dipole magnet can be used as a particle filter to select particles with the desired A/Z ratio and velocity. The selected particles are then focused on the point F1, where a wedge-shaped achromatic degrader and a slit are placed. The slit at F1 has a horizontal width of 4 mm and rejects particles, resulting in an acceptance of dp/p = 0.19 %. The aluminum degrader has a thickness of 9 mm and reduces the energy of the particles, depending on the position offset of the particles. The energy loss in the degrader leads to a new ratio of $A^{2\gamma-1}/Z^{2\gamma-2}$ with γ being a material constant of the wedge. Due to the new ratio, other particles can be selected with the dipole magnet D2. The focal point F2 is an achromatic focus, where a second slit is placed for adjustment of the beam.

The second stage of BigRIPS starts at the focal point F3. It uses the $B\rho - \Delta E-$TOF method for the identification of the ions, where TOF is the time of flight between two plastic scintillators. The triplet quadrupole magnets STQ7 - STQ14 and dipole magnets D3 - D6 are used at this stage. In our setup the slits at F5 and F7 had a width of 5 and 7 mm, respectively. For the particle identification of the beam 3 mm thick plastic scintillators are used at F3 and F5, which are read out with two photomultipliers on each side. The working principle of the detectors is described in Section 2.5.1. The plastic scintillators measure the energy loss ΔE of the particles. The TOF can be calibrated with the time signal of two plastic scintillators and the $B\rho$ of the beam at D3/D4 or D5/D6. A $\Delta E-$ TOF plot can then be created to identify the particles. A complete overview of BigRIPS setup used during the experiment is given in Table 2.1.

Table 2.1.: Overview of the BigRIPS configuration during the experiment.

Component	
Primary Beam	^{18}O
Intensity [pnA]	400
Production Target ^{9}Be [mm]	14
F1 Aluminium Degrader [mm]	9
D1 [Tm]	3.41
D2 [Tm]	2.8581
D3 [Tm]	2.7332
D4 [Tm]	2.7332
D5 [Tm]	2.5978
D6 [Tm]	2.5978
F1 Slit [mm]	4
F2 Slit [mm]	6
F5 Slit [mm]	10
F7 Slit [mm]	60
F3 Plastic Scintillator [mm]	3
F5 Plastic Scintillator [mm]	3

2.3. SAMURAI spectrometer

The SAMURAI spectrometer consists of several detectors around a superconducting dipole magnet [59]. The dipole magnet is placed on a rotatable platform, which makes it flexible for various experimental setups. It has an inner gap size of 0.8 m and a maximum magnetic field integral of 7.1 Tm, which allows a complete kinematic measurement for various reaction residues. A resolution of up to 1/1500 can be achieved for the magnetic rigidity.

The setup with the used detectors and the measured beam and residues is shown in Fig. 2.4. When the secondary beam enters the SAMURAI spectrometer area it is first tagged by the plastic scintillator SBT1 to measure its energy deposition and arrival time. For the measurement of the beam position on the target two drift chambers BDC1 and BDC2 are used in front of the target. The secondary beam is then impinged on the target. The fragments from the reaction go through the SAMURAI dipole magnet, which separates them according to their $B\rho$. In front of and after the SAMURAI magnet are two drift chambers FDC0 and FDC2, which measure the position coordinates of the fragments for reconstructing $B\rho$ and the flight length L. At the end of the setup the energy loss ΔE is measured by a plastic scintillator array hodoscope. In addition, a time signal is measured with the hodoscope, which is then used in combination with SBT1 in front of the target to reconstruct the TOF. The detector positions were determined with a photogrammetry measurement (PGM). A sketch with all distances can be seen in Fig. 2.5.

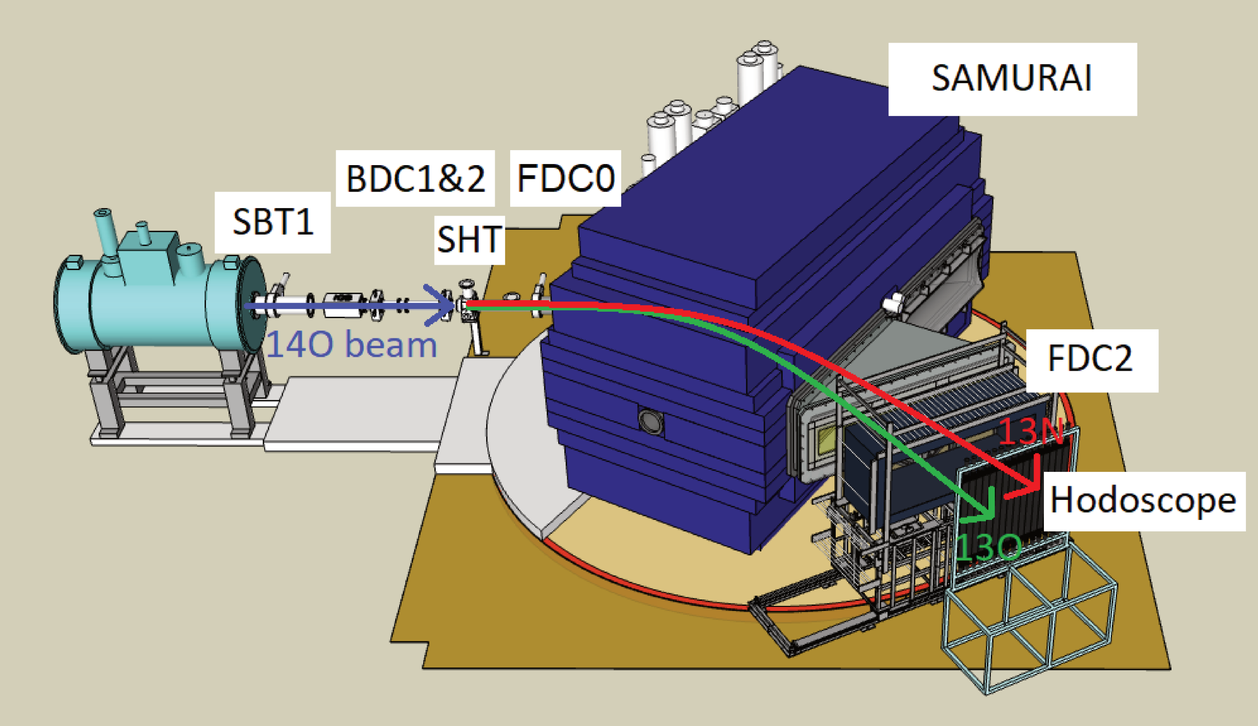

Figure 2.4.: Graphical view of the SAMURAI experimental area. The position of the used detectors is indicated by the labels.

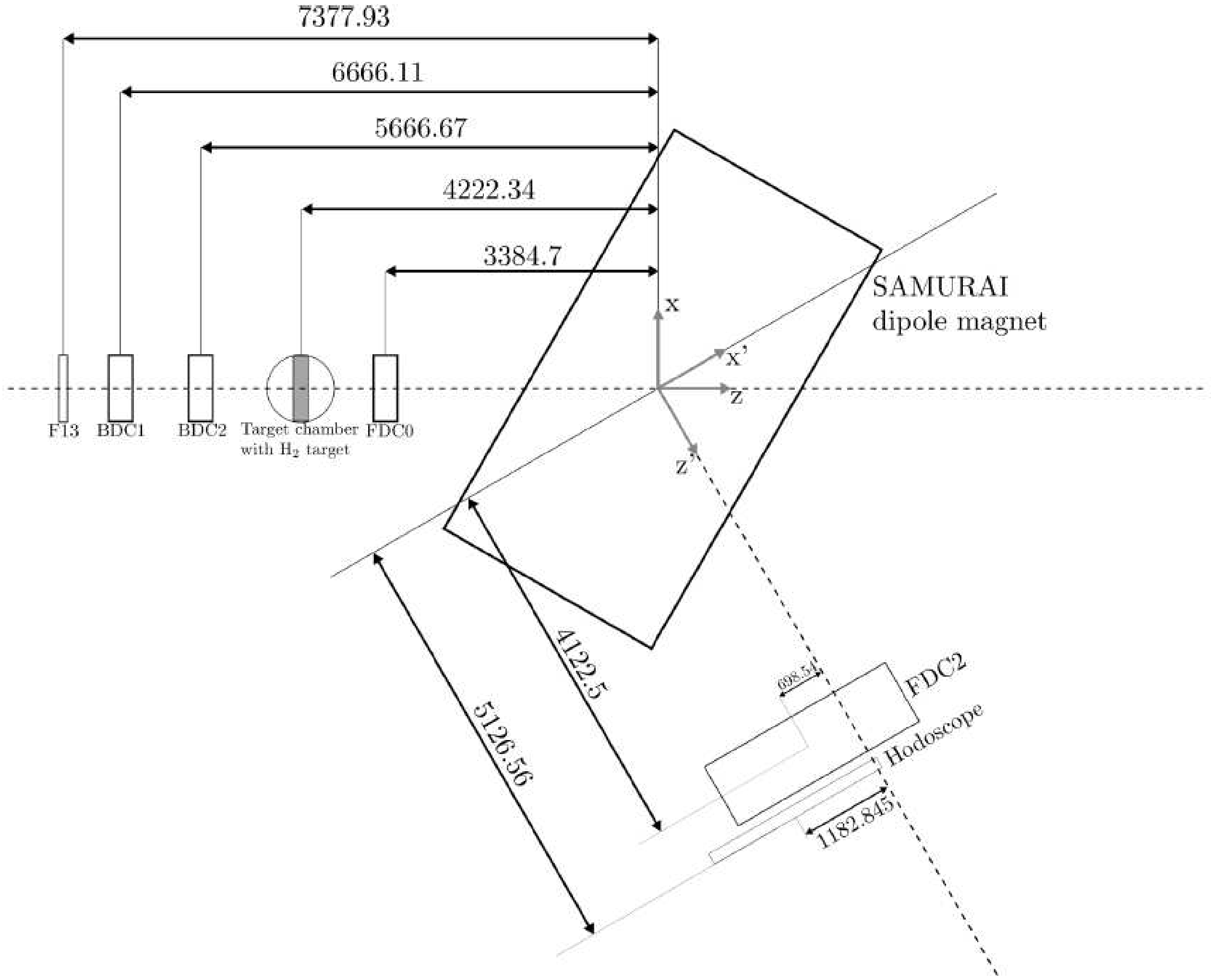

Figure 2.5.: Sketch of the SAMURAI experimental area for this experiment. The detector positions were determined with a photogrammetry measurement and are given in mm.

2.4. Overview of the Beam Line Materials

An overview of the beam line material is given here. Therefore, two tables are presented. In Table 2.2 and Table 2.3 up- and downstream materials are listed, respectively. The water on the target entrance and exit windows is condensation water, which was observed during the experiment. A picture of the condensated water was taken during the experiment and can be seen on Fig. 2.6. The value in the tables for the thickness of the water is an estimation of the average water thickness. However, the water distribution is in fact non-homogeneous as can be seen on the picture and thus the energy and momentum loss of the particles is also not homogeneous. This is why the energy loss of the water needs to be treated explicitly, which will be covered in Section 3.12. The target thickness calculation is described in Sec. 3.9. The separation of the beam line materials has the practical purpose, that the energy loss of the beam is usually calculated to mid target and that the energy loss of the reaction residues start from mid target. The energy loss calculation is relevant in the data calibration and analysis section. If a component is not mentioned in the table, it was removed from the beam line (e.g. SBT2) or in vacuum (e.g. the dipole magnet) during the experiment and thus had no impact on the energy loss.

From the last column of the tables one difficulty for the analysis of this experiment becomes obvious. If the material budget of the beamline is added up, the overall thickness is in the order of the target thickness. This means, that a large background can be expected and in fact, has been found during the analysis process. A proper particle identification was one of the key challenges for the analysis of this experiment.

Table 2.2.: Material between the dipole magnets D5/D6 and the SHT.

Part	Material	Thickness [μm]	Thickness [atoms/m^2]
F13 window	Mylar	4	$3.85 \cdot 10^{19}$
F13 plastic	Plastic	200	$2 \cdot 10^{21}$
F13 window	Mylar	4	$3.85 \cdot 10^{19}$
Gap	Air	$10 \cdot 10^3$	$4.94 \cdot 10^{19}$
Foil	Aluminium	24	$6.63 \cdot 10^{19}$
BDC1 window	Kapton	75	$6.65 \cdot 10^{20}$
BDC1 gas	$H_{10}C_4$	90	$2.22 \cdot 10^{20}$
BDC1 electrodes	Mylar	72	$6.93 \cdot 10^{20}$
BDC1 window	Kapton	75	$6.65 \cdot 10^{20}$
BDC2 window	Kapton	75	$6.65 \cdot 10^{20}$
BDC2 gas	$H_{10}C_4$	90	$2.22 \cdot 10^{20}$
BDC2 electrodes	Mylar	72	$6.93 \cdot 10^{20}$
BDC2 window	Kapton	75	$6.65 \cdot 10^{20}$
Exit	Kapton	125	$1.11 \cdot 10^{21}$
Gap	Air	$108 \cdot 10^3$	$5.34 \cdot 10^{20}$
Foil	Aluminium	24	$6.63 \cdot 10^{19}$
Gap	Air	$70 \cdot 10^3$	$3.46 \cdot 10^{20}$
Target window entrance	Water	393	$3.94 \cdot 10^{21}$
Target window entrance	Kapton	75	$6.65 \cdot 10^{20}$
Target cell	Aramid	6	$6.45 \cdot 10^{19}$
1/2 Target	Solid hydrogen	$1.2 \cdot 10^3$	$6.17 \cdot 10^{21}$

Table 2.3.: Material between the SHT and the SAMURAI dipole magnet.

Part	Material	Thickness [μm]	Thickness [atoms/m^2]
1/2 Target	Solid hydrogen	$1.2 \cdot 10^3$	$6.17 \cdot 10^{21}$
Target cell	Aramid	6	$6.45 \cdot 10^{19}$
Target chamber exit	Kapton	75	$6.65 \cdot 10^{20}$
Target chamber exit	Water	393	$3.94 \cdot 10^{21}$
Gap	Air	$130 \cdot 10^3$	$6.42 \cdot 10^{20}$
Silicon chamber entrance	Aluminium	10	$6.03 \cdot 10^{19}$
Silicon chamber	Air	$350 \cdot 10^3$	$1.72 \cdot 10^{21}$
Silicon chamber exit	Aluminium	10	$6.03 \cdot 10^{19}$
Gap	Air	$50 \cdot 10^3$	$2.45 \cdot 10^{20}$
Window	Kapton	125	$1.11 \cdot 10^{21}$
FDC0 window	Kapton	75	$6.65 \cdot 10^{20}$
FDC0 gas	$H_{10}C_4$	90	$2.08 \cdot 10^{20}$
FDC0 electrodes	Mylar	72	$6.93 \cdot 10^{20}$
FDC0 window	Kapton	75	$6.65 \cdot 10^{20}$
FDC1 window	Kapton	75	$6.65 \cdot 10^{20}$
FDC1 electrodes	Mylar	120	$1.16 \cdot 10^{21}$
FDC1 window	Kapton	75	$6.65 \cdot 10^{20}$

Figure 2.6.: Condensation water found during the experiment on the target entrance and exit windows. Courtesy Y. Sun.

2.5. Detector System and Target

In this section, the detectors and the target around the SAMURAI dipole magnet, which were used during the experiment, are presented. Their working principle and the observable quantities are discussed in detail.

2.5.1. Start Beam Trigger Plastic Scintillator

The Start Beam Trigger (SBT) plastic scintillator is at the beginning of the SAMURAI experimental area and measures the arrival time and the energy loss of the beam. It is a scintillation detector, which consists of two parts: the scintillating material and two photomultiplier tubes (PMT). Usually, the SBT at SAMURAI consists of two 1 mm thick plastic scintillators, SBT1 and SBT2. However, during this experiment only SBT1 was used to reduce the background. As scintillating material, the organic plastic BC408 is used with a quadratic shape of 120 mm x 120 mm. The molecules inside the plastic are excited, when charged particles pass through the material. They release their energy via photon emission, which is called fluorescence. The produced photons inside the plastic are collected by two light guides at the end of the plastic and transmitted to two PMTs. Here, the light signal is converted into an electrical signal by the photoelectric effect. The produced photoelectrons build up a current, which is amplified by multiple dynodes. The final current is processed into a signal by a Charge-to-Digital Converter (QDC). The pulse shape can then be described by a two-component exponential decay. Those decays are described by the two time constants τ_s (slow) and τ_f (fast) and are material dependent. A typical decay constant is around $\sim$2 ns. Approximately, the fluorescent light is proportional to the energy loss ΔE of the particle in the scintillator. For an exact treatment it is a function of the energy and the charge of the incoming particle [60]. The use of scintillating material in combination with a PMT is widely used technique and described in detail in the literature [61, 62].

2.5.2. Multi-Wire Drift Chambers

For the measurement of the position and the angles of the beam and residue particles Multi-Wire Drift Chambers (MWDC) are used. A MWDC consists basically of two components, which are confined in a closed chamber: a drift gas and a set of potential wires. Incoming radiation particles ionize the gas inside the chamber. The released electron-ion pairs will start to drift to the anode and cathode wires. The drift velocity depends on the gas and the potential between the anode and cathode. By triggering a start signal when the ionizing particle arrives and measuring the time the electrons need to arrive at the wires, the time of flight of the electrons through the detector can be calculated. The origin of the ionization can then be reconstructed with the average drift velocity. The typical position resolution is around 100 μm. Since the drift distance is limited by the potential on the wire, one wire can only cover a limited area of space to detect particle positions. For covering a greater area with a high precision multiple wires are aligned in equidistant positions. Further details on the MWDC can be found in Refs. [61, 62] and technical details of the drift chambers used at SAMURAI in Ref. [59].

Beam Drift Chamber (BDC) The two drift chambers BDC1 and BDC2 are placed 1444.33 mm in front of the secondary target. The distance between BDC1 and BDC1 is about $\sim$1 m. Each drift chamber has a total of eight wire layers. Four are oriented along the x-axis and four along the y-axis. They cover an active area of 80 $\times$ 80 mm. With the x- and y-coordinates the position of the beam on target can be calculated. The drift gas $\mathrm{C_4H_{10}}$ at 50 torr is used. The efficiency of the BDC is usually close to

100 %.

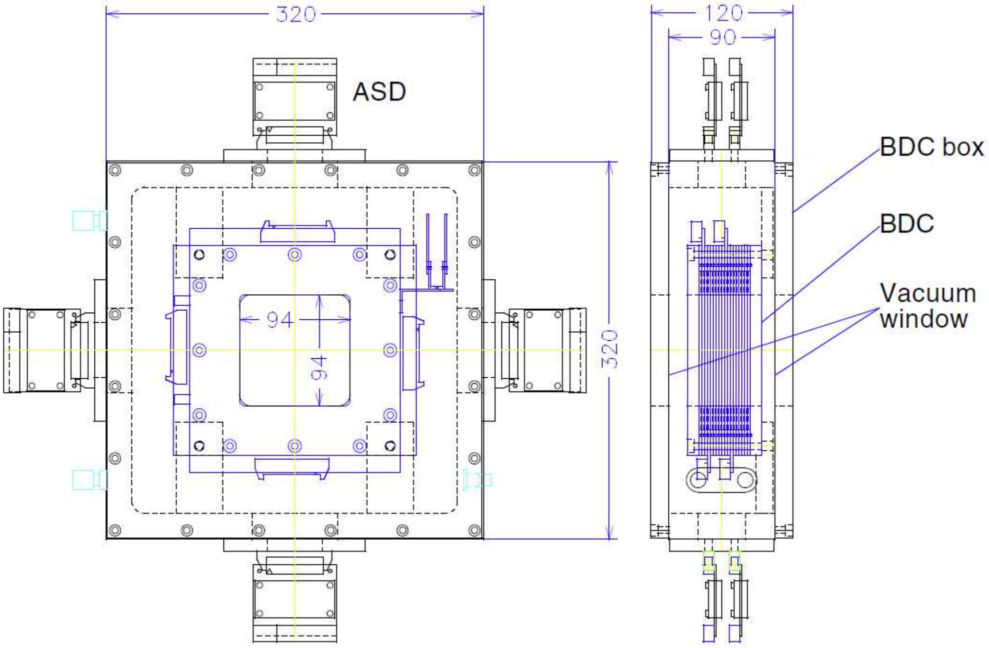

Figure 2.7.: Schematic drawing of a BDC. The lengths are given in mm. Figure from Ref. [59].

Foward Drift Chamber 0 (FDC0) The drift chamber FDC0 is placed 837.64 mm behind the target and in front of the SAMURAI dipole magnet. It is constructed and operates as the BDC drift chambers. The task of FDC0 is to measure the x- and the y-positions of the reaction residues and the unreacted beam. The trajectories of the particles in the dipole magnet can be reconstructed from the coordinates together with FDC2. The efficiencies for this experiment are calculated in the analysis part and given in Table 3.4.

Foward Drift Chamber 2 (FDC2) The drift chamber FDC2 is located behind the SAMURAI dipole magnet and measures the x- and y-positions of the bent unreacted beam and reaction residues. Together with FDC0 the trajectories of the particles can be reconstructed and so their flight length and magnetic rigidity. The active volume of the FDC2 drift chamber is $2.2 \times 0.8 \times 0.8$ m. The drift chamber needs to be 2.2 m wide in x-direction, because the particles are spread by the magnetic field in the x-direction to distinguish them. The large width makes it impossible to align the wires along the x-axis, since they would bend strongly and so the y-position cannot be measured directly. Therefore, for the measurement of the particle position six layer of wires are aligned along the y-axis to measure the x-position (X-layers), four layer of wires have an angle of 30° with respect to the y-axis (U-layers) and another four layer of wires have an angle of -30° with respect to the y-axis (V-layers) to reconstruct the y-position with the information from the x-position measurement. Two layers of wires build a group, which are separated from another group by a 100 mm gap with shield wires in between. The arrangement of wire groups follows the pattern XX'-UU'-VV'-XX'-UU'-VV'-XX'. A schematic view of the setup is shown in Fig. 2.8. The wires are arranged in a hexagonal cell structure, where one anode wire is surrounded by six cathode wires. In total they add up to 1568 anodes, 4788 field and 328 shield wires. As drift gas He + 50 % C_2H_6 at 1 atm is used. The efficiency is again given in Table 3.4.

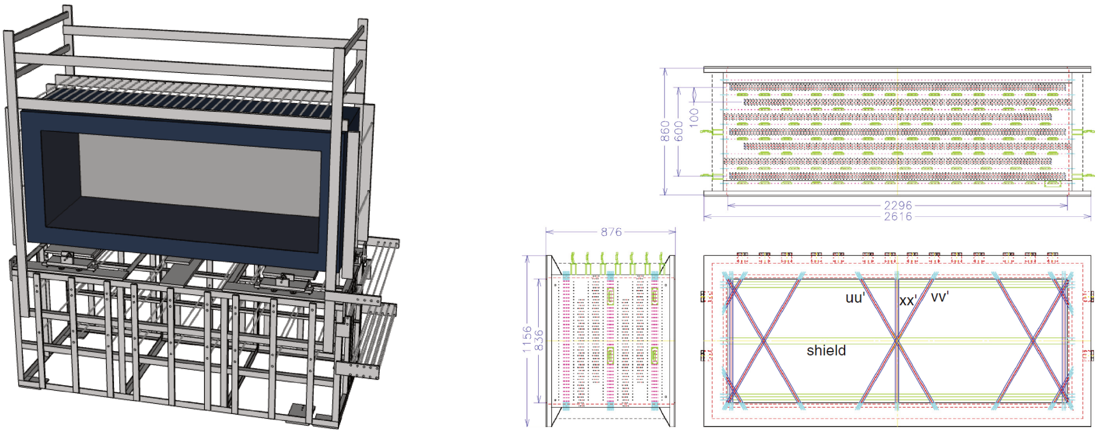

(a) (b)

Figure 2.8.: (a) Graphical view of the FDC2 detector (without wires). (b) Schematic sketch of the wiring inside FDC2. The lengths are given in mm. The top figure shows the view on the FDC2 box from above, the bottom left figure from the side and the bottom right figure from the front. Figure from Ref. [59].

2.5.3. Hodoscope

There are two different hodoscopes, one for protons (HODP) and one for fragments (HODF). A hodoscope is an array of vertical aligned plastic scintillators and both are placed behind FDC2 [59]. Only the HODF was used, since for the experiment no protons were measured. The objective is to measure the energy deposit ΔE and the arrival time of the fragments. For HODF 24 plastic scintillator bars with a size of $10(\mathrm{H}) \times 120(\mathrm{V}) \times 1(\mathrm{D})\,\mathrm{cm}^3$ are aligned next to each other, see Fig. 2.9. The photons are collected by PMT's at the top and bottom side of each scintillator bar. Each module has a separate voltage supply and cabling. Therefore, the gain and TOF offset must be calibrated individually. The TOF can be calculated with timing information from SBT1. The typical resolution for the atomic number is $\sigma_\mathrm{Z} \approx 0.16$ and the time $\sigma_\mathrm{T} \approx 140\,\mathrm{ps}$ [59].

2.6. The Solid Hydrogen Target

The target of the experiment was a 2.4 mm thick solid hydrogen target (SHT), which was used in the experiment before by the SAMURAI12 collaboration. In the experiment of the SAMURAI12 an exact vertex reconstruction was necessary, which was made possible by the use of a thin hydrogen target. For our experiment a liquid hydrogen target would have been sufficient, however for convenience and time schedule reasons the experiment was performed with the SHT. The production of a SHT is a very elaborated process and described in detail in Ref. [60]. It has to be cooled down to 14 K to become solid and the temperature distribution has to be homogeneous, so that the density of the target is uniform. For a better thermal distribution para-Hydrogen is used, which has a better thermal conductivity then normal-Hydrogen. Tests with normal-Hydrogen revealed, that evaporation holes were building immediately. Occasionally an evaporation hole can also occur with para-Hydrogen as seen in Fig. 2.10. However, during the analysis of the data, it did not have an impact on the extracted cross sections. The density was determined to be $0.86\,\mathrm{g/cm}^3$ by monitoring the temperature of the target cell and was stable during the whole experiment.

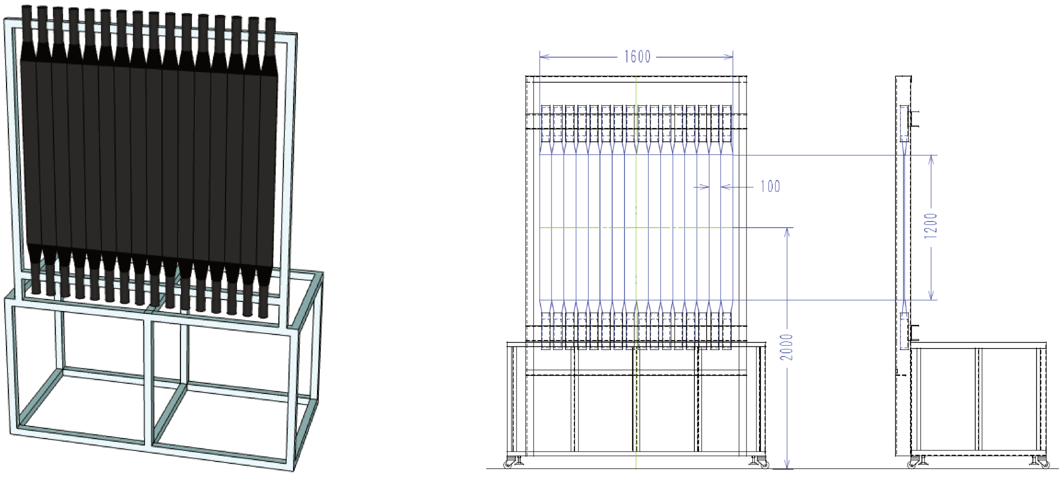

(a) (b)

Figure 2.9.: (a) Graphical view of HODF. (b) Schematic HODF plastic scintillator array. The lengths are given in mm. Figure from Ref. [59].

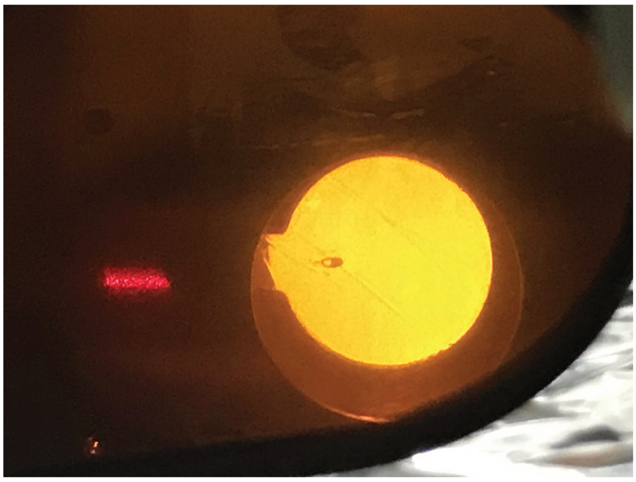

Figure 2.10.: Picture of the SHT during the experiment. Courtesy Y. Sun.

3. Data Calibration and Analysis

The purpose of the calibration is to convert the measured raw data of an experiment into physical quantities. The extracted information from the detectors are often given in arbitrary units, which is with digital electronics always a bin number within the range of the channel considered. The connection of this channel number to physics quantities is called calibration. Therefore, a conversion into reasonable units, e.g. MeV, mm, ns, is often the first step when extracting the raw data. This procedure is accompanied by checking correlations between detectors and if the data is reasonable. This important first step is described in this chapter. Afterwards, the data can be investigated closer and the physical interpretation can begin.

3.1. Trigger Selection and Dead Time

Two main trigger systems were used during the data taking of the experiment. First, the ^{14}O *beam trigger*, which task it is to count the ^{14}O particles impinging onto the target. It registers an event, when both F5 and SBT1 receive a signal. To avoid most of unnecessary other particles, two measures were performed. A veto was implemented for F5 for particles with $Z \leq 7$ to exclude low Z particles from being registered. Most of the other particles with $Z > 7$ are excluded by the dipole magnets at BigRIPS, which are configured for ^{14}O at $\sim 100\,$MeV/nucleon. With these most of the registered events were ^{14}O and the trigger was down scaled by a factor of 100 due to the high intensity of the beam. The second trigger is the *reaction trigger*. It has the same condition as the *beam trigger* plus that the hodoscope needs to register an event with $Z \leq 8$. Thus, the task is to register the successfully measured reaction residues from the SAMURAI spectrometer, when a beam particle was registered.

Table 3.1.: Summary of the trigger conditions for the two used triggers. The "x" indicates that the detector needs to receive a signal, so that the trigger system starts recording an event. For the plastic scintillator F5 a veto was applied for particles with Z $\leq$ 7.

	F5	SBT1	Hodoscope
Beam trigger	x	x	-
Reaction trigger	x	x	x

In addition, the DAQ lifetime for the *beam trigger* and *reaction trigger* needs to be considered for the calculation of the cross section. The DAQ lifetime is calculated by the number of measured events to the number of possible cycles. For the *beam trigger* an average ratio of ~0.54 and for the *reaction trigger* ~0.69 is extracted, respectively. Thus, the counts of the beam and fragments are corrected by the DAQ lifetime. A complete table for all runs is given in Appendix A. Here, one can see that the values change over time. This is because the beam intensity during the experiment was high with 9×10^3 particles per second. At higher beam intensities there are more fluctuations in the intensity and the DAQ is adjusting the lifetime values to this change.

3.2. Selection and Energy Calibration of ^{14}O at BigRIPS

3.2.1. Selection of ^{14}O

From the described hardware selection in the previous section, the selection of ^{14}O is performed straightforward by analyzing the energy deposit of F3 and F5. An absolute $\Delta E - B\rho -$TOF calibration was not necessary, since ^{14}O is identified unambiguously. This can be seen on Fig. 3.1, where the measured charge of F3 and F5 is shown. There is only few background left from other particles. A software selection is applied (black circle) to remove the remaining background around ^{14}O.

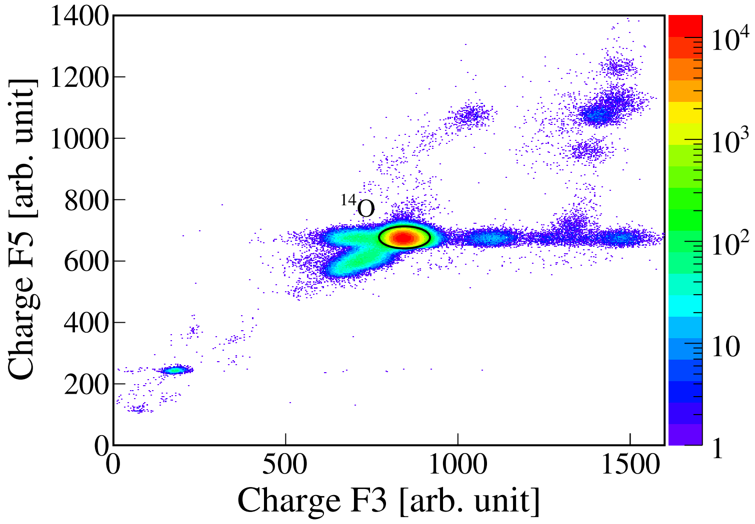

Figure 3.1.: F5 energy deposit of the beam against F3 energy deposit of the beam for the selection of ^{14}O. The black circle indicates the selection of ^{14}O.

3.2.2. Energy Calibration of ^{14}O

The two dipole magnets D5 and D6 have a magnetic rigidity of $B\rho = 2.5978\,\mathrm{Tm}$. From that, the velocity v and kinetic energy E_{kin} are calculated. ^{14}O has a kinetic energy of 100.8 MeV/nucleon at D5/D6 (Fig. 3.2 (a)) . With the velocity v at D5/D6 and the flight length of 59.03807 m between F5 and F13, the TOF is calibrated. Finally, the kinetic energy of ^{14}O at mid target is calculated. For the energy loss calculation the program *ATIMA 1.2 LS-theory* [63] implemented in *LISE++* [64] is used. The relevant materials for the energy loss from BigRIPS up to the target have been listed in Table 2.2. The energy loss calculation is separated into three steps. First, the energy loss of the beam from the dipole magnets D5/D6 to the entrance of the target chamber is calculated. A linear function is created from the energy loss simulations, which transforms the velocity at D5/D6 to the velocity at the target chamber entrance. The function for the energy loss up to the target entrance window can be seen in Fig. 3.2 (c). In the next step, the energy loss due to condensation water on the target chamber entrance window is calculated. Since, the water distribution is not homogeneous on the window, the particles experience different energy losses depending on the water thickness. Therefore, a value for the water thickness is generated for each particle and an energy loss applied according to the function in Fig. 3.2 (d). For example a particle with a momentum of ~ 6090 MeV/c will have a momentum of ~ 6040 MeV/c after going through $\sim 400\,\mu$m water. The generation of the water thickness for each particle is explained in detail in Section 3.12. The last step is the calculation of the energy loss from the target chamber entrance window to the mid of the SHT target. Here, the same procedure as for the first energy loss is applied. The last function is given in Fig. 3.2 (e). The final beam energy distribution is shown in Fig. 3.2 (b) with a mean value of ∼94 MeV/nucleon. The slightly asymmetric shape in comparison to the original distribution is due to the non-homogenous energy loss in the water.

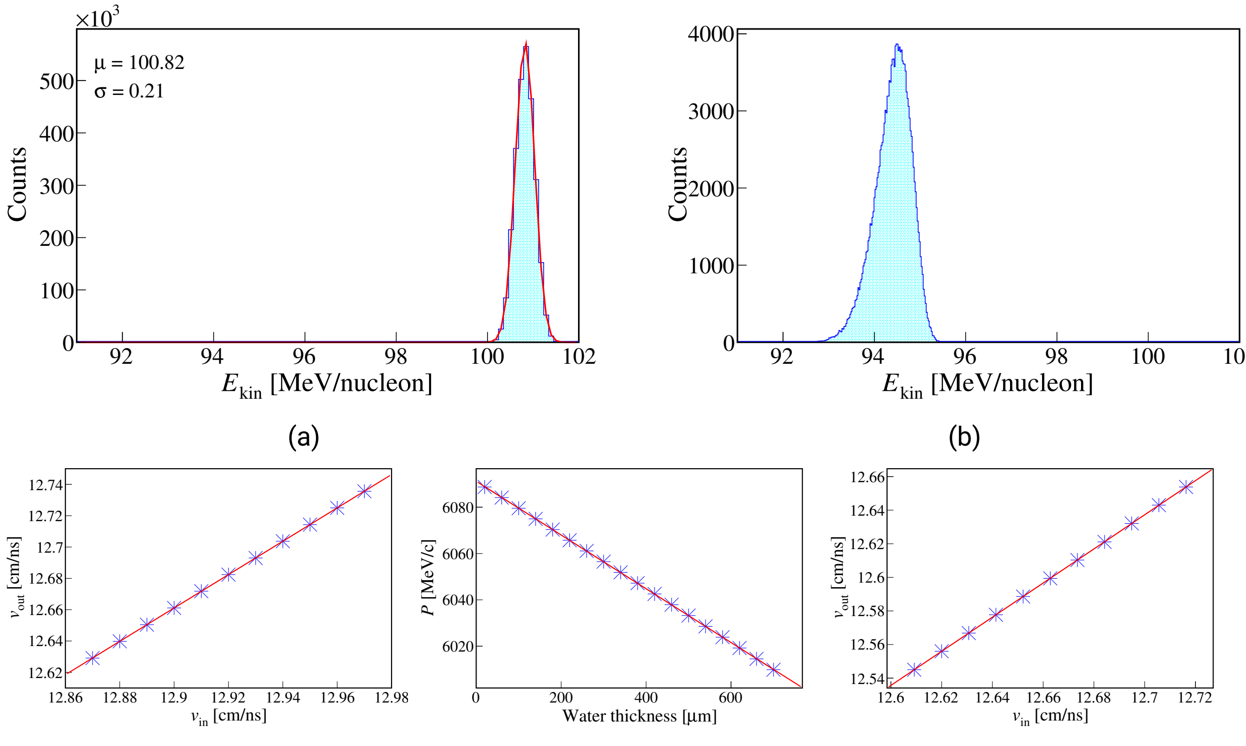

(a)

(b)

(c)

(d)

(e)

Figure 3.2.: (a) Energy of the beam at the dipole magnets D5/D6. (b) Energy of the beam at mid target. The energy of the beam at mid target was calculated in three steps. (c) Energy loss function from D5/D6 to the entrance window of the target chamber. (d) Energy loss function through water. (e) Energy loss function from the target chamber window to mid target.

3.3. Data Analysis of the Drift Chambers

This section is about the data analysis of the drift chambers, where the quality of the data taking and the efficiency of the drift chambers are checked.

3.3.1. BDC1/2 and FDC0

When a particle passes through a drift chamber, the gas in the chamber is ionized and the electrons drift towards an anode wire. From the position of the wire and the drift length of the particle, the incident reaction location is determined. The drift length is calculated from the drift time using a space-time conversion (STC), which is shown in Fig. 3.3 (b). The STC is obtained by integrating the drift time spectrum, Fig. 3.3 (a), assuming a uniform drift length distribution. Since the electric field is non-uniform towards the wire, it has a sharp peak towards higher channels. Due to symmetry reasons there are two possible directions from which the particle can drift to a wire. Therefore, one needs at least three layers of wires behind each other to determine the correct track with a linear fit. The BDC's and FDC0 consist of four X and four Y layers to determine the track. With a least square procedure a linear track is determined considering all eight possible particle positions and their 16 different combinations. The optimum track is a fit through the four true points and the differences of the track to the four positions is calculated. Those differences are referred to as residuals and they are used to determine the position resolution of the drift chamber. Therefore, the residuals are plotted against the drift length, which is shown for the first X layer of BDC1 in Fig. 3.4 (a). The projection on the residual axis, Fig. 3.4 (b), gives then the resolution of the drift chamber. Since BDC2 and FDC0 are build the same as BDC1 they are treated likewise. A summary for the position resolutions is given Tab. 3.2.

Table 3.2.: Position resolution (1σ) of the drift chambers

Drift Chamber	Position Resolution [μm] (axis)	
BDC1	73 (x)	74 (y)
BDC2	74 (x)	73 (y)
FDC0	82 (x)	82 (y)
FDC2	258 (x)	364(v)

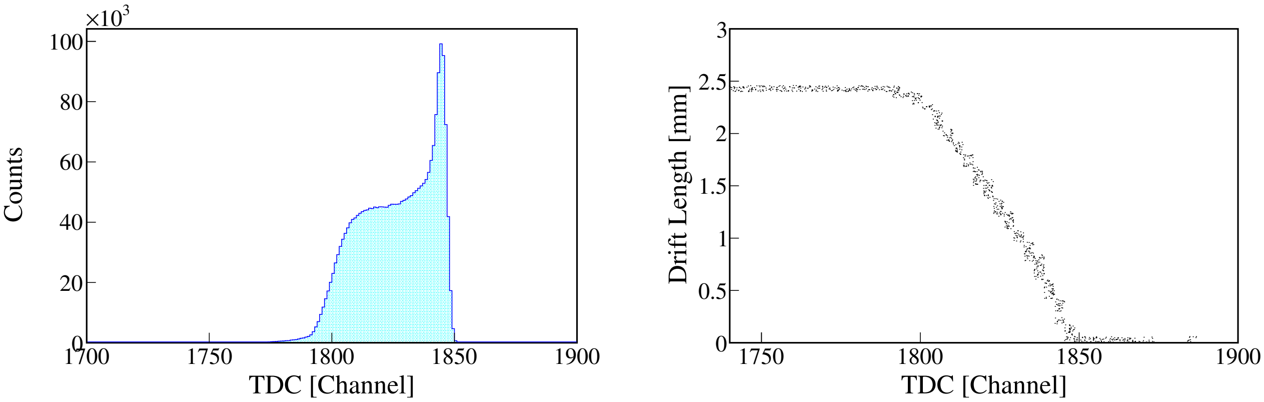

(a)

(b)

Figure 3.3.: (a) Drift time distribution for all BDC1 wires. (b) Space time conversion (STC) function for BDC1. The drift time distribution and STC function for BDC2 and FDC0 are quantitatively the same and not shown here.

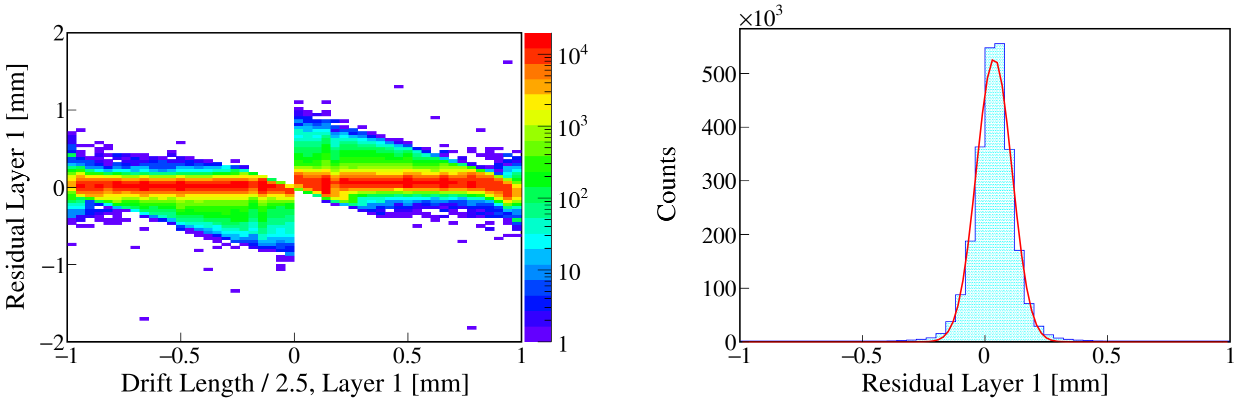

(a)

(b)

Figure 3.4.: (a) Residual with respect to the track against the drift length divided by the cell size (2.5 mm) for the first X layer of BDC1. (b) Projection on the residual axis to estimate the position resolution with a gaussian fit.

3.3.2. FDC2

Similar to the BDC, the functionality of the FDC2 is validated by studying the time-to-digital conversion distribution and space time conversion functions and the residuals of the calculated tracks. However, due to the different structure of FDC2, it is analyzed differently. The FDC2 layer scheme is XX'-UU'-VV'-XX'-UU'-VV'-XX'. The time-to-digital conversion distribution and space time conversion function are given in Fig. 3.5 (a) and (b). They are similar to the ones before, however more elongated due to the larger drift distance of 10 mm. Fig. 3.5 (c) shows in addition a correlation between the first XX' layer pair. The shape is unique due to a shift of the wire position between the two layers. It originates from the particles passing the wires with different angles and distances. This is a good check that FDC2 is working properly. Similar patterns appear for all other layer pairs of FDC2.

During the experiment the last UU' layers of FDC2 were not supplied with high voltage because they were sparking. Since the standard algorithm is calculating first the 1D track of the X, U and V layers separately, the two functioning U layers were not used, because a least square optimization is not possible with only two layers. Therefore, the track was only reconstructed using the X and V layers. The procedure is basically the same as for the BDC and FDC0 drift chambers, however the calculation is more elaborated due to the angle of the V planes. The final track is again compared with each points from the different layers and the residual is calculated. Fig. 3.6 (a) and (b) shows the residual against drift length plot for the first two X layers. In contrast to the BDC/FDC0 distributions one can see an offset shift and a worse resolution. These problems have been found systematically for all FDC2 layer pairs. In a discussion it was pointed out that the problems might arise from problems with the space time conversion function [65]. However, since the extracted values from FDC2 have been reasonable as can be seen in later sections, the problem was not pursued to a solution due to time constraints. It is expected, that fixing the issue could slightly enhance the resolution of the final results. The projected resolution plots are shown in Fig. 3.6 (c) and (d). The resolutions are also given in Table 3.2.

Note, that it would of course be possible to find out the correct positions for the functioning U planes using the track estimated from the X and V planes. However, the improvement of the resolution for the x-coordinate would be limited and so they were not calculated.

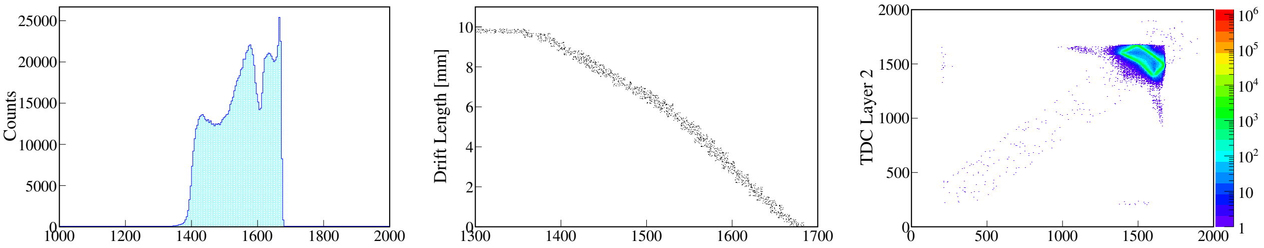

(a) (b) (c)

Figure 3.5.: (a) Drift time distribution for FDC2. (b) Space time conversion function for FDC2. (c) Correlation of the time-to-digital conversion distributions of the first XX' layer pair.

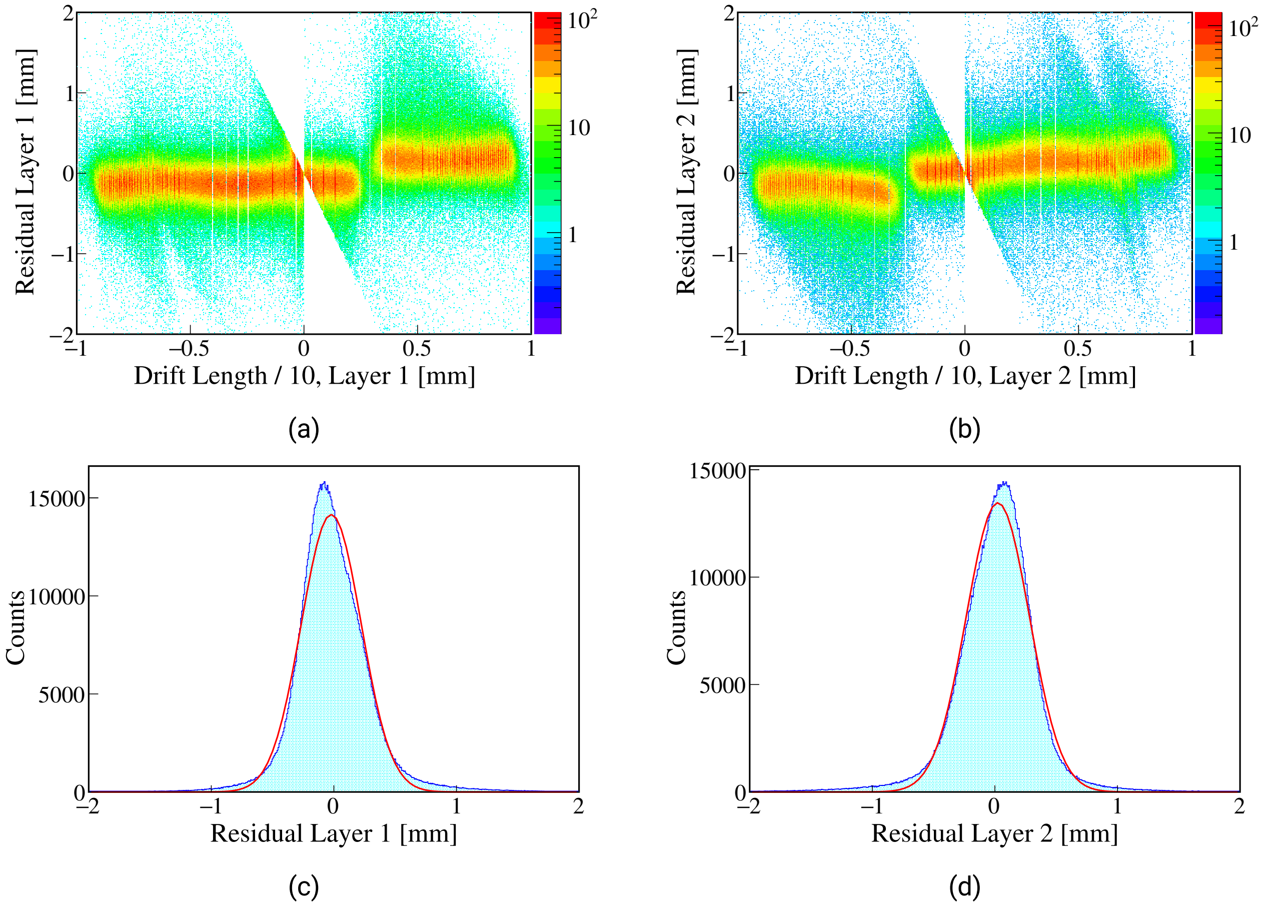

(a)

(b)

(c)

(d)

Figure 3.6.: Residual with respect to the track against the drift length divided by the cell size (10 mm) for the first X (a) and X’ (b) layer. Projection on the residual axis to estimate the position resolution with a gaussian fit for layer X (c) and layer X’ (d).

3.3.3. Alignment of FDC0

The exact relative position of FDC0 with respect to the BDC's was measured with limited precision. Therefore, the tracking of BDC1 and BDC2 is used to adjust relative alignment with the beam data. For the alignment, the $x_{\mathrm{BDC1,BDC2}}$ and $y_{\mathrm{BDC1,BDC2}}$ position coordinates of BDC1 and BDC2 are used to calculate the track of the particles. With the resulting tracks from the BDC's the position coordinates of the particles at FDC0 are determined. The calculated coordinates are then compared to the measured values x_{FDC0} and y_{FDC0} from FDC0 to specify the offset of FDC0. The offsets Δx_{FDC0} and Δy_{FDC0} with respect to the beamline are calculated using Eq. (3.1) and Eq. (3.2). Here, d_{BDC1FDC0} is the distance between BDC1 and FDC0 and d_{BDC1BDC2} is the distance between BDC1 and BDC2. The corrections for FDC0 are $x_{\mathrm{FDC0}} = 0.17\,\mathrm{mm}$ and $\Delta y_{\mathrm{FDC0}} = 0.5\,\mathrm{mm}$. The calculated values are used later for the reconstruction of magnetic rigidity $B\rho$ and flight length L of the particles.

$$\Delta x_{\mathrm{FDC0}} = x_{\mathrm{FDC0_{exp}}} - [x_{\mathrm{BDC1}} + \frac{d_{\mathrm{BDC1FDC0}}}{d_{\mathrm{BDC1BDC2}}} \cdot (x_{\mathrm{BDC1}} - x_{\mathrm{BDC2}})] \tag{3.1}$$

$$\Delta y_{\mathrm{FDC0}} = y_{\mathrm{FDC0_{exp}}} - [y_{\mathrm{BDC1}} + \frac{d_{\mathrm{BDC1FDC0}}}{d_{\mathrm{BDC1BDC2}}} \cdot (y_{\mathrm{BDC1}} - y_{\mathrm{BDC2}})] \tag{3.2}$$

3.3.4. Beam Position on the Target

The beam position on mid target is calculated from the position coordinates of BDC1 and BDC2, see Fig. 3.7 (a) for target runs and (b) for empty target runs. The target has a diameter of 30 mm. Therefore, only events within a diameter of 30 mm are considered for further analysis.

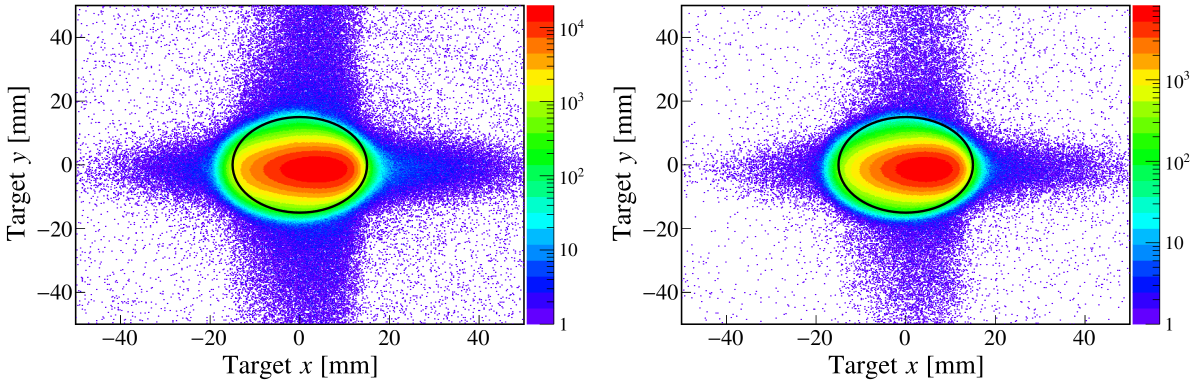

(a)

(b)

Figure 3.7.: Beam position on mid target for (a) target runs and (b) empty target runs. The black circle indicates the diameter of the target.

3.4. Reconstruction of $B\rho$ and the Flight Length L

For the calculation of the cross sections and the parallel momentum distribution (PMD) it is necessary to know the magnetic rigidity $B\rho$ and the flight length L of the particles. Those two quantities were not directly measured during the experiment. They also cannot be calculated straightforward with the Lorentz force, because the magnetic field of the large SAMURAI dipole magnet is not homogeneous. Therefore, simulations of the trajectories are done using an accurate magnet field map provided by RIBF. With the obtained simulated trajectories a multidimensional fit is done using the position coordinates of FDC0(x,θ_x,y,θ_y) and FDC2(x,θ_x). The fit functions are then used to reconstruct $B\rho$ and L with the experimentally measured position coordinates of FDC0 and FDC2.

For the simulation the software *smsimulator3.5* provided by our collaborators from *TiTech* [66] is used, which is based on *Geant4* [67]. The input parameters for the generated events are given in Table 3.3. The expected $B\rho$ mean value for ^{14}O is $B\rho(^{14}\mathrm{O}) = 2.44\,\mathrm{Tm}$, for ^{13}O and ^{13}N they are $B\rho(^{13}\mathrm{O}) = 2.2\,\mathrm{Tm}$ and $B\rho(^{13}\mathrm{N}) = 2.6\,\mathrm{Tm}$. Thus the input $B\rho$ is covering the experimental range. The position and angle coordinates have their origin at the target position. The coordinates are chosen to that they cover the target dimensions. Note, that the choice of angle coordinates from -20 mrad to 20 mrad covers the impact range of the beam on target. However, due to the reaction the angle distribution widens. The resolution of the PID was found to be much better for the range from -20 mrad to 20 mrad than for higher ranges. The issues with higher angles could be attributed to the flight lengths function. Simulations for the $B\rho$ function from -60 mrad to 60 mrad resulted in a similar momentum distribution as for the one from -20 mrad to 20 mrad. However, there was an offset in the momentum distribution. The offset gave rise to a deviation from the theoretical calculations, while the shape was again nicely reproduced (see Section 4.4). Therefore, the calculation with the range from -20 mrad to 20 mrad are applied for our momentum distribution. Of course, there will be final checks in the near future to confirm these results. In addition, several checks were already done, where the events smaller then -20 mrad and larger then 20 mrad were always consistent with the other data in the A/Q plots and the momentum distributions in the later sections.

500.000 ^{14}O particles are generated uniformly within the chosen limits. The magnetic field map for 1.5 T provided by RIBF is used for the simulation. The magnetic field is scaled with a factor of 0.99503 with SHT and 1.0068 without SHT to match the experimental magnetic field of 1.4858 T and 1.5102 T. An example for the resulting trajectories for ^{14}O, ^{13}O and ^{13}N is shown in Fig. 3.8. From the simulation the FDC0 and FDC2 position and angle, $B\rho$ and L of the particles are saved and then used for the multidimensional fit.

Table 3.3.: Simulation input parameters. The range of the position coordinates is chosen, so that they cover the range of target used in the experiment. The $B\rho$ is chosen so that it covers the range of momentum distribution of ^{14}O, ^{13}O and ^{13}N.

	Minimum value	Maximum value
Target x position [mm]	-15	15
Target θ_x angle [mrad]	-20	20
Target y position [mm]	-15	15
Target θ_y angle [mrad]	-20	20
$B\rho$ [Tm]	2.0	2.8

The experimental $B\rho$ and L are obtained with a *least square fitting* multidimensional fit from the trajectories [68]. The method is included in the *smsimulator3.5* software.

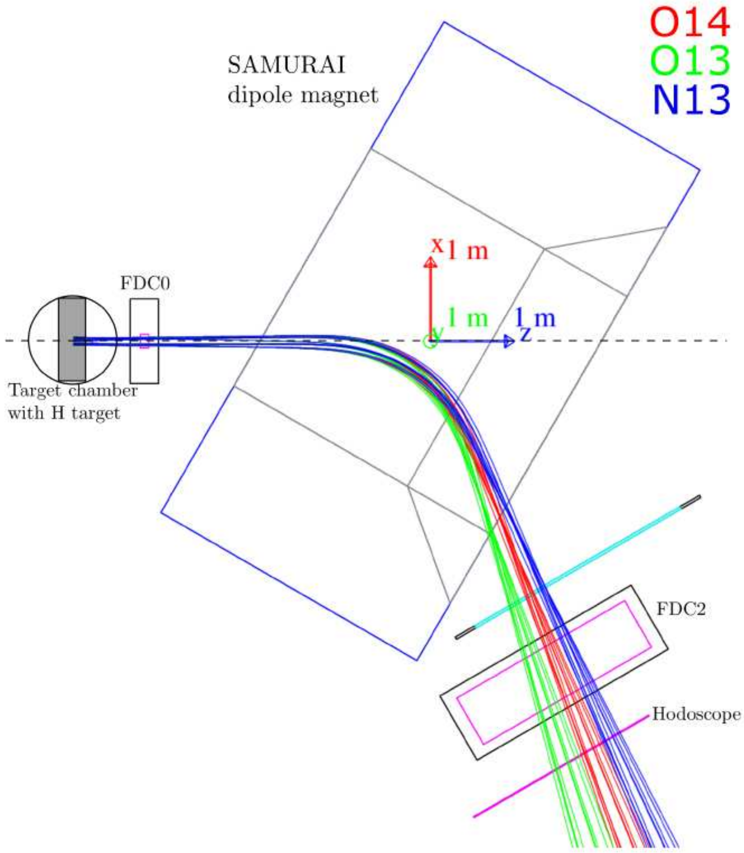

Figure 3.8.: Simulation of the trajectories ^{14}O (red), ^{13}O (green) and ^{13}N (blue) at the SAMURAI spectrometer.

The goal is to reconstruct not measurable quantities with a function, which depends on experimental measurable quantities. For our experiment, we want to know $B\rho$ and L of the particles, which were not measured experimentally and are our unknown quantities. To reconstruct them we measured the angle and position of the particle at FDC0 and FDC2, which are our measurable quantities. The position and angle of FDC0 and FDC2 depend on $B\rho$ and L and vice versa. The functions for $B\rho$ and L are obtained with a least square fitting procedure, which needs a large amount of sample data. We generated the sample data in the previous described simulation. A general idea of the fitting procedure is given in the following, which follows the description in Ref. [69].

Let D be the quantity of interest, which depends on the variables $x_1, ..., x_\mathrm{N}$ and has the the square error E. From simulation a sample (x_f,D_f,E_f) is generated. The multidimensional fit will determine the parameters c_l of the following equation

$$D_p(\mathbf{x}) = \sum_{l=1}^{L} c_l \prod_{i=1}^{N} p_{li}(x) = \sum_{l=1}^{L} c_l F_l(\mathbf{x}) \quad , \tag{3.3}$$

so that

$$S = \sum_{j=1}^{M} (D_j - D_p(\mathbf{x}_j))^2 \tag{3.4}$$

becomes minimal. $p_{li}(\mathbf{x}_l)$ can be monomials, Chebyshev or Legendre polynomials.

The quality of the fit is tested by inserting the simulated values into the $B\rho$ and L function and compare it to the corresponding value from the simulation. The result of this comparison is shown in Fig. 3.9. The figures show that the fit functions reproduce $B\rho$ and L with very small deviations from the simulated value in the region of interest. The fit converges for monomials with a maximum order of 4. For higher orders there was no improvement of quality. The minimum relative error is set to 0.01. A minimum needs to be given, because it is highly unlikely that the error becomes zero and thus the fit would not converge. The maximum number of monomial terms is set to 1000.

For the particle identification, the previous described simulation using ^{14}O particles is used. The precision of the functions is sufficient for the particle selection. For an exact determination of the parallel momentum of the residues, ^{13}O and ^{13}N are used as the input of the simulation. The other simulation and fit input parameters stayed the same. The results of the quality control plots are similar to the ones from ^{14}O and the output momenta changed slightly.

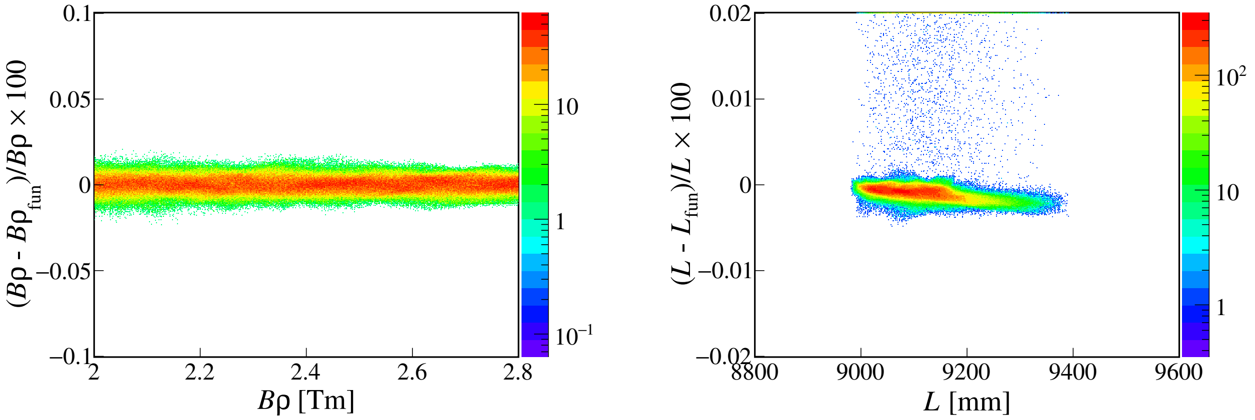

(a)

(b)

Figure 3.9.: Quality test for the $B\rho$ and Fl functions with SHT. A second simulation was performed, since the magnetic field was different for the runs with and without SHT. The results without SHT are similar to the ones shown here.

3.5. Calibration of the Hodoscope

The calibration of the hodoscope is done in two steps. First the relative calibration to align the time and charge offset of the different hodoscope bars. Secondly, the absolute calibration to get the correct Z and A/Q for the particle identification.

3.5.1. Relative Calibration

For the relative calibration the assumption is made, that events, which hit two neighboring hodoscope bars, have the same energy deposit and TOF. This is obviously only the case at the transition from one bar to another bar (see Fig. 3.10). Therefore, the position of the particles at hodoscope is calculated with the FDC2 coordinates and then only events in a range of ± 5 mm at the transition between two bars are selected. The charge and the time is then compared for those events, from which then an alignment factor is calculated for the charge and an offset constant for the time. The procedure is done repetitively until every bar is relatively aligned to bar 9 of the hodoscope, which is the bar with the most events during the experiment. A quality check of this procedure is done by looking at the charge and the TOF against the FDC2 X position (see Fig. 3.11). If the constants for the alignment are correct, the structures in the plots should be continuous. If there are "jumps" it means, that there is a transition from one bar to an other and that those two bars are not correctly aligned. This misalignment can happen, when there were only few measured events between two bars. It can then be corrected by adjusting the relative alignment manually.

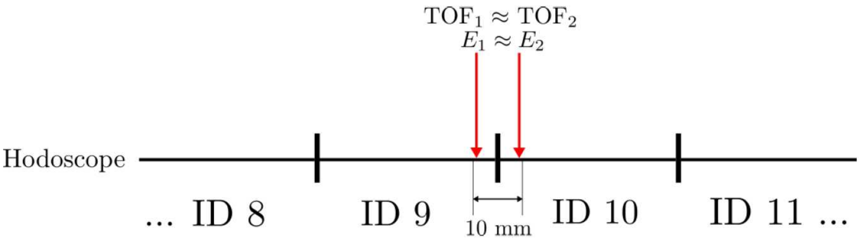

Figure 3.10.: Principle of the relative calibration of the hodoscope.

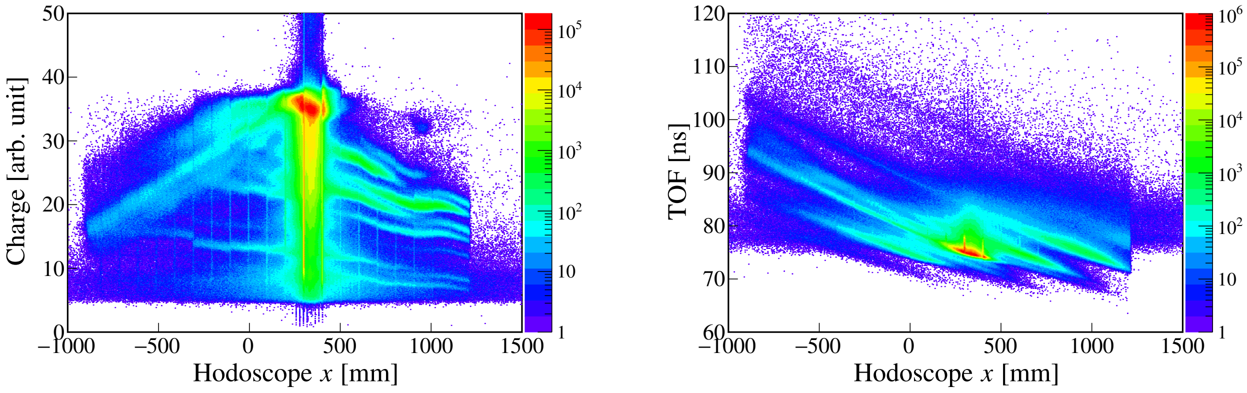

(a)

(b)

Figure 3.11.: (a) Charge and (b) TOF against the hodoscope x position of the particles as a quality check for the relative calibration.

3.5.2. Absolute Calibration

The absolute calibration of the hodoscope is done with $\Delta E - B\rho$–TOF method using the following equations:

$$\frac{A}{Q} = \frac{B\rho c}{\beta\gamma m_\mathrm{u}} \tag{3.5}$$

$$\mathrm{TOF} = \frac{L}{\beta c} \tag{3.6}$$

$$-\frac{\mathrm{d}E}{\mathrm{d}x} = 2\pi N_\mathrm{a} r_\mathrm{e}^2 m_\mathrm{e} c^2 \rho \frac{Z}{A}\frac{z^2}{\beta^2}\left[\ln\frac{2m_\mathrm{e}v^2}{I} - \ln(1-\beta^2) - \beta^2\right] \tag{3.7}$$

In Eq. (3.5) A is the atomic mass number and Q is the charge of the incoming particle, $B\rho$ is the magnetic rigidity of the particle, c is the velocity of light, $\beta = v/c$, where v is the velocity of the particle, γ is the Lorentz-factor and m_u is the atomic mass. With an A/Q of 1.75 for ^{14}O and the calculated $B\rho$, the velocity v of the particles is determined. v is then used with the calculated L to determine the TOF offset constant with Eq. (3.6). Note that additional slight corrections had to be applied for the TOF, so that the nuclei ^{13}O and ^{13}N are at their correct position. This was due to the slew correction, which was applied only on one hodoscope plastic scintillator. The slew correction is discussed later in Section 3.8.2.

In a second step, the measured charge of the hodoscope is calibrated to the atomic number of the measured nuclei. The charge z of the incident particle is calculated by using the Bethe-Bloch formula Eq. (3.7). Here, N_a is the Avogadro constant, r_e^2 is the classical electron radius, m_e is the electron mass, ρ is the density of the scintillator material, z is the charge of the incident particle in units of elementary charge e, I is the mean excitation potential, Z is the atomic number and A is the atomic weight of the absorbing material. For composite materials the effective values for A and Z are calculated by the sum over the single components:

$$Z_\mathrm{eff} = \sum a_i Z_i \tag{3.8}$$

$$A_\mathrm{eff} = \sum a_i A_i \tag{3.9}$$

The material of the plastic scintillator is BC408. It has a density of $\rho = 1.03289\,\mathrm{g/cm^3}$, a mean excitation potential of $I = 64.7\,\mathrm{eV}$ [70]. Furthermore, note that Eq. 3.7 is only valid for $M >> m_e$ due to various approximations. Here, M is the mass of the incident particle. Also corrections like the density effect and shell correction are not considered, because they are not relevant in the energy range of the experiment.

The values one calculates for z from the Bethe-Bloch formula are arbitrary and have to be assigned to the proper atomic number Z. Therefore, a first z versus A/Q figure is created. A projection on the z-axis of this plot is done. From this plot the corresponding values for each Z can be identified. The values for z are the mean values from a gaussian fit to each peak. With z and Z a quadratic translation function is created

$$Z = az^2 + bz + c \tag{3.10}$$

and a, b, c are constants to be determined. Note, that the amount of intensity of fluorescent light is only in first approximation proportional to the energy deposit. It usually depends on the energy and type of the incoming particle [71]. Thus, one should use as much nuclei with different Z as one can identify and a quadratic function instead of a linear fit. The procedure is repeated for every hodoscope plastic scintillator individually. However, for all plastic scintillators above ID 13 the constants a, b, c from ID 13 are used. The reason for this is, that most of the particles striking ID 14 and higher are stopped in the hodoscope and thus the calibration fails. This problem will be discussed further in Section 3.8, where a first particle identification plot is created based on the calibration in this section.

3.6. Plastic Scintillator Selection

For reducing the background of the experiment the plastic scintillators are used [72]. The selection is done with the hodoscope plastic scintillators and is described in the following. Each plastic scintillator is read out at the top and bottom side with a PMT. The light arriving at a PMT depends on the energy deposit and the position where a particle strikes the plastic scintillator bar. The amount of light arriving at the top and bottom side may be calculated by the following equation:

$$q_t = q_0 \exp(-\frac{L+x}{\lambda}) \tag{3.11}$$

$$q_b = q_0 \exp(-\frac{L-x}{\lambda}) \ . \tag{3.12}$$

Here, q_t and q_t are the measured amounts of light at the top and bottom plastic scintillator, respectively, q_0 is the initial amount of light, λ is the attenuation length, L the length of the plastic scintillator and x the position of the particle on the scintillator. Solving Eq. (3.11) and Eq. (3.12) for x leads to the expression

$$x = -\lambda \ln(\frac{q_t}{q_b}) \ . \tag{3.13}$$

In addition, the timings t_t and t_b of the charge signals in both scintillators are measured and can be used to deduce x with the effective light propagation velocity in the scintillator v

$$x = -\frac{v}{2}(t_t - t_b) \ . \tag{3.14}$$

By equating Eq. (3.13) and Eq. (3.14) and simplifying the result one gets the following equation

$$v(t_t - t_b) = \lambda \ln(\frac{q_t}{q_b}) \ . \tag{3.15}$$

Thus, there is a linear relationship between the two measurable quantities $t_t - t_b$ and $\ln(q_t/q_b)$ and events from physical particles fulfill Eq. (3.15). This linear relationship is used for the background removal, when plotting those two quantities in Fig. 3.12. The removed particles by this selection amount to 0.6(1) % and will be considered for the cross section correction.

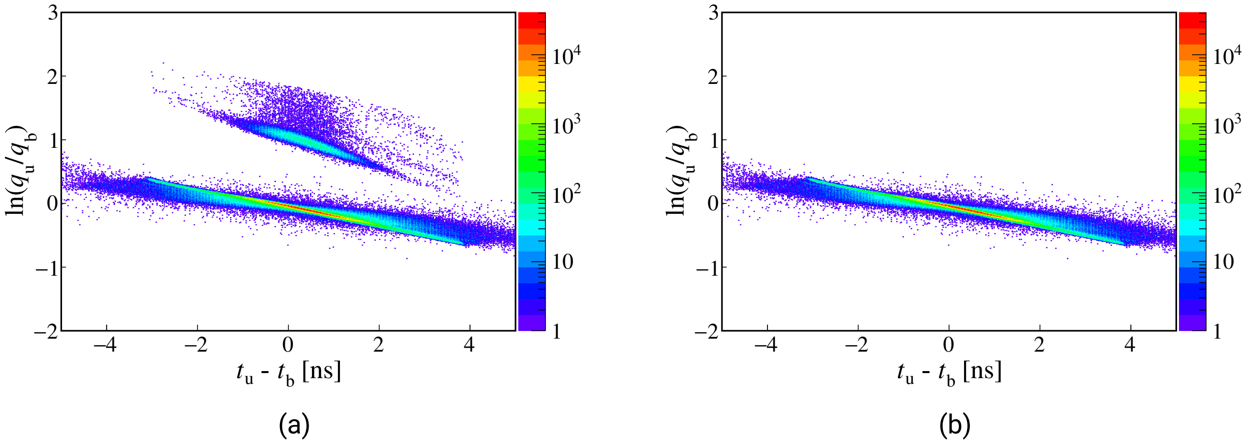

(a)

(b)

Figure 3.12.: Noise removal using the plastic scintillator with the ID8 of the hodoscope. (a) All registered events, (b) Registered events without the noise. The same selection method was applied on all plastic bars of the hodoscope.

3.7. Efficiency of the Detectors

The efficiencies of the drift chambers and the hodoscope plastic scintillator during the experiment are estimated. They were estimated by comparing registered events in neighboring detectors:

$$E_2 = \frac{N_1 \cap N_2}{N_1}$$

Here, E_2 is the efficiency of detector 2 and N_1 and N_2 the number of events registered at detector 1 and 2, respectively. FDC0 to BDC2,FDC2 to the hodoscope and the hodoscope to FDC2 were compared like this. All detectors have at least an average efficiency of 98.4 % or higher. The efficiencies are given in Table 3.4. They did operate well during the whole experiment. The efficiency of the detectors has to be considered for the cross section, because of the loss of ^{13}O and ^{13}N. However, a direct consideration is difficult, because particles can also be lost in between the detectors due to reactions with beam line material. It is then not know, if the the particle was not measured, because it was lost in the beamline or due to a detector not measuring it. This is especially the case for the detector FDC0, where no other detector is really close and much material is between FDC0 and BDC2. Therefore, the estimation will be indirectly in Section 3.10.2, where the beam loss due to beam line materials is described. Note that BDC1 and BDC2 were used to calculate the beam position on the target. All events which are not detected by them are removed from the selection on the target diameter. Thus, their efficiency is not relevant for the further analysis.

Table 3.4.: Average detection efficiency for ^{14}O of the used detectors in the SAMURAI experimental area: FDC0, FDC2 and the hodoscope.

	FDC0	FDC2	Hodoscope
Efficiency [%]	98.97	99.29	98.41

3.8. Particle Identification

3.8.1. Standard Particle Identification

In a first attempt for the particle selection a PID is created with the standard approach by calculating A/Q from the equality of the Lorentzian and centrifugal force and Z via the Bethe-Bloch-formula. The result is shown in Fig. 3.13. The residues can be clearly identified. However, there are some difficulties for a straightforward residue selection. The additional treatment for the shown PID and the final procedure for the selection of ^{13}O and ^{13}N are explained in the following sections.

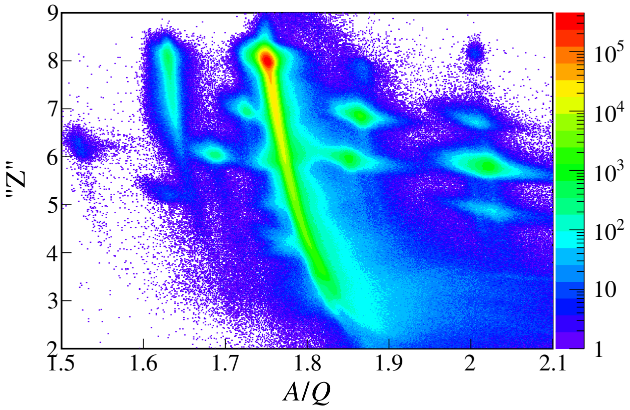

Figure 3.13.: PID with the standard $\Delta E - B\rho-$ TOF approach.

3.8.2. Slew Correction

Due to the use of a leading edge discriminator the TOF depends on the deposited energy of the particles. Therefore, the so called slew correction is applied by analyzing the particles, which hit two adjacent bars. Naturally, the signals of both bars have a different amplitude, but the same TOF. Unfortunately, only the central plastic scintillator with ID9 had enough events shared with a neighboring plastic scintillator ID8 for enough statistics for a good enough fit. Therefore, the same slew correction is applied for all hodoscope plastic scintillator. If enough statistics is there, one should usually apply the calibration for each plastic scintillator individually, because it changes. However, it is a good enough approximation to improve the quality of the PID and simplify the residue selection. It has no effect on the quality of the results, since the momentum distribution is calculated independently of this correction. The time of flight correction $\Delta\text{TOF}_{\text{sc}}$ is determined by fitting the following function to the selected events. It depends on the energy loss in the hodoscope ΔE with the parameters a, b and c:

$$\Delta\text{TOF}_{\text{sc}} = a + b \cdot \Delta E^{c} \quad . \tag{3.16}$$

The constants are determined to be $a = 70.5075$, $b = 15.0648$ and $c = -0.432171$. The $\Delta\text{TOF}_{\text{sc}}$ is subtracted from the calibration TOF and the A/Q is recalculated. The new PID is given in 3.14.

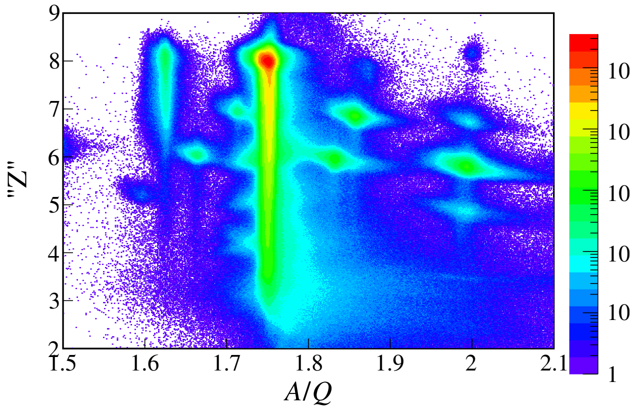

Figure 3.14.: PID with the standard $\Delta E - B\rho -$ TOF approach and applied slew correction.

3.8.3. Uncorrelated FDC Events

In the PID there are elliptical background contaminations. They appear for A/Q from 1.7 to 1.79 at "Z"= 3,4,5 and 6. They can be seen in Fig. 3.15 (a) for the target PID and in (b) for the empty target PID of plastic scintillator ID11. This background contamination can slightly overlap with the residue ^{13}N, which is shown in detail later. The origin of the background could not be found during the analysis. However, it is shown in the following, that the background does not originate from reactions upstream of the SAMURAI dipole magnet.

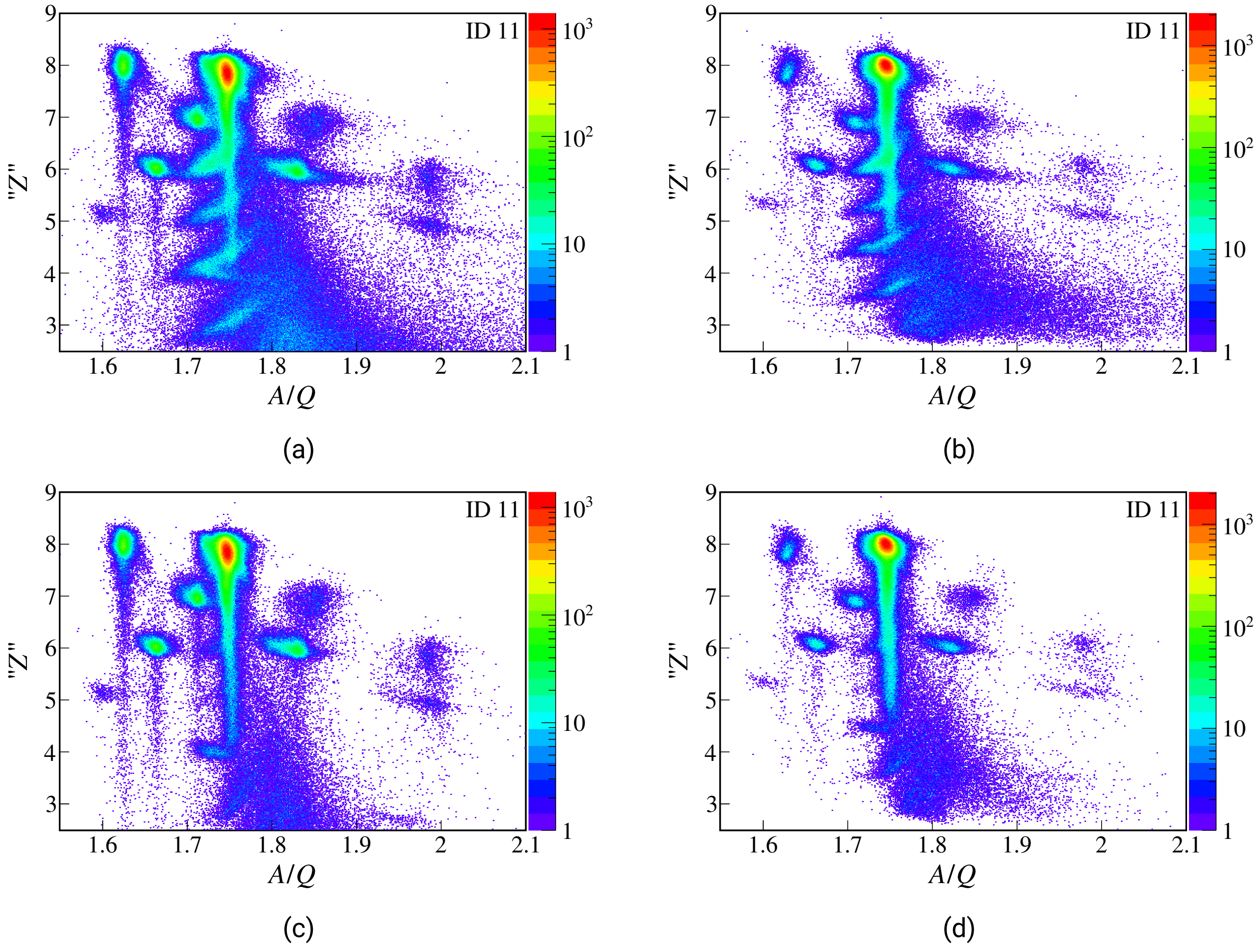

(a)

(b)

(c)

(d)

Figure 3.15.: PID's for hodoscope bar 11 without using the selection from Section 3.8.3 for runs with SHT (a) and without SHT (b). Elliptical contaminations can be seen for A/Q from 1.7 to 1.79 at "Z"= 3,4,5 and 6. PID's with the selection from Section 3.8.3 for runs with SHT (c) and without SHT (d).

To prove that the elliptical background is not relevant for the analysis FDC0 θ_x and FDC2 θ_x are used. Fig. 3.16 shows the angle θ_x of FDC0 against the angle θ_x of FDC2 for ID11 of the plastic scintillator from the hodoscope. Usually, those two quantities are correlated, which is also true for most of the events in this experiment. The correlation of those two quantities is shown with Geant4 simulations in Fig. 3.17. In the figure, the correlation of the nuclei ^{14}O with the magnetic field strength of the target runs is given. The results for other isotopes such as ^{13}O and ^{13}N and the empty target run magnet field are similar, with only slight differences in the slope of the correlation and the offset of the angle FDC2 θ_x.

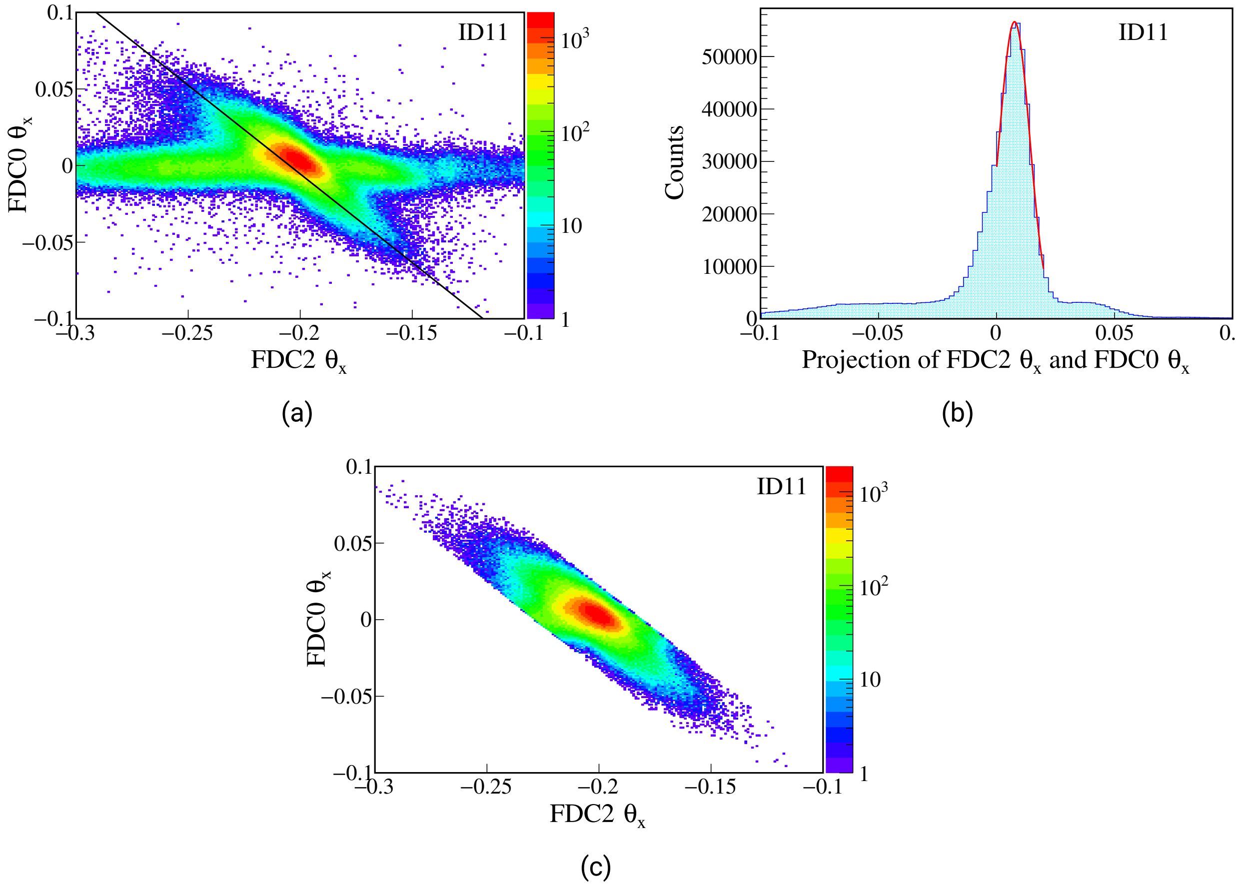

(a)

(b)

(c)

Figure 3.16.: Selection of the events using FDC0 θ_x and FDC2 θ_x for hodoscope ID 11. (a) All events are displayed for ID 11. A linear function is drawn through the correlated events. (b) The projection of the events on the linear function and a gaussian fit on the resulting spectrum. (c) The remaining events after rejecting all events outside of the 3σ environment of the gaussian projection fit.

However, in the experimental data there are many uncorrelated events. The horizontal uncorrelated events have a significant impact on the ^{13}N selection in the particle identification. The selection by plotting FDC0 θ_x against FDC2 θ_x is the best way, to show that those events are not relevant for the analysis. For the selection a linear function is plotted along the correlated events Fig. 3.16 (a). All events are then projected onto this line and a gaussian fit is applied. All correlated events with a 3σ environment are selected and most of the uncorrelated events will get rejected. The remaining events are show in Fig. 3.16 (c).

Compared to Fig. 3.15 (a) and (b) most of the background contamination is gone in Fig. 3.15 (c) and (d). The rest of the background is due to the continuation of the uncorrelated events in Fig. 3.16 behind the correlated events, which cannot be removed like this.

Note, that the selection process described in this section is performed to display the nature of these events further. It is not used for the selection ^{13}O and ^{13}N. The reason, why it is not used, is, that there are too many uncertainties in the selection and the overlap is strong. Some bars have a large overlap of ^{14}O, ^{13}O and ^{13}N, which are slightly shifted against each other and so it is difficult to

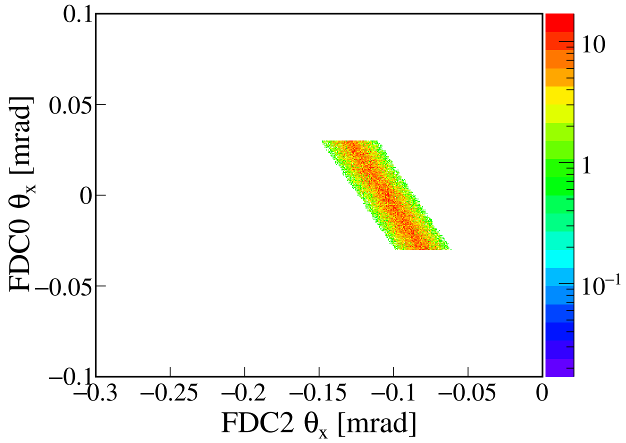

Figure 3.17.: Correlation between FDC0 θ_x and FDC2 θ_x from Geant4 simulations.

disentangle them. It leads sometimes to situations, that a 5σ selection must be applied for certain plastic scintillators to collect all correlated events instead of 3σ as in the example. However, an identification without the selection is possible since most of the background is subtracting for target and empty target runs. This is proven in Fig. 3.18. Here, FDC0 θ_x and FDC2 θ_x are displayed for all hodoscope plastic for runs with SHT (a) and without SHT (b). The horizontal background shows a repetitive pattern. This pattern can be reproduced by projecting both plots on the FDC2 θ_x axis in Fig. 3.18 (c). One can see nicely, that the repetitive pattern of runs with SHT (blue) and without SHT (green) is equivalent. The difference of the peak in the middle is due to events reacting at the target.

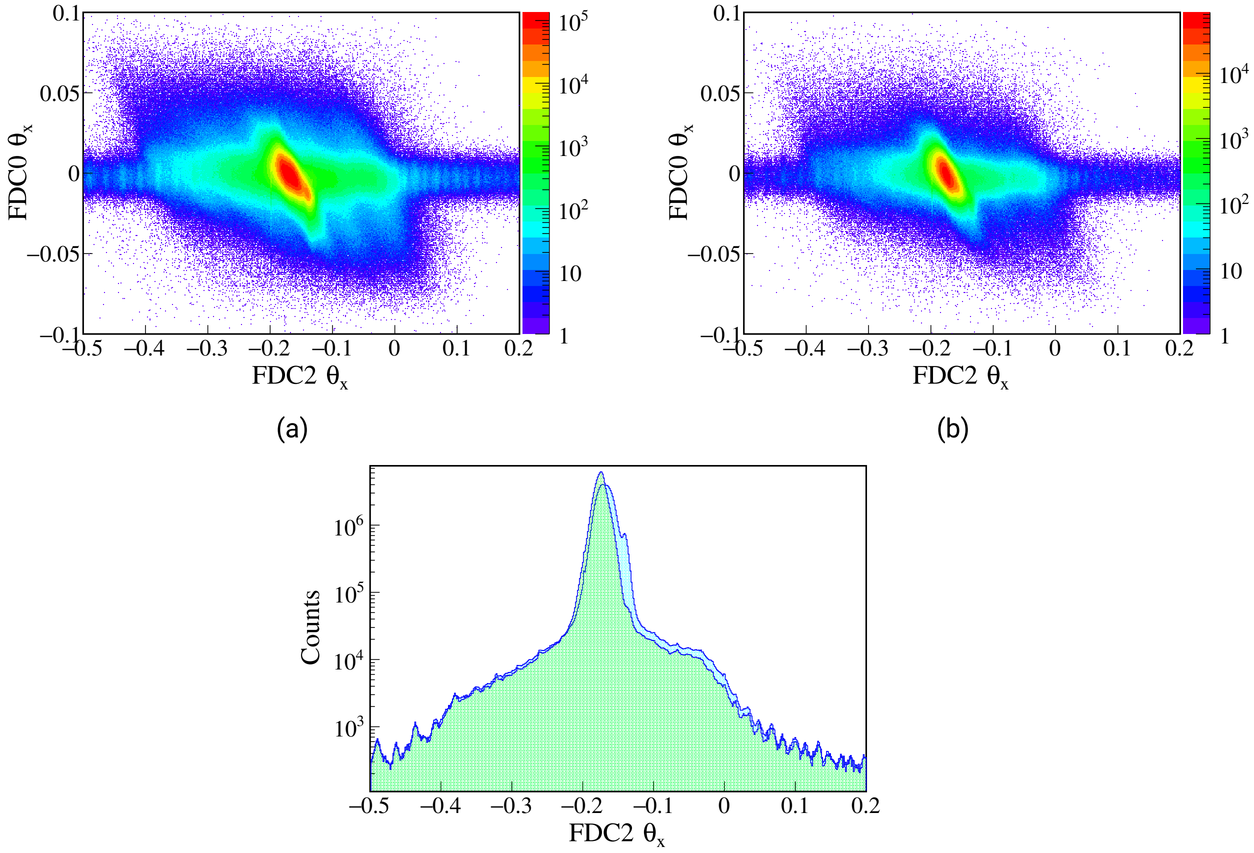

(a)

(b)

(c)

Figure 3.18.: FDC0 θ_x and FDC2 θ_x correlation for (a) runs with SHT and (b) runs without SHT. (c) Projection of the plots (a) and (b) on the horizontal FDC2 θ_x axis. The distribution in blue and green are for with SHT and without SHT, respectively.

3.8.4. Particles Stopping in the Hodoscope

The main issue for a particle identification is visible on the full PID in Fig. 3.19. ^{14}O and ^{13}O show both large tails and ^{13}N also a minor one. The tails stem from nuclei, which interact strongly or even stop in the hodoscope. Fig. 3.20 (a) and (b) shows the momentum against the hodoscope ID for ^{13}O and ^{13}N. The black line indicates the momentum threshold 5090 MeV/c and 4707.8 MeV/c for ^{13}O and ^{13}N respectively, when the residues stop in the plastic. The threshold was calculated using *LISE++*. For ^{13}N only a small part of the residues stop completely in the hodoscope, while most of the ^{13}O particles stop in the hodoscope. The difference is due to the different atomic number Z, which significantly impacts the energy loss. Note, that the black line only gives the threshold for the particle to stop completely in the hodoscope. The stopping power is higher for low momentum particles. When a particle passes through the plastic scintillator slowly, the interaction with the material becomes more likely and the particle looses more energy. The assumption of constant v in the usual Bethe-Bloch formula is not valid anymore and one would have to integrate over the energy. Therefore, the Z calibration is "smeared". The smearing is from the hodoscope ID's 14 and higher, which use the calibration constants of ID 13 and where the calibration process from the previous section fails. Due to this smearing ^{13}O events overlap with other isotopes and make a selection with this PID difficult.

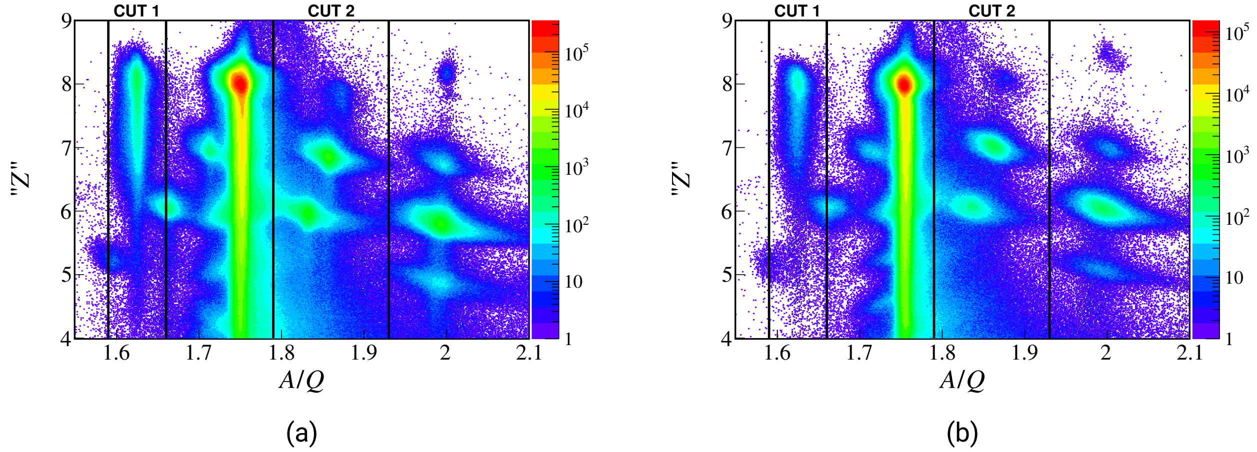

Figure 3.19.: "Z" versus A/Q plot for target (a) and empty target (b) runs. Usually, this plot is used for the PID. However, due to the energy loss of the particles in the hodoscope the different nuclei have significant tails, which overlap with other nuclei. Thus, a "clean" separation is not possible like this.

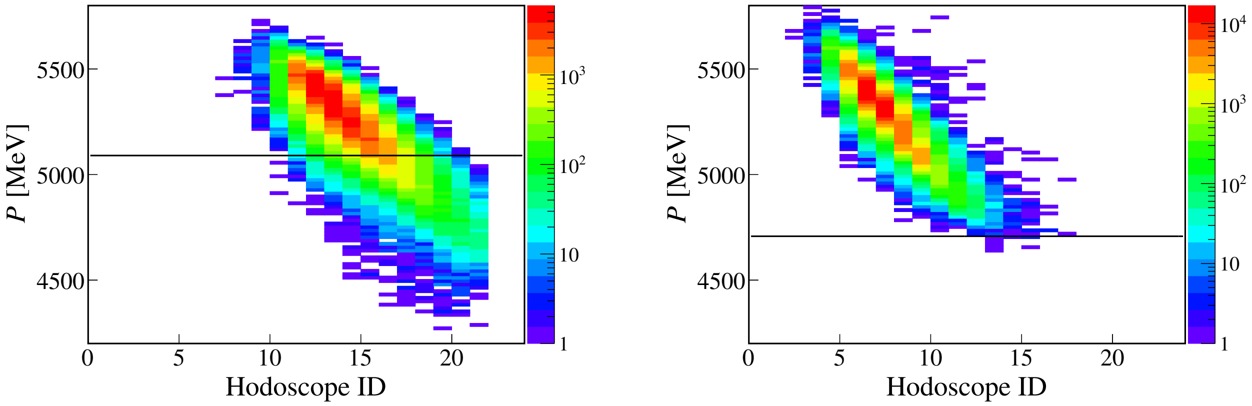

(a)

(b)

Figure 3.20.: Momentum against the hodoscope bar ID for (a) ^{13}O and (b) ^{13}N. The black line indicates the threshold at which momentum a particle would completely stop in the hodoscope.

3.8.5. Selection of ^{13}O and ^{13}N

Therefore, the PID is done by plotting the energy loss in the hodoscope against the velocity of the particles in Fig. 3.21 for (a) ^{13}O and (b) ^{13}N. In the plots, the A/Q is limited to $1.59 < A/Q < 1.66$ for ^{13}O ($A/Q = 1.625$) and $1.79 < A/Q < 1.93$ for ^{13}O ($A/Q = 1.867$) to simplify the selection of the residues. A/Q is calculated with the $B\rho-$TOF method. In both plots the ^{13}O and ^{13}N events consist of two parts. In the first part the events are correlated. This is when the residues are stopped in the hodoscope and the Bethe-Bloch formula for a constant v is not applicable anymore. The energy loss is proportional to the kinetic energy. The second part are the anti-correlated events. In this case, the events pass through the plastic and the energy loss can be calculated with the Bethe-Bloch formula. For the selection of the residues, the following procedure is applied. Two linear functions are drawn through the residue events. The first one is drawn through the correlated events, the second one through the anti-correlated events. The parameters are summarized in Table 3.5. All events are projected onto these two lines. An exception is made for the ^{13}N correlated events. Here, a selection is done on the lower part of the events, because otherwise the overlap with anti-correlated is too strong and a fit not possible. The resulting projection SHT spectra are shown exemplary in Fig. 3.22 (a) and (b) for ^{13}O and Fig. 3.22 (c) and (d) for ^{13}N. A gaussian fit is applied on each of the projections. The residue events are then selected in a 3σ environment of those fits. The events selected by this procedure are within the black lines shown in Fig. 3.21 (a) and (b). For the selection error estimation the σ from the fit is changed within the fit error limits. This results in deviations in the selection of 0.02 % to 0.29 %. From applying the 3σ environment selection 0.3 % are usually excluded. However, this applies only for a perfect gaussian distribution. Since the distributions are not ideal a maximum error of 0.3 % is assumed for the selection, which is larger than the deviation from the σ fitting error.

Table 3.5.: Linear function parameters for the projection.

Residue	Target	Events	Slope [1/(mm/ns)]	Offset [arb. unit]
^{13}O	Yes	Correlated	0.996336	-85.9048
^{13}O	Yes	Anti-correlated	-1.73623	249.961
^{13}O	No	Correlated	0.98318	-85.7325
^{13}O	No	Anti-correlated	-1.17274	179.144
^{13}N	Yes	Correlated	1.14385	-98.3814
^{13}N	Yes	Anti-correlated	-0.703738	112.491
^{13}N	No	Correlated	0.971551	-80.2785
^{13}N	No	Anti-correlated	-0.580983	97.6513

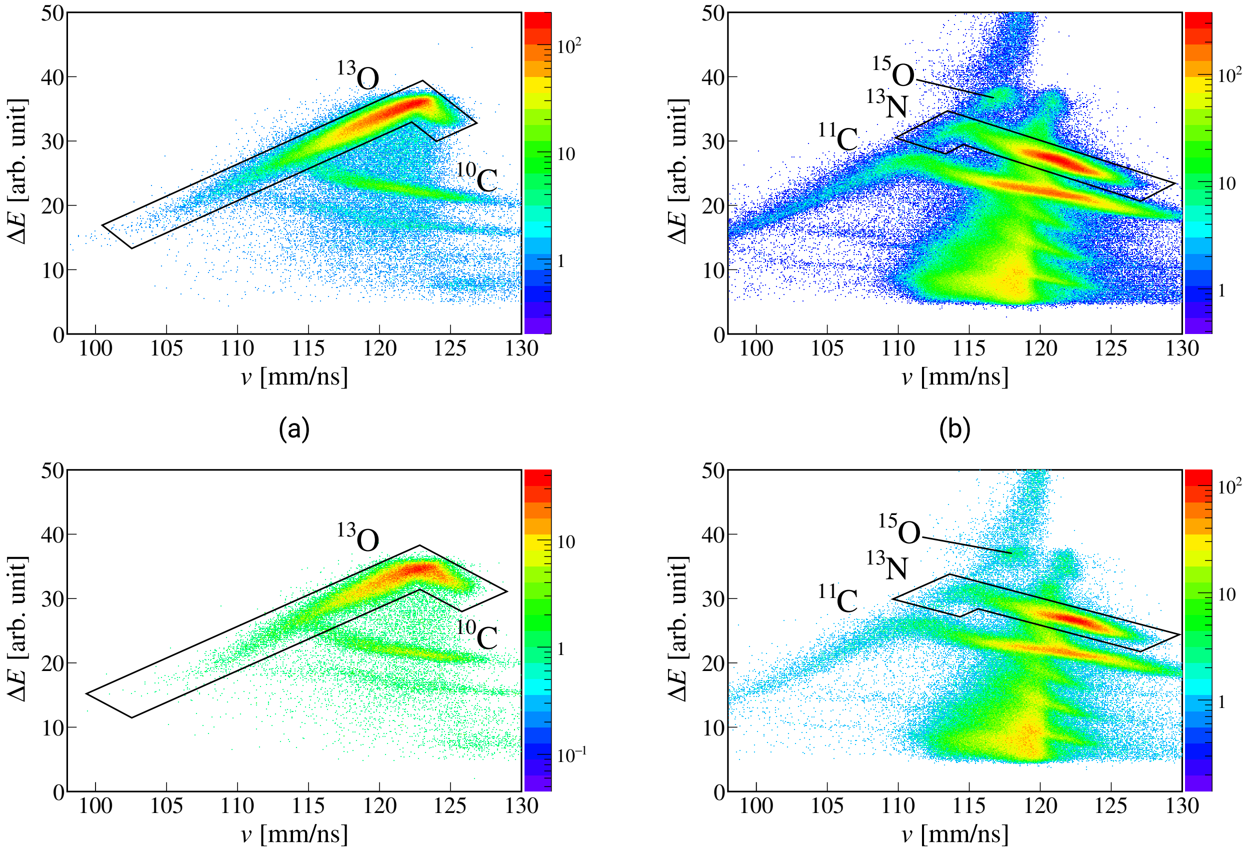

(a) (b)

(c) (d)

Figure 3.21.: Charge against the velocity for the identification of (a) ^{13}O and (b) ^{13}N with SHT. (c) and (d) are the corresponding selection without SHT .Figure (a) and (c) are limited by CUT1 and figure (b) and (d) are limited by CUT2 from Fig. 3.19.

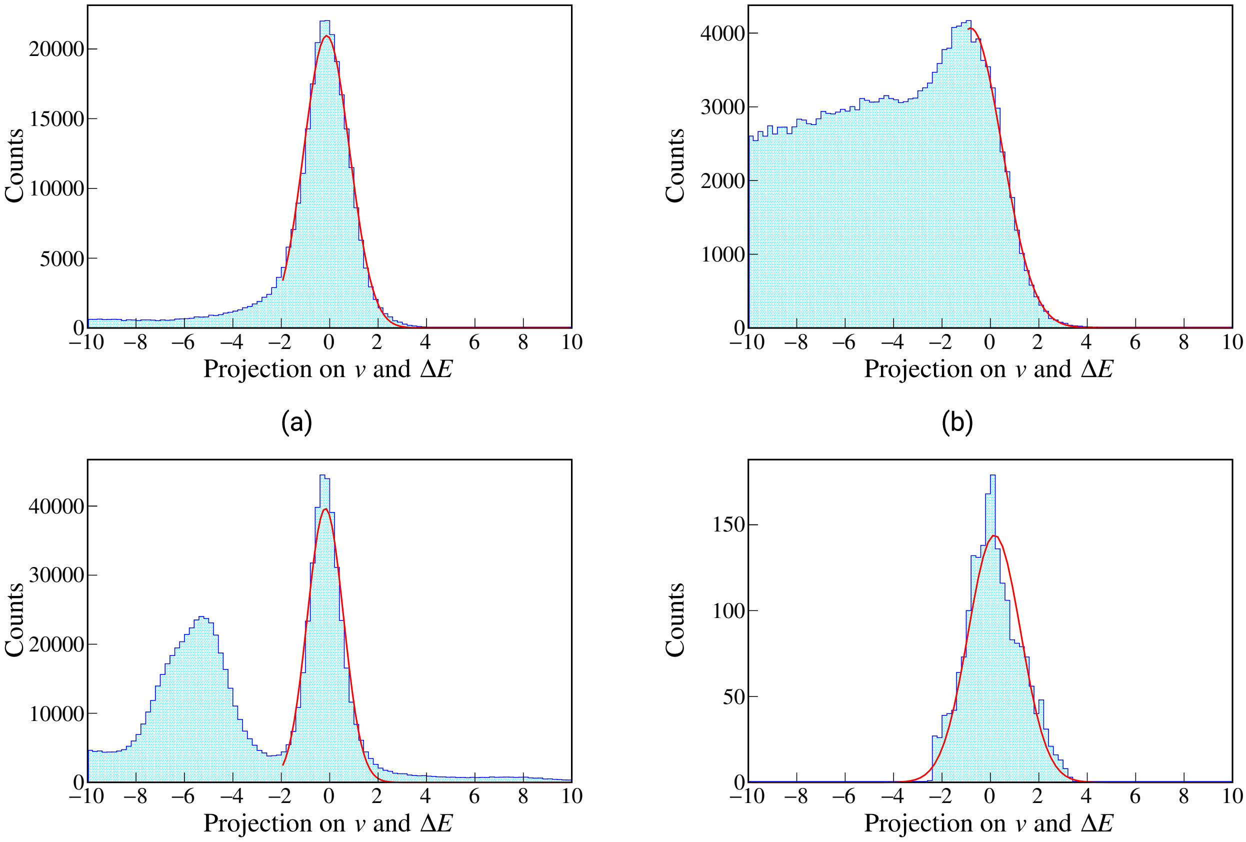

(a)

(b)

(c)

(d)

Figure 3.22.: Projection of the events in Fig. 3.21 (a) and (b) on the respective linear functions given in Table 3.5.(a) and (b) show the projection on ^{13}O correlated and anti-correlated events. (c) and (d) are the corresponding pots for ^{13}O. Note, for the projection on (d) a preselection of the correlated was done, because otherwise the anti-correlated part would have overlapped too strong.

3.8.6. Validation of the Residue Selection

Here, the previous applied selection are verified by comparing the A/Q distributions for runs with SHT and without SHT. The comparison is given in Fig. 3.23. The presented figures prove that selection is good and the distribution subtract nicely. However, there are still some contaminations left. They will be treated in the next section.

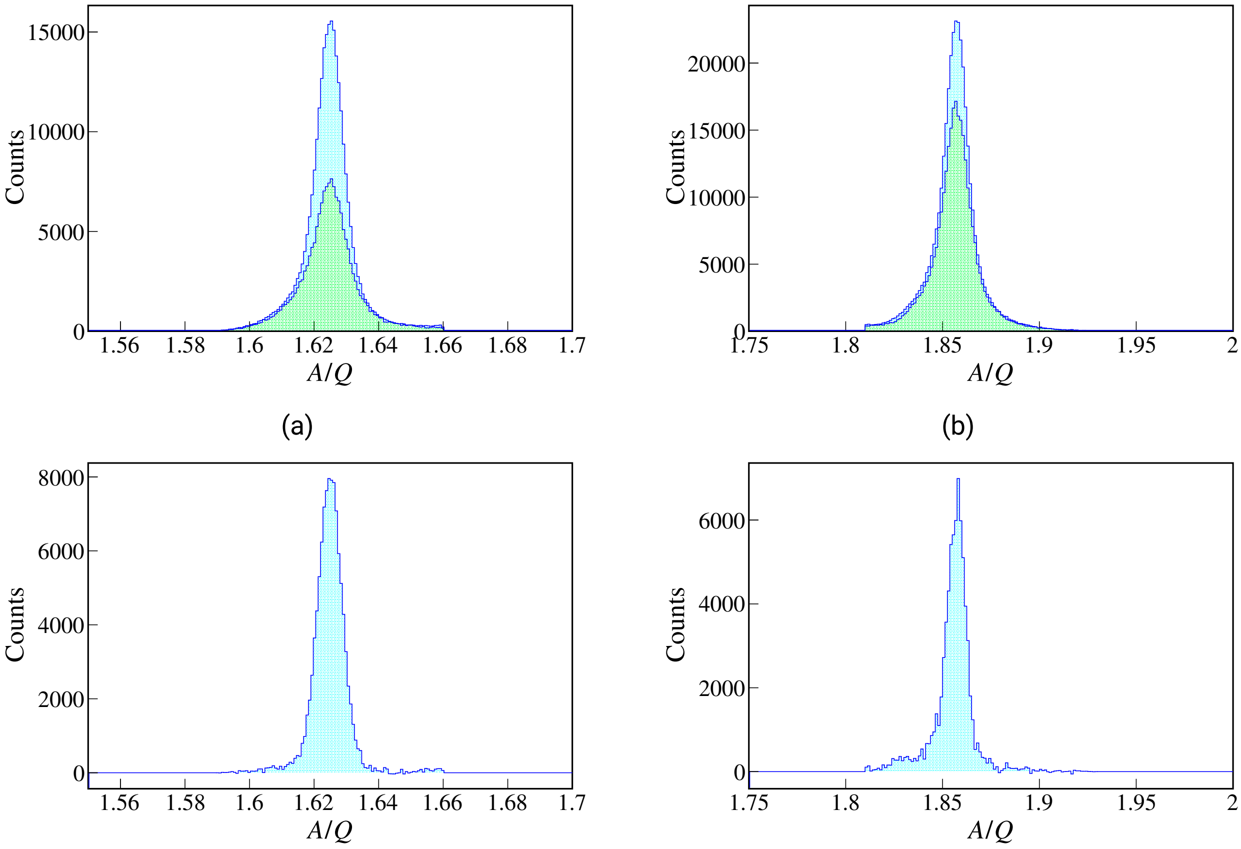

(a)

(b)

(c)

(d)

Figure 3.23.: (a) and (b) show the A/Q distributions with SHT (blue) and without SHT (green) for ^{13}O and ^{13}N, respectively. (c) and (d) are the respective subtracted spectra.

3.8.7. Additional Selection Corrections

Additional selection for ^{13}N

As mentioned in Section 3.8.3 the uncorrelated events in the FDC0 θ against FDC2 θ plot were not excluded due to uncertainties. However, part of those events overlap with the residue ^{13}N in the particle identification plots. In Fig. 3.24 (a) the effect of those events become visible, where a small peak is visible in the range of 5100 MeV/c - 5400 MeV/c.

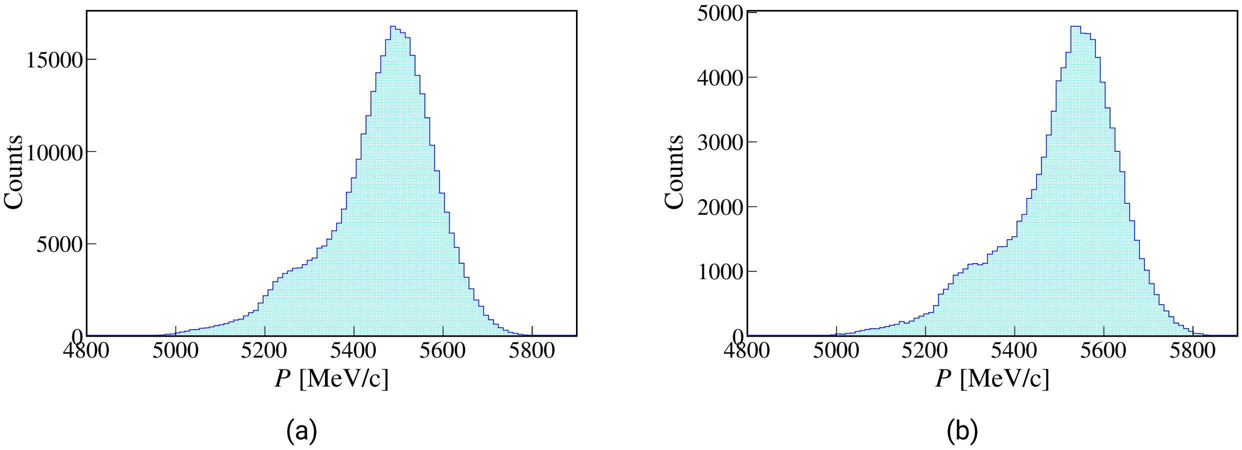

(a)

(b)

Figure 3.24.: PMD of ^{13}N after the PID for (a) runs with SHT and (b) runs without SHT.

Those events can be removed by an additional selection. Therefore, ΔE against A/Q for hodoscope (a) ID 8 and (b) ID 9 is plotted in Fig. 3.25. Here, only events with a momentum below 5400 MeV/c are considered. The black lines indicates the new selection. All events below the black lines are rejected, because they are not ^{13}N. Note, those events were not rejected in the previous selection, because other hodoscope ID's have a similar energy loss and overlap with this contamination. The removal is also applied for ID 10 and 11, but the contamination there is much less. With the presented selection, the small bumps around 5400 MeV/nucleon disappear and the tails are now continuous. The results are presented in 3.26.

The figures in Fig. 3.25 are taken from the runs with SHT. The same selection with a slightly different line is applied and a momentum below 5450 MeV/c for the runs without SHT.

However, this selection is not necessarily mandatory for the calculation of the cross section and a correct momentum distribution. When the A/Q selection limit of the PID preselection is changed from 1.79 to 1.81 and only the energy loss in the hodoscope against the velocity selection is applied, the difference in the cross section is only 0.04 mb. This is consistent with Fig. 3.18, where the background of runs with and without SHT is similar.

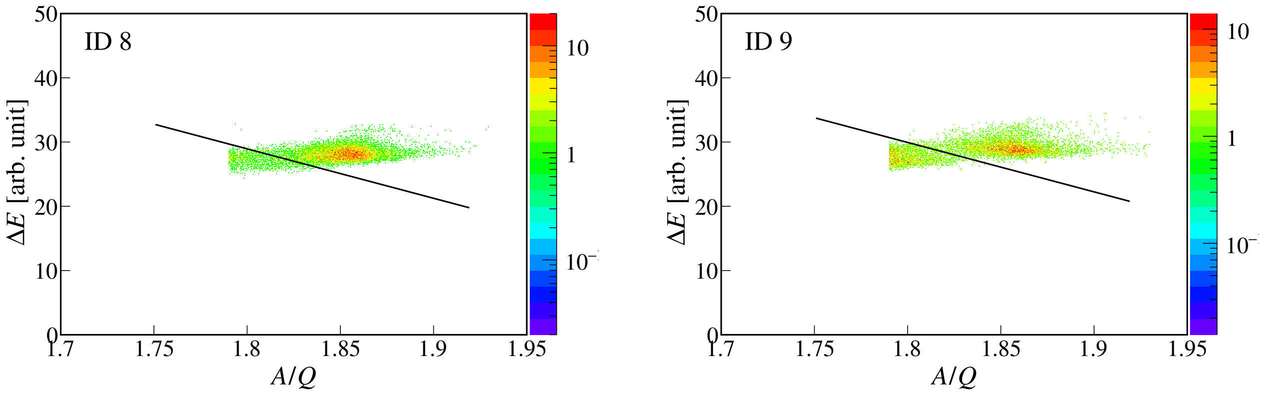

(a)

(b)

Figure 3.25.: ΔE against A/Q for hodoscope (a) ID8 and (b) ID9. Only events with a momentum below 5300 MeV/c are shown. Events below the black line are rejected, because they are not ^{13}N.

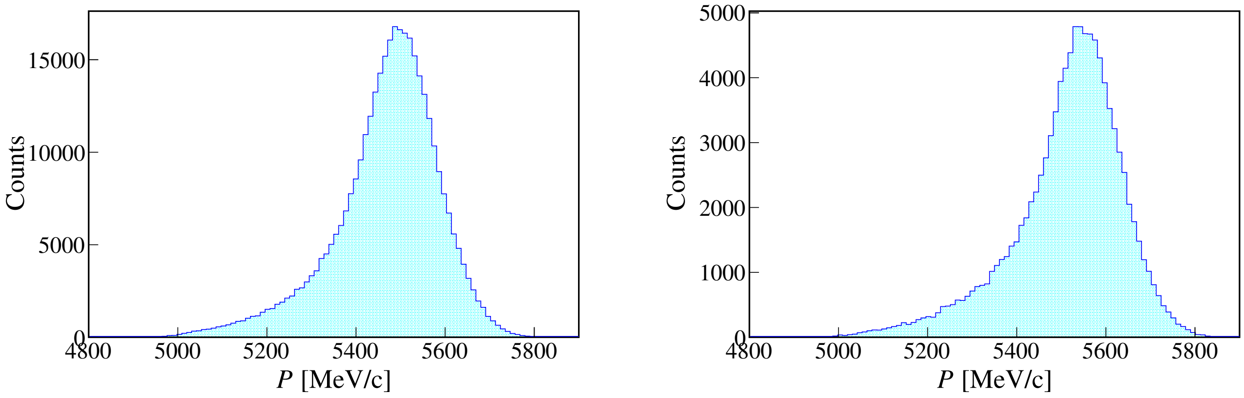

(a)

(b)

Figure 3.26.: PMD of ^{13}N with the additional selection for (a) runs with SHT and (b) runs without SHT. Note, the two distributions have not been normalized yet and represent different total run times.

Additional selection for ^{13}O

For ^{13}O a similar selection must be applied, because there is some ^{11}C left. It is removed again with a ΔE against A/Q plot. An example is given for the plastic scintillator with the ID 15 in Fig. 3.27. The ^{11}C is straightforward removed within the black lines. For the other plastic scintillators with the ID's 14,16,17 and 18 the ^{11}C is also removed like this. The background effect on ^{13}O in not as strong as the one for ^{13}N described in the previously. Therefore, there is no large impact on the momentum distribution visible and thus no such plots are given here. Note, that in fact this selection would not even be mandatory, because ^{11}C is canceling for the distribution with and without SHT.

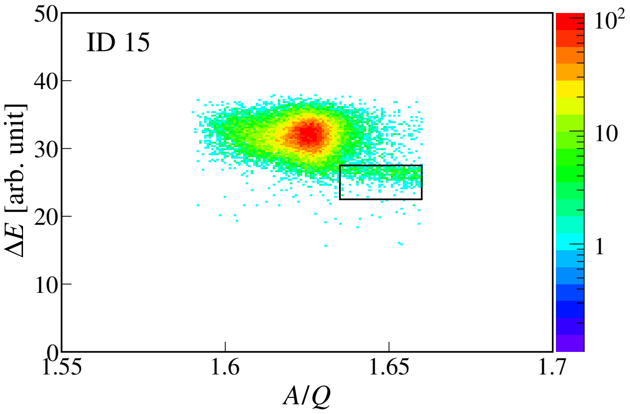

Figure 3.27.: ΔE against A/Q for the removal of ^{11}C. The events within the black lines are removed.

3.9. Target Density and Thickness

The density of the target was determined by constantly monitoring the temperature of the target cell during the experiment. A constant density is important, since the calculated cross section depends on it. Fig. 3.28 (a) shows the temperature profile during the experiment. The target cell temperature was constantly on 9 K. One steep fall of is in the graph, but it is probably due to a network error. The temperature of 9 K can then be translated to a density with Fig. 3.28 (b). Since the thermometer was only near the target cell and not at the target cell, it is expected that the target was below 9 K. The density curve is nearly constant below 9 K and so the density is constant during the experiment with a value of 0.86 g/cm^3 for para-hydrogen.

The target thickness and its respective error is important to calculate the cross section and the associated uncertainties. The thickness is calculated by comparing the ^{14}O beam momentum position for the target runs with the empty target runs. The material budget after the target is for both the same and listed in Table 2.3. For the energy loss calculation in the SHT the program *LISE++* is used. An energy loss function is created, which is shown in Fig. 3.29. The function returns the momentum of a particle which hits the target with an momentum of 6050 MeV/c and passes through a certain distance.

The maximum of the momentum distribution of are determined by fitting a gaussian to the peak for the runs with target and without target. Fig. 3.30 shows the momentum distributions for each run of the experiment. Here, run 527 - 551 are the target runs and 561 - 564 and 567 - 574 the empty target runs. An overview of each peak position and the time for each run is given in Appendix B. In the figures, one clearly sees that the momentum and width of the distribution is changing during the

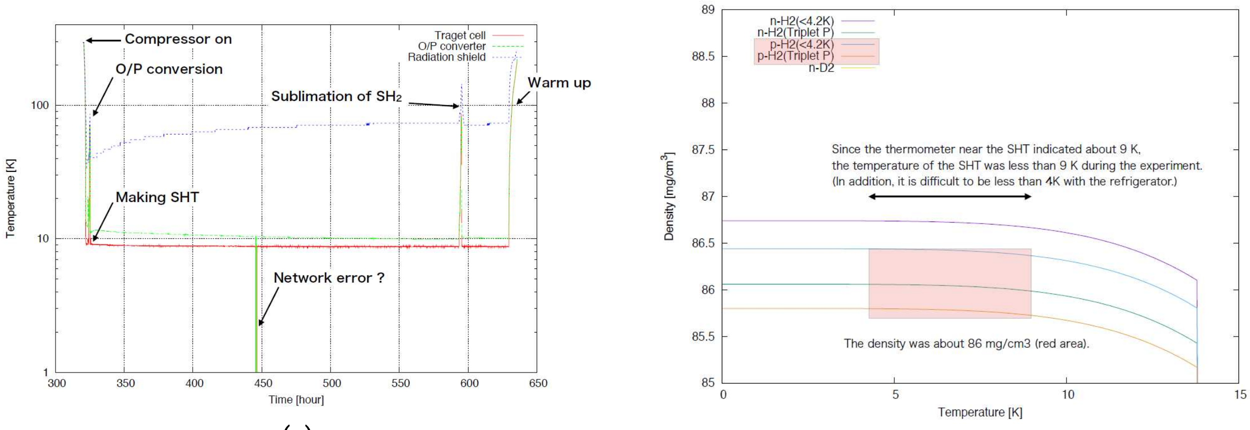

(a)

(b)

Figure 3.28.: (a) Temperature of the target cell during the experiment.(b) Density dependence of para-hydrogen on the the temperature. Courtesy Y. Matsuda.

run. This is probably due the change of the thickness of the condensation water found on the target entrance and exit window. The treatment of the water will be elaborated further in Section 3.12. For now it is only important, that the fluctuations have a large impact on the error of the target thickness. Note, one can see that the mean position of the runs 564,567 - 574 is shifting compared to run 561 - 563. It is assumed, that the target chamber is heating up after emptying and so the water starts to evaporate.

Table 3.6 gives an overview of the important parameters for the target thickness calculation. The average momentum peak position and the respective errors are calculated for target and empty target setup with all runs. The target thickness is then determined by using the energy loss function (Fig. 3.29) to be 2.4 mm $\pm$ 0.33 mm. The error is $\sim$14 %, which will be the largest uncertainty for the cross section.

In addition, an error from the scaling of the magnetic field is calculated. For the simulation in Section 3.4 the original field map has 1.5 Tm and is scaled by a factor to the experimental values. However, it is not necessarily that this scaling is linear. Therefore, the simulations are performed again using a 1 % stronger and a 1 % weaker magnetic field. The results for this simulation are also given in Table 3.6. The difference of the target thickness to the original experimental field is 0.05 mm for 1 % and 0.07 mm for -1 %. Thus, the error is significantly smaller than the 14 % uncertainty determined by the momentum change of the beam with and without the SHT target.

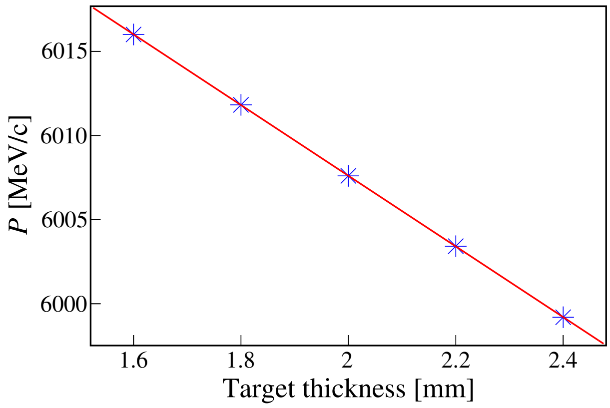

Figure 3.29.: Energy loss of ^{14}O, when passing through the SHT.

Table 3.6.: Average momentum peak position of the experimental data for the experimental magnetic field B_{exp} and for a magnetic field increased and decreased by 1 %. The target thickness is calculated from the momentum difference of the target and background run with the function in Fig. 3.29.

	B_{exp}	B(+1%)	B(-1%)
P with SHT [MeV/c]	6009.24	6062.24	5956.52
ΔP with SHT [MeV/c]	2.79	2.78	2.5
P without SHT [MeV/c]	6059.25	6112.58	6005.92
ΔP without SHT [MeV/c]	6.27	6.46	6.21
Target thickness [mm]	2.4	2.45	2.33
Error target thickness [mm]	0.33	0.34	0.31

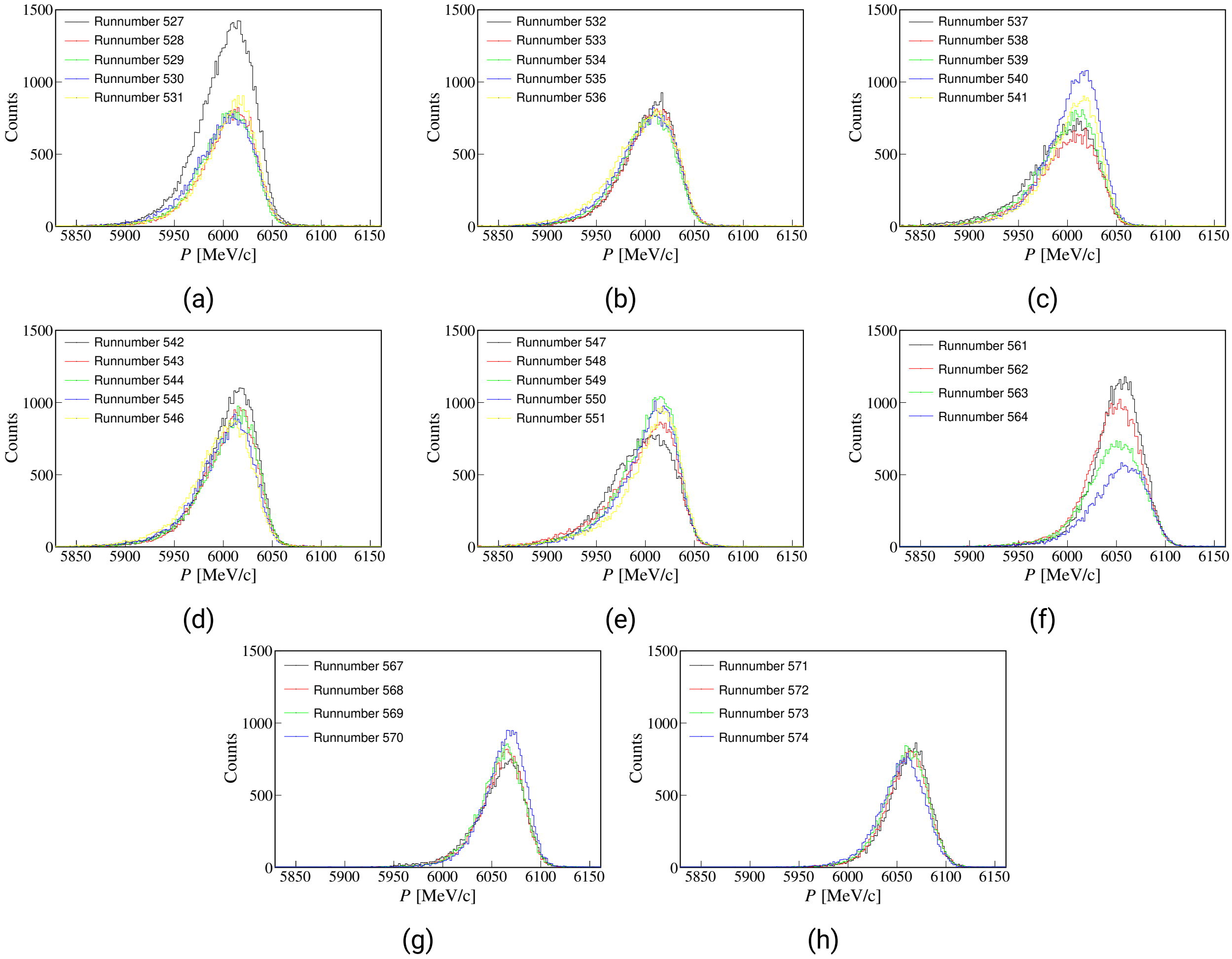

(a) (b) (c)

(d) (e) (f)

(g) (h)

Figure 3.30.: ^{14}O beam momentum distributions calculated from the measurements with the SAMURAI spectrometer. The runs 527 - 551 were with SHT and the runs 561 - 564 and 567 - 574 without. An overview of the estimated peak position and the time of the runs is given in Appendix B Tables B.1 and B.2.

3.10. Acceptance and Reaction Loss Correction

3.10.1. Residue Acceptance

In Fig. 3.32 the experimental P_x and P_y distributions for the unreacted ^{14}O beam and the residues ^{13}O and ^{13}N are shown. The red lines in the figure indicate the acceptance threshold in y-direction. One can clearly see, that the distributions of ^{13}O and ^{13}N are cut, while ^{14}O is only lost slightly. The momentum P_y is limited due to the SAMURAI dipole magnet exit window. It has a height of 800 mm in y-direction and a width of 2800 mm in x-direction. All events outside this window collide with the magnet frame and get stopped. This means, that some of the ^{13}O and ^{13}N events are lost due to this acceptance limitations.

This loss of events needs to be considered in the calculation of the cross sections. Therefore, in this section simulations are performed to estimate the loss of events through the acceptance. Both P_x and P_y acceptance were estimated by simulations.

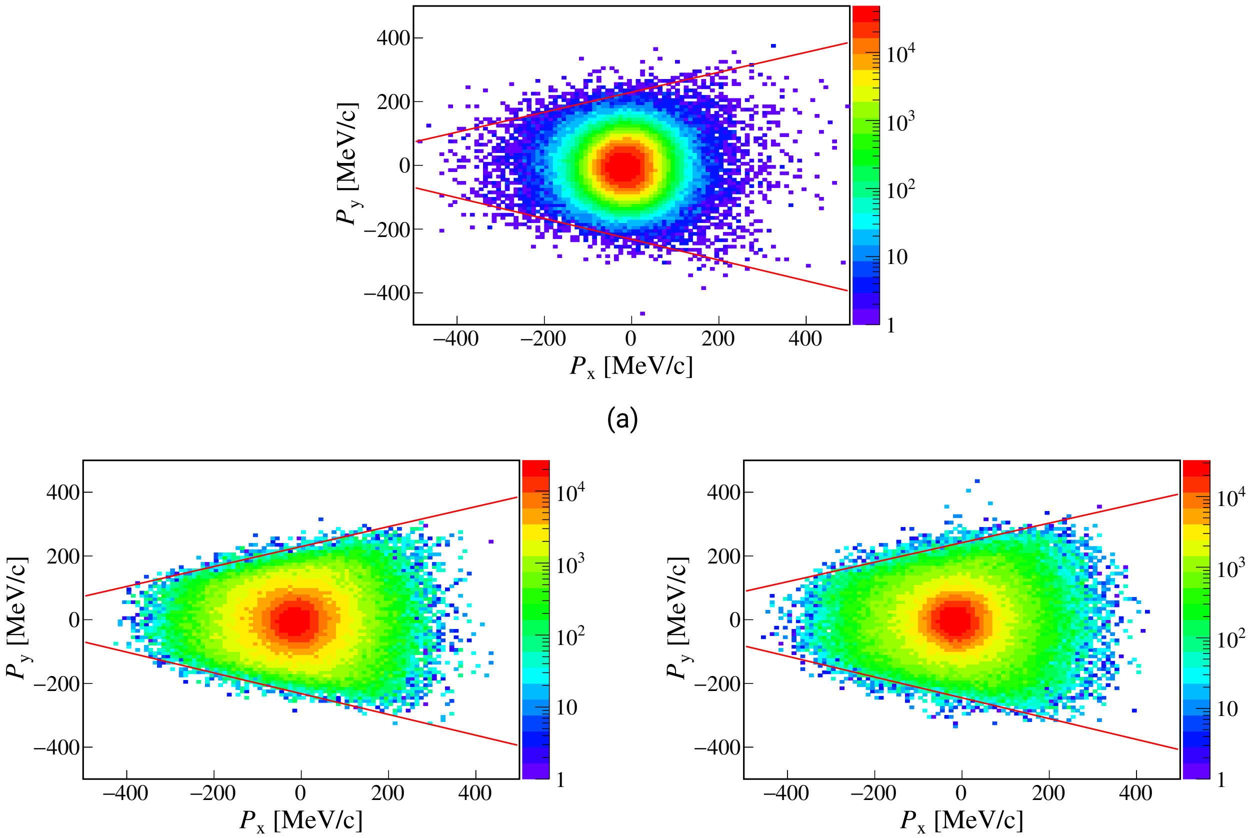

(a)

(b)

(c)

Figure 3.31.: Experimental P_x and P_y distributions for (a) ^{14}O, (b) ^{13}O and (c) ^{13}N. The red lines are there to guide the eyes to indicate the acceptance threshold.

For the simulation the *smsimulator3.5* [66] is used. First, an amount of particles is generated. The trajectories of the particles through the SAMURAI spectrometer are simulated and it is checked, if the particles path through the following components: FDC0, SAMURAI dipole magnet exit window, FDC2 and hodoscope. If a particle does not path through all of them, it is rejected. At the end, the generated events are compared to the accepted ones to estimate the amount of lost events. The generation of the particles and the evaluation of the simulation is different for the P_{x}-acceptance and P_{y}-acceptance and will be described separately in the following.

P_{y}-acceptance

First, the experimental transversal momentum distribution for ^{13}O and ^{13}N are compared in Fig. 3.32. For both nuclei the P_{x} distribution is wider than the P_{y} distribution, which is cut at lower absolute momentum values. The origin of the difference is due to acceptance of the experimental setup as discussed before. Furthermore, the P_{x} distribution has a small offset of $\sim$ -15 MeV/c coming from the angular distribution of the ^{14}O beam. It will be considered in the simulation. In addition, the experimental distribution of ^{13}O and ^{13}N have a different shape, which is also predicted by theory [73]. This leads to a small difference in acceptance for both particles. The transversal momentum shape is an independent topic and is left for future investigation. The focus of this work is on the parallel momentum distribution.

In the ideal case both distributions P_{x} and P_{y} should be the same, because there is no preferred direction, so that it is symmetric relative to the azimuthal angle. This assumption will be used in the following to do the simulation.

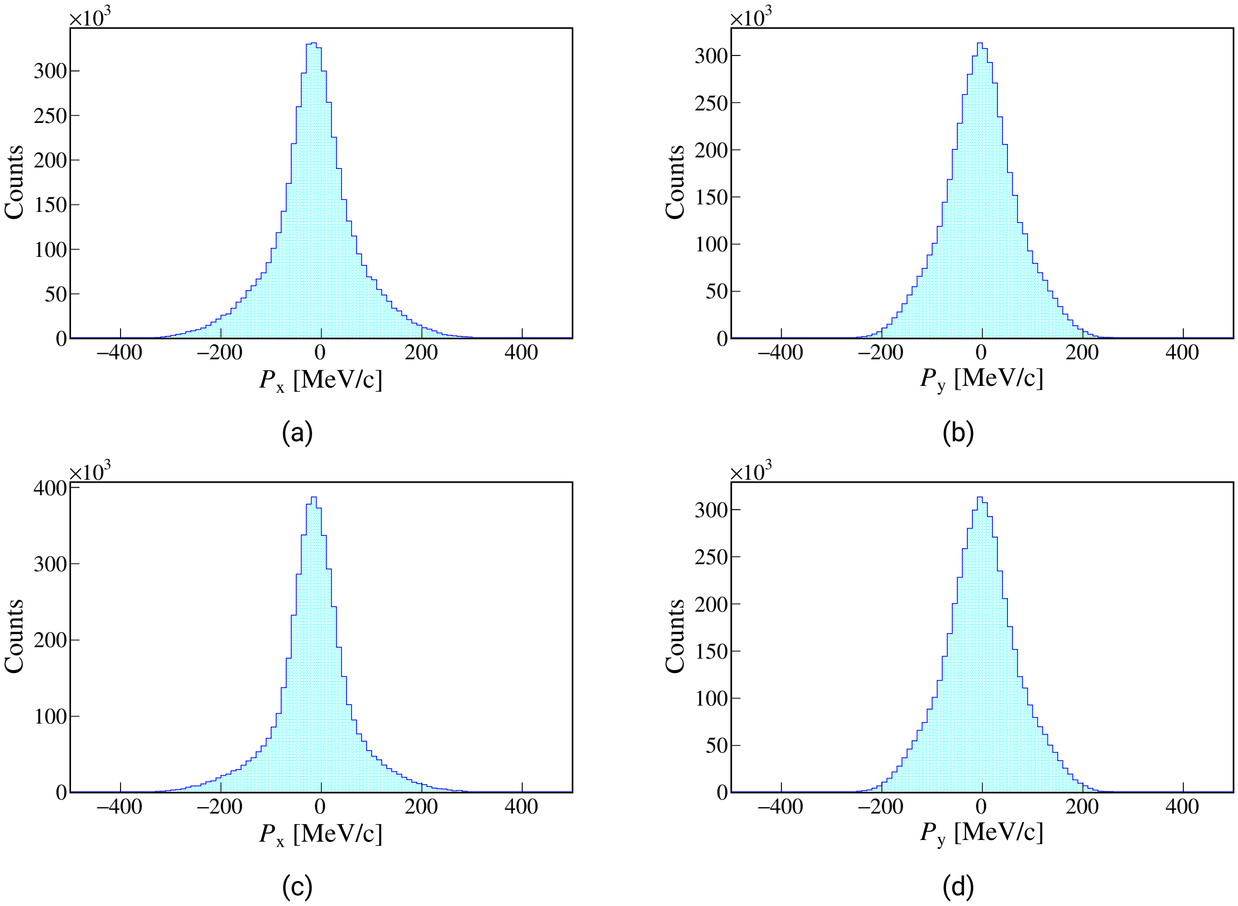

(a)

(b)

(c)

(d)

Figure 3.32.: Experimental transversal momentum distributions for ^{13}O of (a) P_{x} and (b) P_{y} and for ^{13}N of (a) P_{x} and (b) P_{y}.

First, the transversal momentum P_{t} needs to be reconstructed, so that P_{x} and P_{y} can be generated independently. The quantities are related by the following equation:

$$P_\mathrm{t}^2 = P_\mathrm{x}^2 + P_\mathrm{y}^2 \tag{3.17}$$

Due to the acceptance loss of P_y the experimental distribution of P_t is also incomplete. Therefore, it is necessary to make some assumptions for the reconstruction of P_t. It is assumed that for P_y around 0, there is no acceptance loss. To meet this condition only experimental events with $P_\mathrm{y} \leq 20$ are selected. With this approximation Eq. (3.17) can be simplified to:

$$P_\mathrm{t} = |P_\mathrm{x}| \tag{3.18}$$

With Eq. (3.18) it is possible to reconstruct P_t with the experimental distribution of P_x, because we have no acceptance loss of P_x. The distributions for the simulation are then generated using P_t and a uniform distributed azimuthal angle θ with the following equations:

$$P_\mathrm{x}^\mathrm{sim} = P_\mathrm{t} \cdot \cos(\theta) \tag{3.19}$$

$$P_\mathrm{y}^\mathrm{sim} = P_\mathrm{t} \cdot \sin(\theta) + g(\mu = 0, \sigma) \tag{3.20}$$

Here, $g(\mu = 0, \sigma)$ is a correction gaussian function, which is necessary, because of the angular distribution of the ^{14}O beam. The distribution for the beam is shown in Fig. 3.33, from which σ = 27 MeV/c is calculated. In addition, due to an offset in the P_x distribution, a constant offset of 13.9 MeV/c for ^{13}O and 15.4 MeV/c for ^{13}N is added to P_x to shift it close to 0 for the creation of the correct P_t distribution. After the generation P_x^sim it is shifted by -13.9 MeV/c and -15.4 MeV/c to match the experimental P_x distribution better. The comparison between the experimental and simulated P_x distributions for ^{13}O and ^{13}N are given in Fig. 3.34. The simulation reproduces the experimental data very well and will be used as simulation input for P_x and P_y to estimate the acceptance.

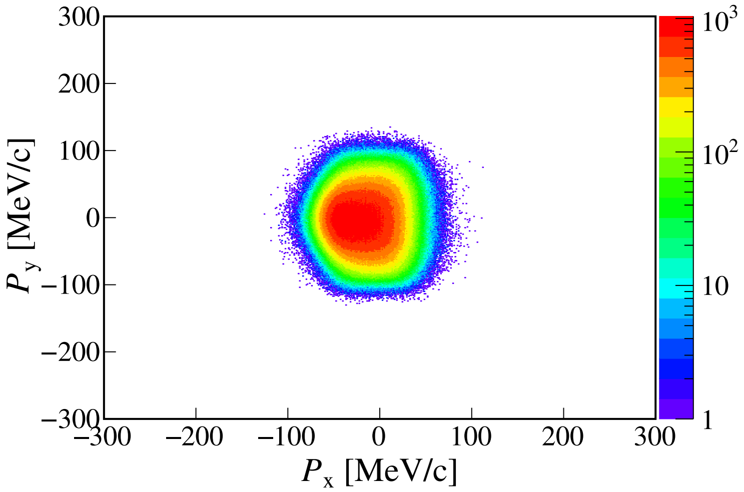

Figure 3.33.: Experimental P_x and P_y distributions of ^{14}O.

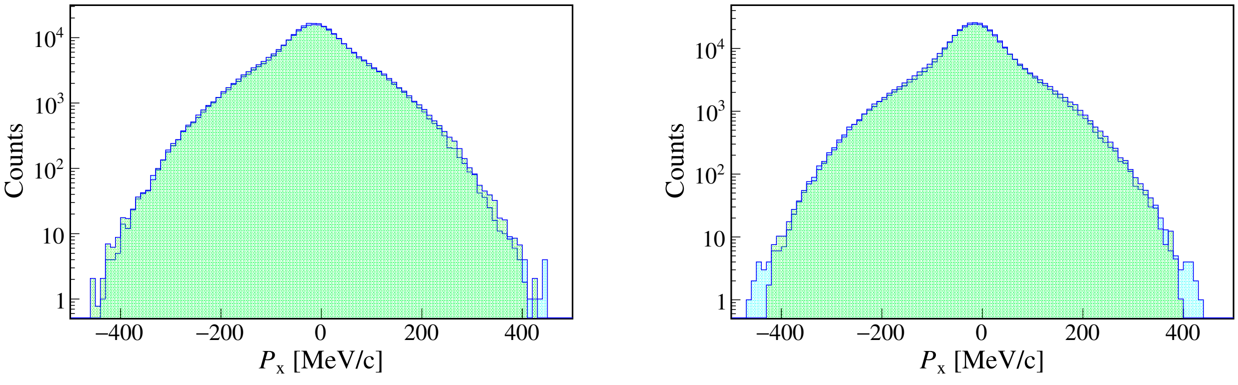

(a)

(b)

Figure 3.34.: Comparison of the experimental distribution (blue) with the simulated distribution (green) for (a) ^{13}O and (b) ^{13}N. The simulated distribution is scaled to have the same area as the experimental distribution. The y-axis is put on log scale, to compare the tails better.

The simulated results are given in Fig. 3.35. The input distributions have a spherical shape, since no direction is preferred. The acceptance distributions are cut due to the P_y acceptance loss. The results match the shape of the experimental distribution in Fig. 3.31, which proves the consistency of the simulation. Therefore, the experimental acceptance loss is extracted by calculating the ratio of generated and accepted events. The acceptance is 94 % for ^{13}O and 96 % for ^{13}N. The cross sections are corrected accordingly.

Table 3.7.: Input for the acceptance simulation.

	P_y-acceptance	P_x-acceptance
Events	1,000,000	1,000,000
P_x distribution	P_x experimental	Uniform
P_y distribution	P_x experimental	$P_y = 0$

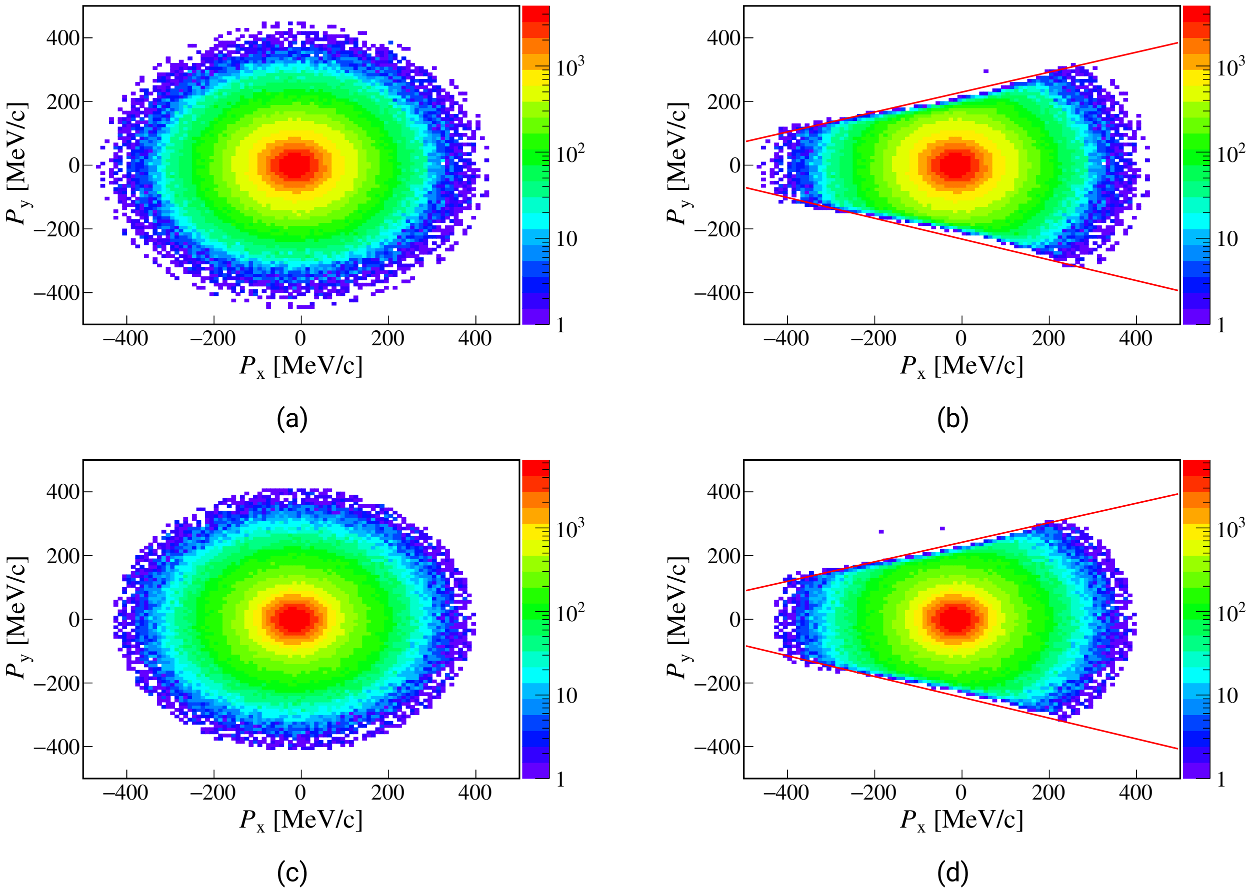

(a)

(b)

(c)

(d)

Figure 3.35.: P_y against P_x simulation input for (a) ^{13}O and (b) ^{13}N. P_y against P_x accepted events for (c) ^{13}O and (d) ^{13}N. The red lines are there to guide the eyes and indicate the acceptance threshold. They are the same as in Fig. 3.31.

P_x-acceptance

For the P_x-acceptance the conditions for the generation of events are summarized in Table 3.7, too. One million events are generated with P_x between 500 MeV/c and -500 MeV/c and $P_\mathrm{y} = 0$ MeV/c, so that only the x-acceptance is evaluated and that there is no impact from the P_y-acceptance. The results from the simulation are given in Fig. 3.36. The left figures show the generated and accepted momentum distributions for ^{13}O and ^{13}N. On the right-hand side the acceptance distributions are shown. The result of the simulation is, that particles are fully accepted between 400 MeV/c and -400 MeV/c. From the comparison with Fig. 3.35 one can conclude, that the x-acceptance is close to 100 %. Only a negligible amount of events has a larger absolute momentum beyond 400 MeV/c.

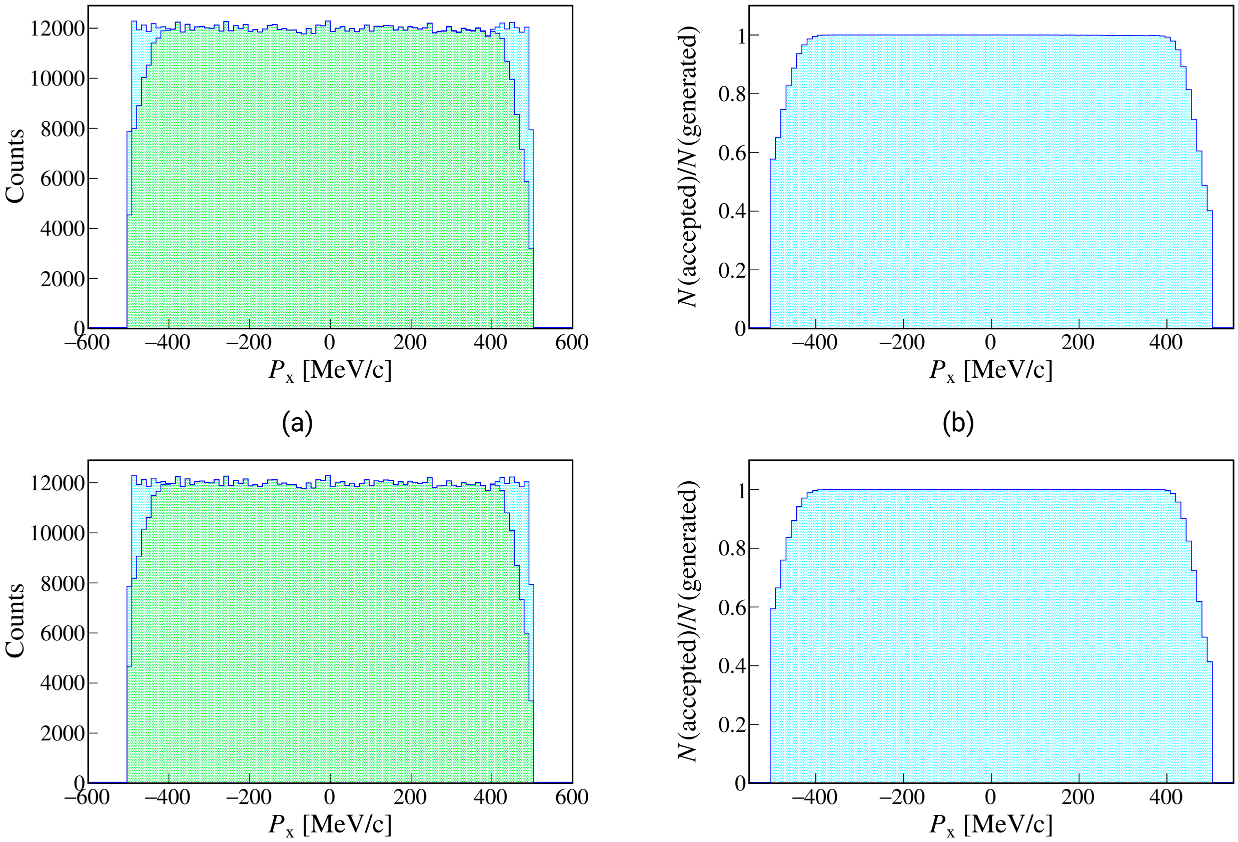

(a)

(b)

(c)

(d)

Figure 3.36.: Input P_x distribution (blue) and accepted P_x distribution (green) for (a) ^{13}O and (c) ^{13}N. Acceptance distribution of P_x for (b) ^{13}O and (d) ^{13}N. Between -400 MeV/c and 400 MeV/c the acceptance is close to 100 %.

3.10.2. Reaction Loss in the Beamline Materials and Hodoscope

The beam and the fragments pass through different materials (see Table 2.3) and the hodoscope after the reaction with the target. Reactions of the particles with the material can occur, which influences the extraction of the cross section. First, the reaction loss from the material between the target and the SAMURAI dipole magnet is evaluated. An estimation of the losses in the hodoscope follow.

Reaction Loss in the Beam-Line Materials

The reaction losses from the downstream SBT1 beam line materials can be estimated by comparing the number of beam events before the target and the number of beam events after the target. When a particle did react in the beam line material, either it will not be accepted by the SAMURAI spectrometer and the event is ”lost” or a fragment is produced, which will not appear as ^{14}O on the PID plot. Fig. 3.37 shows the PID of the ^{14}O beam generated with the *beam trigger*. ^{14}O is selected within the black lines. There is the additional possibility that a detector did not measure an event and the particle does not appear on the PID. Thus, the selection is not fully ”pure”, because it also contains the detector efficiencies, which were already discussed earlier. It is difficult to disentangle, which events are lost through the detector efficiency or through a nuclear reaction along the beamline material. Furthermore, the losses from the hodoscope charge selection are included here for convenience. They could be disentangled with 0.6 % calculated earlier. The number of events are listed in 3.8. Thus, the reaction loss of ^{14}O due to beam line materials is $\sim$6.2(5) % and $\sim$5.9(5) % for runs with and without SHT, respectively. With the assumption that the reaction loss is similar, the same numbers are applied for ^{13}O and ^{13}N.

Table 3.8.: Estimation of losses due to beam line material and detector efficiency.

	Events with SHT	Events without SHT
Unreacted beam events before the target	4,384,961	1,570,291
Unreacted beam events after the target with the selection in this section	4,113,959	1,477,186
Reaction, detector efficiency and hodoscope charge selection loss [%]	6.2(5)	5.9(5)

Reaction Loss in the Hodoscope

In a second estimation, the reaction losses of the particles in the hodoscope is considered. When the particles hit the hodoscope it is possible, that a nuclear reactions occurs, which leads to tails in the energy deposit. For ^{14}O, the number of particles can be straightforward selected with the *beam trigger*. This selection is very difficult, because the tails overlap with other isotopes. Therefore, simulations using the INCL cascade model [74] have been performed to estimate the reaction loss of ^{13}O and ^{13}N in the hodoscope. For benchmarking the simulation, the experimental reaction loss of the ^{14}O beam in the hodoscope is compared to that of the simulation. The experimental reaction loss of ^{14}O in the hodoscope is given in Fig. 3.38. Here, ^{14}O is selected in a 3σ range. The excluded tail corresponds to around 7(1) % of the total amount of ^{14}O striking the hodoscope. The simulation result in 6 - 7 % of the particles react in the hodoscope, which confirm our experimental results within the error bars.

The simulation results for ^{13}O and ^{13}N are given in Fig. 3.39. Here, the energy loss in the hodoscope

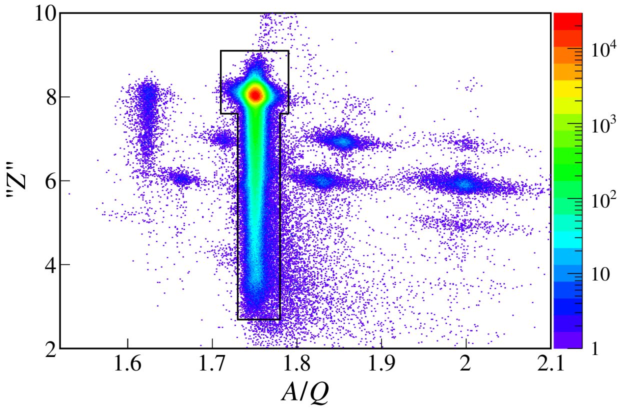

Figure 3.37.: PID with *beam trigger* selection. The selected part is ^{14}O.

ΔE is plotted against the velocity of the particles. The unreacted residues can be clearly identified in the displayed selection. The reacted events amount to a ratio of 5(1) % and will be considered in the calculation of the cross sections.

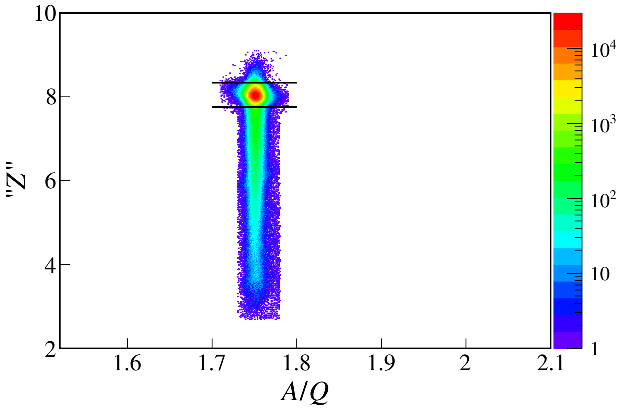

Figure 3.38.: Experimental PID with *beam trigger* selection. ^{14}O in a 3σ environment (black lines) to estimate the tail and thus the amount of particles reacting with hodoscope.

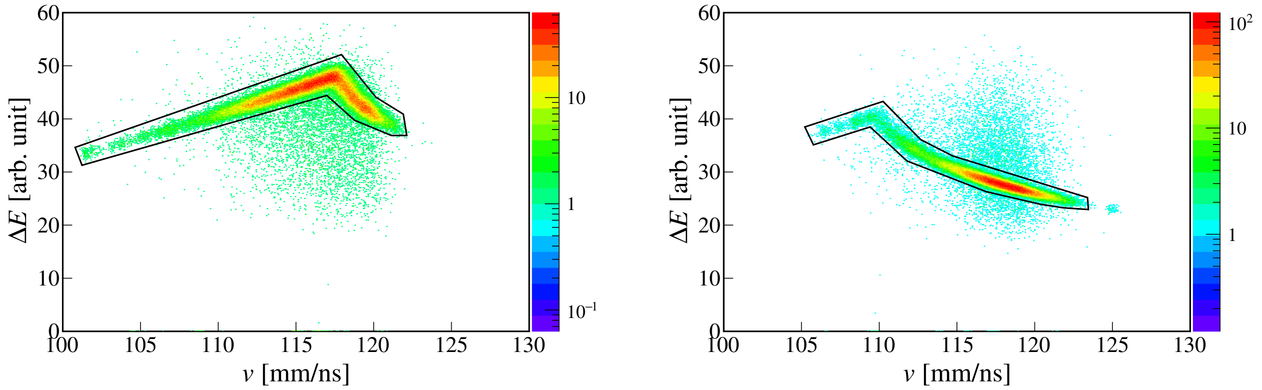

(a)

(b)

Figure 3.39.: Simulated energy loss against velocity for (a) ^{13}O and (b) ^{13}N. The events outside the selections are the ones reacting with the hodoscope. Courtesy Y. Sun.

3.11. Cross Sections

The cross section is calculated with the selection and the target thickness from the previous chapters. For this, Eq. (3.21) is used. Here, N_{target} is the number of residues from the target runs, N_{empty} is the number of residues from the empty target runs, α is the number of beam events during the target runs divided by the number of beam events during the empty target runs, N_{beam} is the number of unreacted beam particles and d is the thickness of the target. f_{1-7} are the different correction factors. An overview is for the factors is given in Table 3.9. The resulting cross sections with errors are given in Table 3.10. The experimental cross section will be interpreted and compared to theory in Section 4.4.

$$\sigma = \frac{N_{\text{target}}(^{13}\text{O}/^{13}\text{N}) \cdot \frac{1}{f_5} - \alpha \cdot N_{\text{empty}}(^{13}\text{O}/^{13}\text{N}) \cdot \frac{1}{f_6}}{N_{\text{beam}} \cdot d} \cdot \frac{f_1}{f_2} \cdot \frac{1}{f_{3/4}} \cdot \frac{1}{f_7} \tag{3.21}$$

Table 3.9.: Correction factors for the calculation of the cross sections.

Factor	Associated correction	Correction value
f_1	DAQ lifetime *reaction trigger*	Tables A.1, A.2, A.3
f_2	DAQ lifetime *beam trigger*	Tables A.1, A.2, A.3
f_3	Acceptance losses ^{13}O	0.94(1)
f_4	Acceptance losses ^{13}N	0.96(1)
f_5	Reaction losses beamline, detector efficiencies and hodoscope charge selection with SHT	0.938(5)
f_6	Reaction losses beam line, detector efficiencies and hodoscope charge selection without SHT	0.941(5)
f_7	Reaction losses hodoscope	0.95(1)

Table 3.10.: Cross sections with respective errors.

	^{13}O	^{13}N
Cross section [mb]	16.8(24)	10.7(16)
Statistical error [mb]	0.11	0.14
Selection error [mb]	0.16	0.23
Systematic error [mb]	2.39	1.56

Target uniformity

The target is not solid at room temperature. It needs to be build by a liquefaction and solidification process at 4 K in mylar cell, which is placed in a vacuum chamber. Therefore, it is possible that the hydrogen is not distributed homogeneously and due to the flexibility of the mylar cell the target can become non uniform. In fact, it is often the case that the target is swollen in the center and decreases in thickness to the side.

The target uniformity is checked by limiting the target radius and calculate the cross sections with the events counted in the limited areas. The radii and the resulting cross sections are listed in Table 3.11. The calculated cross sections also indicate, that our target was thicker in the middle with a maximum thickness of approximately 2.76 mm and thinner on the outside with a minimal thickness of 2.01 mm. This is in agreement with the expectation. In discussion with the solid hydrogen target expert it was pointed out, that a target with a thickness of 2 mm can have an uncertainty of ± 0.15 mm. The tendency for the targets is to be larger and swollen. It is usually not thinner [75].

Table 3.11.: Change of the cross section depending on the target radius.

Radius [mm]	$\sigma_{\text{Exp}}(^{13}\text{O})$ [mb]	$\sigma_{\text{Exp}}(^{13}\text{N})$ [mb]
0 - 15	16.8	10.7
0 - 2.5	19.3	12.2
2.5 - 5	17.4	11.3
5 - 7.5	16.9	10.6
7.5 - 10	16.3	10.3
10 - 12.5	15.8	9.8
12.5 - 15	14.0	9.6

3.12. Thickness Estimation of the Background Water on the Target Windows

In contrast to the BigRIPS ^{14}O momentum distribution the SAMURAI momentum distribution of ^{14}O is asymmetric, which is shown in Fig. 3.40. This should not be the case, since no reaction has taken place and the material in the beamline is homogeneous. This unusual behaviour needs to be investigated and resolved, since a goal of the analysis is to extract the momentum distributions of ^{13}N and ^{13}O, which are predicted to be asymmetric by theory. Thus, an asymmetry from beam is not wanted. However, the effect of this asymmetry is small compared to the final momentum distribution of ^{13}N and ^{13}O, which can be seen in Fig. 3.43.

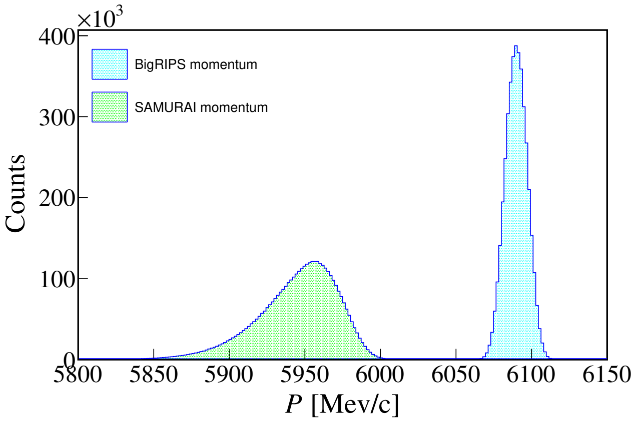

Figure 3.40.: Comparison of BigRIPS and SAMURAI ^{14}O momentum distributions.

The origin of this asymmetric distribution is found to be due to condensation water on the target chamber entrance and exit. A photograph taken during the experiment was already presented before in Fig. 2.6. The target was cooled down to 4 K during the experiment. That is why it was possible for the water to condensate on the windows from the surrounding air. To prove that the asymmetric shape is really due to the water condensation, energy loss simulations have been performed.

For the simulation, the energy loss of the BigRIPS momentum is calculated due to the water and the materials in the target chamber and then compared with the SAMURAI momentum. For the water distribution on one window a half gaussian is taken Fig. 3.41. The σ and the μ value for the water distribution is fluctuating during the experiment and is therefore determined run by run with a χ^2 optimization. For the optimization σ and μ for the water distribution are both varied and then it is applied on the BigRIPS momentum distribution. The new BigRIPS momentum distribution is then compared to the SAMURAI distribution until the minimal χ^2 is found. In addition, there are two different approaches to reproduce the water distribution. In the first one, a water thickness is chosen for the first window and the exact same value is taken for the second window. The change of the water on both windows is negligible, so the total water distribution is half gaussian again. This is referred to as ”static” model. In the second approach, for both windows a different value is chosen. The sum of both distributions is not half gaussian anymore. The interpretation of this model is, that the water on at least one window was changing during a run. This is referred to as ”dynamic” model. The full table with all values and which model is used, is given at the end in Appendix C. The result from the simulation is shown in Fig. 3.42 (a) with a test of quality in (b). The simulation is able to reproduce the SAMURAI momentum in the range from 5880 MeV to 6020 MeV with a deviation of 10 % or less. For events above or below it becomes difficult to reproduce with a small error, because the statistics there is very low and already few events difference can give large error.

After a benchmark of reproducing the experimental beam momentum distribution, the results from this simulation are later used for the convolution of the theoretical calculations to make a proper comparison to the experimental data possible. In addition, the results from the simulation can be used to create a response matrix for a deconvolution of the experimental data.

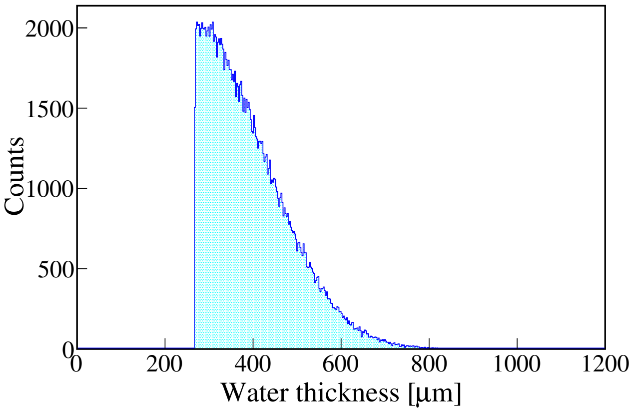

Figure 3.41.: Water distribution used in the simulation.

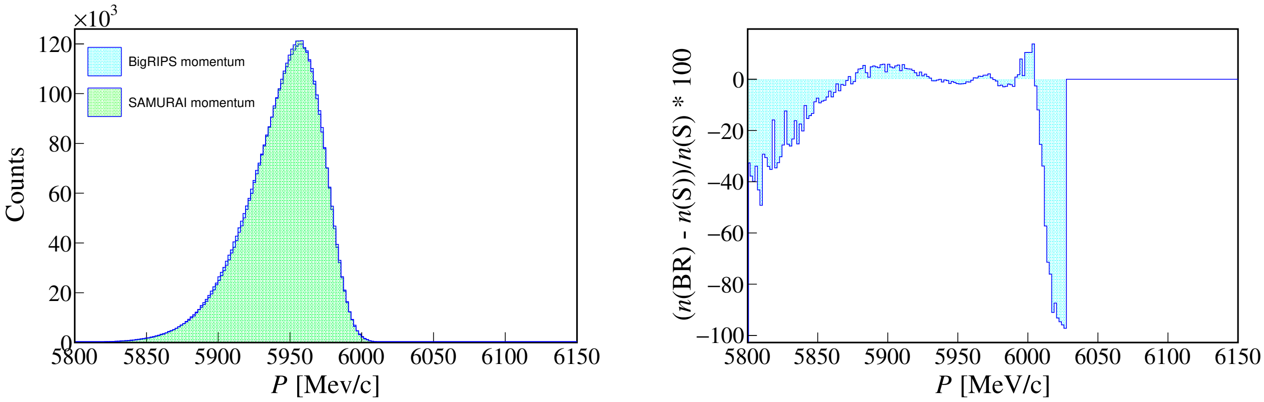

(a)

(b)

Figure 3.42.: (a) BigRIPS momentum after the energy loss simulation compared to the SAMURAI momentum. (b) Test of quality of the simulation by comparing the bin content from the two distributions in (a) and calculate the relative deviation.

3.13. Parallel Momentum Distribution

With the particle identification the residue events for ^{13}O and ^{13}N are selected as for the cross sections. The momentum of the events is then calculated with Eq. (3.22), where $B\rho$ is the magnetic rigidity, which is calculated from the DC coordinates with the multidimensional fit function, m the mass of the residue and c_0 the velocity of light.

$$P = B\rho \cdot m(^{13}\mathrm{O}/^{13}\mathrm{N}) \cdot c_0 \tag{3.22}$$

The momentum distributions for both residues are calculated. Due to target energy loss, naturally there is an offset between target and empty distributions. Therefore, the empty target momentum distribution of ^{13}O is shifted by -50.707 MeV/c and ^{13}N is shifted by -44.176 MeV/c. The values are calculated assuming, that the particles move through half the target (1.2 mm) as ^{14}O and the other half as ^{13}O or ^{13}N. For ^{14}O the particles are striking the target with a mean value of 6050 MeV/c and the residues have a mean energy of 5500 MeV/c. After the shift the empty target distributions are directly subtracted from the target distributions. The y-axis of the distribution is then converted to the unit of a cross section with Eq. 3.21. The final result of the experimental momentum distribution is shown in Fig. 3.43 for proton removal (left) and neutron removal (right). The squares around the experimental points are the systematic errors, which are dominated by the target thickness error as discussed in previous sections. In addition, the unreacted ^{14}O momentum distribution (shifted by -200 MeV/c) is given in the figure for comparison. As one can see, the effect of the experimental response is small in comparison to the width of the residue momentum distribution and so does not have a significant impact on the final results.

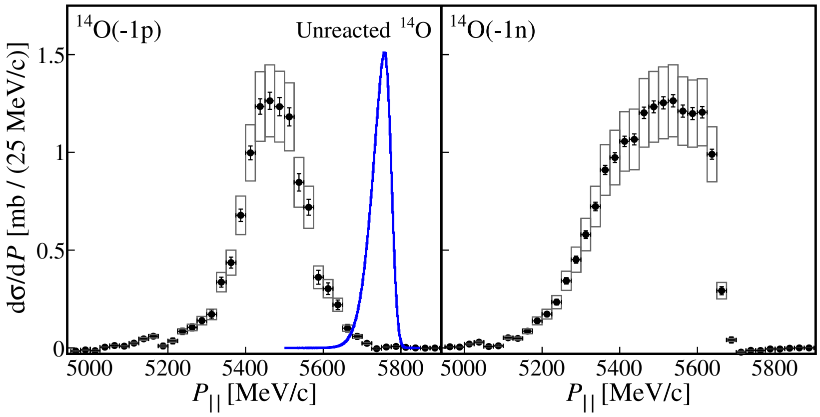

Figure 3.43.: PMD's for one proton (left) and one neutron (right) removal. The rectangles indicate the systematic error. The blue graph is the unreacted ^{14}O shifted by -200 MeV/c to compare the experimental response.

Theory

4. Theory for the Interpretation of the Results

The cross sections and parallel momentum distributions are interpreted and compared to theoretical calculations. Distorted-wave impulse approximation (DWiA) and quantum transfer to the continuum (QTC) calculations are used to describe the knockout reactions. In addition, transfer ^{14}O(p,d) reactions are considered for the ^{13}O residue with the QTC framework and inelastic excitation of ^{14}O for the ^{13}N residue with microscopic DWIA calculations. The theoretical concepts are introduced at the beginning of the section, followed by the presentation of results and the input parameters for this work. The calculations are then compared to the experimental data and interpreted.

4.1. Theoretical Frameworks

In the following, there will be a general introduction on quantum mechanical scattering in Section 4.1.1, which is based on Ref. [6]. The well established approach for the calculation of inelastic scattering is presented in Section 4.1.2 and oriented on Refs. [6, 76]. The distorted-wave impulse approximation (DWIA) is presented in Section 4.1.3 with Refs. [32, 52, 77–80]. Finally, the quantum transfer to the continuum (QTC) is introduced in Section 4.1.4 based on Refs. [22, 81–83]. The major differences of the models will be pointed out. Recent results from DWIA and QTC calculations and the input parameters for the comparison with the experimental data will be given after this introduction.

4.1.1. Quantum Mechanical Scattering

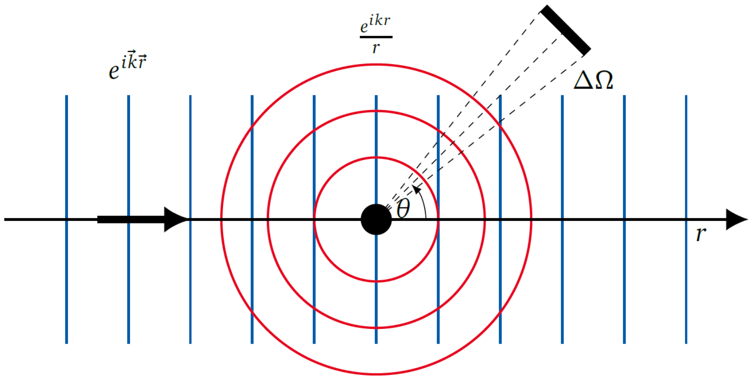

Figure 4.1.: Principle of quantum mechanical scattering. An incoming particle is described as a plane wave and is scattered on a target nucleus. The scattered particle is described by an outgoing spherical wave and measured by a detector, which covers the solid angle $\Delta\Omega$.

The basic idea for quantum mechanical scattering is shown in Fig. 4.1. The incoming particles are described with a plane wave and are approaching a target, where they interact in the case of nuclear interaction with a short-range potential V. The scattered particles leave then as spherical wave. The scattering process is exemplary described with the elastic scattering equation Eq. (4.1). The first term is the approaching plane wave and the second term the outgoing spherical wave. Here, A is a normalization constant, $\vec{r}$ are the relative coordinates, $\vec{k}$ the relative momenta and $f(\Omega) = f(\theta, \phi)$ is the scattering amplitude. The scattering amplitude describes the magnitude of the outgoing spherical wave in dependence of the angles ϕ and θ.

$$\psi_{\vec{k}}(\vec{r}) \to A \left(e^{i\vec{k}\cdot\vec{r}} + f(\Omega)\frac{e^{ikr}}{r} \right) \tag{4.1}$$

The quantum mechanical scattering process itself is described by the Schrödinger equation with a Hamiltonian $H = K + V$. Here, K is the operator for the kinetic energy of the approaching particle and V the short-ranged potential, which conveys the interaction between the particle and the target. The equation for a free particle is then Eq. (4.2) and for a particle interacting with the potential V it is Eq. (4.3). Here, $E_k = \hbar^2 k^2/2\mu$ are the energy eigenstates with μ being the reduced mass and ϕ_k the plane wave eigenfunctions of K, which solve the free particle Schrödinger equation.

$$(E_k - K)|\phi_k\rangle = 0 \tag{4.2}$$

$$(E_k - K)|\psi_k\rangle = V|\psi_k\rangle \tag{4.3}$$

From Eq. (4.2) and Eq. (4.3) the *Lippman-Schwinger equation* Eq. (4.4) can be derived. The solution of the Lippman-Schwinger equation is possible with the Green's function $G(E_k)$ in Eq. (4.5). The addition of $i\epsilon$ avoids possible singularities and defines where the solution corresponds to outgoing or incoming waves. Details on the derivation and calculation can be found in various lecture books such as Ref. [6].

$$|\psi_{\vec{k}}\rangle = |\phi_{\vec{k}}\rangle + G(E_k)V|\psi_{\vec{k}}\rangle \tag{4.4}$$

$$G^{(\pm)}(E_k) = \lim_{\epsilon\to\infty} \left(\frac{1}{E_k - H \pm i\epsilon} \right) \quad . \tag{4.5}$$

The approach of the Green's function and its solution generates two wave states $\psi_{\vec{k}}^{(\pm)}$:

$$\left[\psi_{\vec{k}}^{(\pm)}(\vec{r})\right]_{|\vec{r}|\to\infty} \to \frac{1}{(2\pi)^{3/2}} \left[e^{i\vec{k}\cdot\vec{r}} + \frac{e^{\pm ikr}}{r} \left(-2\pi^2 \left(\frac{2\mu}{\hbar^2}\right) \langle \phi_{\pm k'}|V|\psi_{\vec{k}}^{(\pm)}\rangle \right) \right] \quad . \tag{4.6}$$

$\psi_{\vec{k}}^{(-)}$ describes an incoming spherical wave, which is not a realistic solution for the scattering problem. $\psi_{\vec{k}}^{(+)}$ behaves asymptotically as an incident plane wave and an outgoing spherical wave. The comparison with the phenomenological Eq. (4.1) gives $A = (2\pi)^{-3/2}$ as normalization constant and for the scattering amplitude

$$f(\theta) = -2\pi^2 \left(\frac{2\mu}{\hbar^2}\right) \langle \phi_{k'} | V | \psi_k^{(+)} \rangle \quad . \tag{4.7}$$

The previous equation indicates, that all the scattering information is contained in the matrix elements of the potential. Therefore, it is convenient to define the transition matrix $T_{\vec{k}',\vec{k}}$, which is defined as

$$T_{\vec{k}',\vec{k}} = \langle \phi_{\vec{k}'} | T | \phi_{\vec{k}} \rangle = \langle \phi_{\vec{k}'} | V | \psi_{\vec{k}}^{(+)} \rangle \quad . \tag{4.8}$$

Thus, the relation to the scattering amplitude is

$$f(\theta) = -2\pi^2 \left(\frac{2\mu}{\hbar^2}\right) T_{\vec{k}',\vec{k}} \quad . \tag{4.9}$$

The T-matrix describes the scattering process and includes all the structure and dynamics information. The cross section can then be calculated with the transition amplitude (T-matrix) by the relation

$$\frac{\mathrm{d}\sigma}{\mathrm{d}\Omega} = |f(\vec{k},\vec{k}')|^2 \quad . \tag{4.10}$$

For the description of nucleon removal reactions, the scattering matrix (S-matrix) is usually used. Its definition is given in Eq. (4.11). The square of the absolute value of the S-matrix gives the probability, that a given initial state reaches a certain final state after the scattering process. Thus, it relates physical states and the matrix elements are only defined for initial and final states having the same energy $E_i = E_f$. The S-matrix is by definition related to the T-matrix with Eq. (4.12).

$$S_{\vec{k}',\vec{k}} = \langle \phi_{\vec{k}'} | S | \phi_{\vec{k}} \rangle \tag{4.11}$$

$$S_{\vec{k}',\vec{k}} = \delta(k - k') - 2\pi i \delta(E_k - E_{k'}) T_{\vec{k}',\vec{k}} \tag{4.12}$$

4.1.2. Inelastic Scattering

For a weak potential V one can replace $\psi_k^{(+)}$ with the plane wave ϕ_k in Eq. (4.7). This approximation is used for elastic scattering and inelastic scattering and is called the *Plane Wave Born Approximation* (PWBA). The substitution leads to the following expression

$$f(\theta) = -2\pi^2 \left(\frac{2\mu}{\hbar^2}\right) \langle \phi_{k'} | V | \phi_k \rangle = -\frac{\mu}{2\pi\hbar^2} \int \mathrm{d}^3 r e^{-i\vec{q}\cdot\vec{r}} V(r) \tag{4.13}$$
$$\text{with} \quad \vec{q} = \vec{k}' - \vec{k} \quad .$$

The PWBA is a good approximation for some cases. However, the assumption that the incoming waves are plane waves is no longer satisfied in the vicinity of the nuclear potential. Therefore, the *distorted wave Born approximation* (DWBA) is applied, which replaces the plane waves with distorted waves $\chi_{\vec{k}}$.

For the DWBA the potential is split into two components:

$$V = V_0 + U \tag{4.14}$$

Here, V_0 is the potential, which describes the interaction for the elastic scattering, and U describes the inelastic excitation process. It is assumed that the potential U for the excitation is weak. It is now possible to apply the same ansatz as in the previous section, where the Hamiltonian has been split into $H = K + V$. The previous calculated states $|\phi_{\vec{k}}\rangle$ and $|\psi_{\vec{k}}^{(\pm)}\rangle$ can be related by the waves $|\chi_{\vec{k}}^{(\pm)}\rangle$, distorted by the potential V_0. The Schrödinger equation is then

$$(E - H_0)|\chi_{\vec{k}}^{(\pm)}\rangle = 0 \quad \text{with} \quad H_0 = K + V_0 \ .$$

Again similar to the previous section, the Lippman-Schwinger equations Eq. (4.15) and Eq. (4.17) can be derived and solved with the Green's functions Eq. (4.16) and Eq. (4.18).

$$|\chi_{\vec{k}}^{(\pm)}\rangle = \left[1 + G^{(\pm)}(E_k)V_0\right] |\phi_{\vec{k}}\rangle \tag{4.15}$$

$$G^{(\pm)}(E) = \frac{1}{E - H_0 \pm i\epsilon} \tag{4.16}$$

$$|\psi_{\vec{k}}^{(\pm)}\rangle = \left[1 + \mathcal{G}^{(\pm)}(E_k)U\right] |\chi_{\vec{k}}\rangle \tag{4.17}$$

$$\mathcal{G}^{(\pm)}(E) = \frac{1}{E - [K + V_0 + U] \pm i\epsilon} \tag{4.18}$$

From the previous equations the transition matrix for inelastic scattering can be derived as

$$T_{\vec{k}',\vec{k}} = \langle\phi_{\vec{k}'}|V_0|\chi_{\vec{k}}^{(+)}\rangle + \langle\chi_{\vec{k}'}^{(-)}|U|\psi_{\vec{k}}^{(+)}\rangle \ . \tag{4.19}$$

Because V_0 cannot couple elastic to inelastic scattering, the first term becomes 0 and the inelastic transition matrix can then be written as

$$T^{\text{DWBA}}_{\vec{k}',\vec{k},\text{inelastic}} = \langle\chi_{\vec{k}'}^{(-)}|V_0|\chi_{\vec{k}}^{(+)}\rangle \ . \tag{4.20}$$

The coordinate form of the inelastic part for the reaction $A(a,b)B$ is given as Eq. (4.21). $\chi_\alpha^{(+)}$ and $\chi_\beta^{(-)}$ are the distorted waves in the initial channel α and final channel β. The matrix element corresponds to the integral of the potential U over the internal coordinates of the projectile and target.

$$f^{\text{inel}}_{\text{DWBA}}(\theta) = -2\pi\left(\frac{2\mu}{\hbar^2}\right)\int \chi_\beta^{(-)}(\vec{k}_\beta, \vec{r}_\beta)\langle b, B|U|a, A\rangle\chi_\alpha^{(+)}(\vec{k}_\alpha, \vec{r}_\alpha)\mathrm{d}^3r_\alpha\mathrm{d}^3r_\beta \tag{4.21}$$

4.1.3. Distorted-Wave Impulse Approximation

In the following, the theoretical framework of the distorted-wave impulse approximation (DWIA) will be briefly outlined. The DWIA will be used later in this thesis for the interpretation of the experimental data. The first step for the description of nucleon removal reactions is the introduction of an *optical potential*. The term optical is related to the diffraction of light, where regular minima and maxima intensity patterns appear. The potential $V = V_0 + iW$ is split into two components, a real part and an imaginary part. The real part describes the interaction of the scattered nucleons, while the imaginary part describes the loss due to absorption into other reaction channels. Similar to the approach for inelastic scattering, a two potential Schrödinger equation needs to be solved. The T-matrix and S-matrix can then be extracted to calculate the quantities of interest.

The DWIA has been constantly developed during the last decades and is based on some assumptions, which are characteristic for the theoretical description of the removal of a nucleon. The first assumption is the *impulse approximation*. It is based on the quasi-free scattering picture, where the nucleon removal process occurs in one step. Only the two interacting nucleons are involved, the target proton and the projectile nucleus. Under the impulse approximation the transition matrix can be written as

$$T_{(p,pN)} = \sqrt{S(lj)}\langle \chi^{(-)}_{\vec{k}'_p} \chi^{(-)}_{\vec{k}_N} | V_{pN} | \chi^{(+)}_{\vec{k}_p} \Psi_{jlm} \rangle \ . \tag{4.22}$$

Here, $\chi^{(-)}_{\vec{k}'_{p,N}}$ are the distorted waves of the outgoing projectile and the target nucleon in the potential field of the residual nucleus $A-1$, $\chi^{(+)}_{\vec{k}_p}$ is the wave of the initial incoming nucleon projectile distorted by the nucleus A and Ψ_{jlm} is the bound state wave function of the target nucleon. V_{pN} is the potential between the two nucleons, and $\sqrt{S(lj)}$ the spectroscopic amplitude for a bound nucleon with the quantum numbers (lj). The coordinate form of Eq. (4.22) after simplifying the equation by calculating some of the integrals is

$$T_{(p,pN)} = \sqrt{S(lj)}\,\tau(\vec{k}'_{pN}, \vec{k}_{pN}; E) \int \mathrm{d}^3\vec{r}_{NB} \times \chi^{(-)*}_{\vec{k}'_p}(\vec{r}_{NB})\chi^{(-)*}_{\vec{k}_N}(\vec{r}_{NB})\chi^{(+)}_{\vec{k}_p}(\alpha\vec{r}_{NB})\Psi(\vec{r}_{NB}) \tag{4.23}$$

Here, $\alpha = (A-1)/A$ and $\tau(\vec{k}'_{pN}, \vec{k}_{pN}; E)$ is the Fourier transform of the pN T-matrix. A zero-range approximation for the V_{pn} interaction has been made for this equation. This T-matrix describes the DWIA scattering process.

One can simplify Eq. (4.23) to the plane wave version Eq. (4.24). It gives a straightforward physical interpretation.

$$T^{(\mathrm{PWIA})}_{(p,pN)} = \sqrt{S(lj)}\,\tau(\vec{k}'_{pN}, \vec{k}_{pN}; E) \int \mathrm{d}^3\vec{r} e^{-i\vec{Q}\cdot\vec{r}}\Psi_{jlm}(\vec{r}) \tag{4.24}$$

$$\text{with} \quad \vec{Q} = \vec{k}'_p + \vec{k}_N - \alpha\vec{k}_p \tag{4.25}$$

Eq. (4.24) reveals, that the momentum distribution of the nucleon inside the nucleus is approximately proportional to the cross section. It is a key feature for (p,pn) and $(p,2p)$ removal reactions. This analytically confirms the phenomenological presentation and evaluation of direct reactions in Section 1.2. It can be a good approach for the physical understanding. However, there are deviations from Eq. (4.24) due to absorption and elastic scattering. This effect needs to be considered by distorted waves.

4.1.4. Quantum Transfer to the Continuum

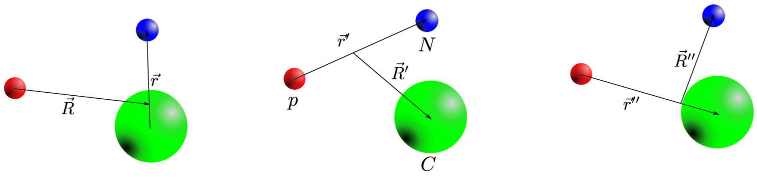

(1) (2) (3)

Figure 4.2.: The three different Jacobi coordinates for the description of a three-body system. Figure from Ref. [22].

The description of transfer reactions is usually done as a three-body system with the Jacobi coordinates. This reduces the complexity of the problem much, since otherwise it needs to be treated as a many-body problem due to the nature of nuclei consisting of many nucleons. The three different sets of Jacobi coordinates are shown in Fig. 4.2. The first set of Jacobi coordinates describes the initial state of a nucleon removal reaction. The position vector $\vec{r}$ gives the relative coordinates between the bound nucleon (blue) and the core (green). The relative position of the projectile (red) to the nucleus is then described by the vector $\vec{R}$. The second set of coordinates is also used for transfer to the continuum calculations. It describes the system after the removal reaction. The removed nucleon and the projectile form a system, where the relative coordinates are given by the vector $\vec{r}'$. Their position to the core C is then described by the vector $\vec{R}'$. The third set of Jacobi coordinates is not used for the description of reactions.

With the introduction of the Jacobi coordinates, the three-body Schrödinger equation for transfer reactions can be expressed as

$$(E^- - K_{r'} - K_{R'} - V_{pN} - U^\dagger_{pC} - U^\dagger_{NC})\Psi^{3b(-)}_f(\vec{r'},\vec{R'}) = 0 \ . \tag{4.26}$$

$E^- = E - i\epsilon$ with E being the total energy of the system, $\vec{r},\vec{R}$ are the relative Jacobi coordinates defined in Fig. 4.2, $K_{r',R'}$ is the kinetic energy of the two center of mass systems defined by r' and R', V_{pN} the nucleon-nucleon interaction and U_{pC} and U_{NC} are effective nucleon-nucleus interactions. The T-matrix for transfer reactions is then

$$T^{3b}_{if}(\alpha) = \langle \Psi^{3b(-)}_f \phi^\alpha_C(\xi_C)|V_{pN} + U_{pC}|\phi_A(\xi_A)e^{i\vec{K}_{pA}\vec{R}}\rangle \ . \tag{4.27}$$

Here, $\phi_A(\xi_A)$ is the ground state wave function of the nucleus A with ξ_A being the internal coordinates, $e^{i\vec{K}_{pA}\vec{R}}$ is the plane wave describing the relative motion of the $p+A$ system, V_{pC} is the potential describing the interaction of the target nucleon with the core, $\Psi^{3b(-)}_f$ is the three-body scattering wave function in the channel f and $\phi^\alpha_C(\xi_C)$ is the core wave function in the state α. The scattering wave consists of a plane wave in the channel f describing the relative motion of the outgoing fragments with the core in state α and incoming spherical waves in all other channels. Eq. (4.27) can be further simplified. First, one can calculate part of the integral by assuming that the potential V_{pN} is independent from the internal coordinates $\xi_{A,C}$. Then one can perform the integral over the internal coordinates of the core, ξ_{AC}, which corresponds to the overlap integral between ϕ_A and ϕ_C, whose result is approximated by $\sqrt{S_{\alpha,l,j}} \times \phi^\alpha_{CA}(\vec{r})$, which is take to be normalized to 1. Also, a distorted wave with an optical potential U_{pA} can be used in the initial channel, resulting in the T-matrix

$$T_{if}^{3b}(\alpha) = \sqrt{S_{\alpha,l,j}}\langle\Psi_f^{3b(-)}|V_{pN} + U_{pC} - U_{pA}|\phi_{CA}^{\alpha}\chi_{pA}^{(+)}\rangle \ . \tag{4.28}$$

$\chi_{pA}^{(+)}$ is the wave function generated from the potential U_{pA}. For U_{pA} usually an optical potential is chosen, which describes the elastic scattering of the $p + A$ system. The remnant term $U_{pC} - U_{pA}$ will then contribute not much to the integral. The transfer process is then dominantly described by the V_{pN} potential. The three-body wave function can be expressed in terms of $p + N$ eigenstates as

$$\Psi_f^{3b(-)}(\vec{r}', \vec{R}') = \sum_{j^\pi} \int \mathrm{d}k \phi^{j\pi}(k, \vec{r}')\chi_{j,\pi}(\vec{K}, \vec{R}') \ . \tag{4.29}$$

Here, $\phi^{j\pi}(k, \vec{r}')$ are the eigenstates of the $p + N$ Hamiltonian using the potential $V_{pN}(\vec{r}')$, $\vec{k}$ is the relative wave number of the $p + N$ pair, $\vec{K}$ is the relative wave number between the residual nucleus C and the $p + N$ pair and $\chi_{j,\pi}(\vec{K}, \vec{R}')$ describes the relative motion of the $p + N$ system in the final state k, j^π with respect to the residual nucleus.

$\chi_{j,\pi}(\vec{K}, \vec{R}')$ cannot be calculated directly, because K is continuous and thus this would give rise to infinite equations. The general approach to solve this issue is to discretize the states. It is a well established procedure, which was introduced first in continuum-discretized coupled-channels (CDCC) calculations. The final $p + N$ states are binned in energy or momentum. Eq. (4.29) is then written as

$$\Phi_f^{3b(-)} \approx \Phi_f^{\mathrm{CDCC}} = \sum_{n,j,\pi} \phi_n^{j,\pi}(k_n, \vec{r}')\chi_{n,j,\pi}(\vec{K}_n, \vec{R}') \ . \tag{4.30}$$

k_n are average values for the discretized $p - N$ energies and $\phi_n^{j,\pi}(k_n, \vec{r}')$ are the bin wave functions. With the known T-matrix the cross section can then be determined. Note, that the presented formulas are derived from non-relativistic calculations. Since many reactions take place at several MeV/nucleon relativistic corrections need to be done. However, since they are not important for the physical interpretation, the details for relativistic calculations will not be presented. They can be found in the literature presented at the start of the section.

4.2. Recent Results for DWIA and QTC

There is only few published data were DWIA and QTC are directly compared to each other. They are presented here, for showcasing the applicability of the two formalisms. In Fig. 4.3 results are given on benchmarking the two formalisms on the nucleon removal reaction ^{15}C(p,pn)^{14}C at 420 MeV/nucleon [80]. A separation energy of $S_n = 1.22$ MeV is assumed for the removed neutron. Fig. 4.3 (a) shows the results of the parallel momentum distribution for DWIA and TC calculations. For the DWIA framework two different potentials have been applied, in which it is either dependent or independent on the incident beam energy. For the energy independent potential, the DWIA parallel momentum distributions show a very good agreement with the TC calculation. The results with energy dependent potential show a slightly lower amplitude. Fig. 4.3 (b) shows the same calculations without a distortion potential. In this case, the waves are no longer distorted and the DWIA reduces to the PWIA. Here again, the shape of PWIA and TC show a very good agreement, after the distorting potentials have been removed in the TC calculations.

Furthermore, the results from an artificial change of the separation energy to 5 and 18 MeV are presented in Ref. [80]. The shapes of the momentum distributions are qualitatively the same to the ones in Fig. 4.3 with the difference of having a smaller amplitude. Still, both theories are in good agreement again. This is an interesting result, since it shows that DWIA and TC predict theoretically the same results for loosely-bound and deeply-bound nucleon removal for high incident energies. Unfortunately, there has been no publication for such a direct comparison of the momentum distributions for lower incident energies around 100 MeV/nucleon.

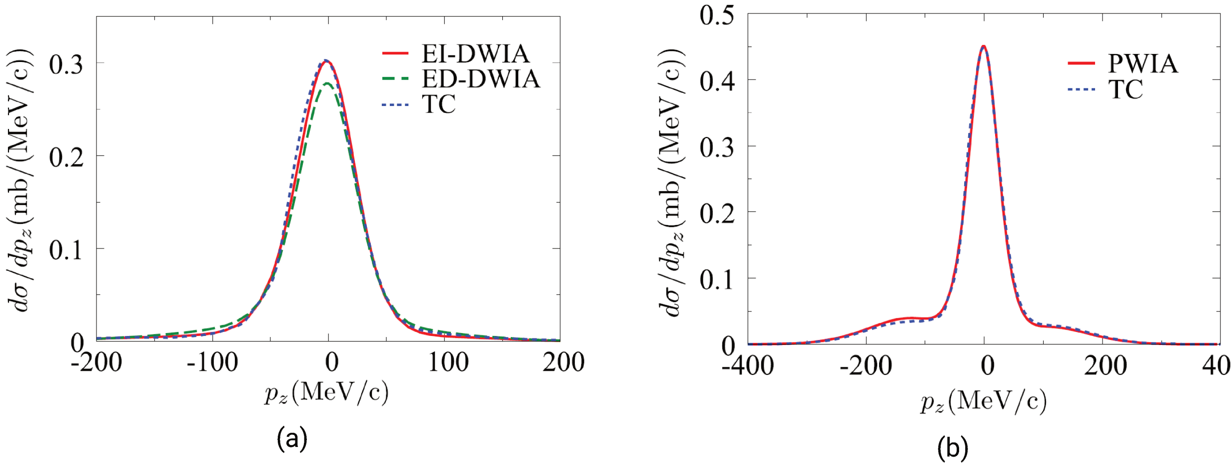

(a)

(b)

Figure 4.3.: (a) Longitudinal momentum distribution of the ^{15}C(p,pn)^{14}C reaction at 420 MeV/nucleon. The struck neutron is assumed to be in a $2s$ orbital with a separation energy of 1.22 MeV. The results are for EI-DWIA (energy-independent potentials), ED-DWIA (energy-dependent potentials) and TC. (b) The same calculations as for (a), but with the distortion potentials switched off. Figures from Ref. [80].

A thorough comparison of the cross section of proton removal from ^{16}O can be found in Ref. [35]. The overall results are shown in Fig. 4.4. Here, the reduction factors R_s are obtained from different reaction mechanisms: (e,e'), (p,$2p$), heavy-ion induced knockout and (d,^{3}He) transfer. The experimental cross sections to calculate the R_s are inclusive. It includes the $1/2^-$ ground state and the $3/2^-$ bound excited states, from which the first one at 6.32 MeV has the strongest spectroscopic strength. The quenching factors are calculated with respect to the IPM limit. Various theoretical formalism are applied for the calculation of the theoretical cross section, depending on how the experimental data was obtained. For (p,$2p$) at 451 MeV/nucleon [46] the DWIA [77], DWIA and QTC are applied. The results are $R_s \sim 0.65$ for eikonal DWIA and $R_s \sim 0.75$ for QTC are very close, while the DWIA exhibits a significantly larger $R_s \sim 1$. The eikonal DWIA results fit well to the results of (e,e') elastic scattering [30, 49], while the QTC results are outside the uncertainty band. Both results are larger than the results from heavy-ion induced knockout and transfer. For details on the calculation on the data and all calculations it is referred to Ref. [35] and references within. Overall, QTC has a good agreement in the calculation of the cross section, while DWIA shows deviation which can stem from a different treatment of relativistic corrections.

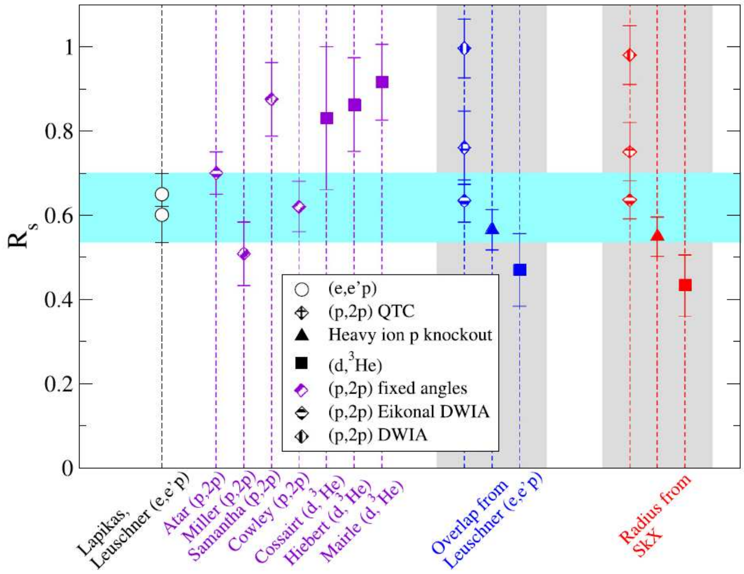

Figure 4.4.: Comparison of the reduction factor R_s for one-proton removal from ^{16}O through different reactions: (e,e') (circles), (p,$2p$)(diamonds), heavy-ion knockout (triangles) and (d,^{3}He) transfer (squares). The R_s are given in purple. The color and the shaded bands indicate the use of the same one-proton overlap. Blue corresponds to overlap with the rms radius form [49] and red to the rms radius from Hartree-Fock calculation using the SkX interaction. Details on calculation can be found in [35] and references within. Figure from Ref. [35].

The trend that the QTC predicts a reduction factor between $\sim 0.7-0.8$ is also presented in [83]. In the various data sets of oxygen and nitrogen isotopes from the R3B campaigns [45–47] are analysed with the QTC framework. The incident energy of the nucleon removal reactions was between 300 and MeV/nucleon. Furthermore, only a small dependence on the isospin is found. In most of the cases, the data was also analysed with DWIA, which predicted a systematically smaller $R_s \sim 0.6 - 0.7$. Finally, the DWIA has been applied on the nucleon removal from different medium mass exotic nuclei with an incident energy of 200-250 MeV/nucleon [84–86]. In each case, the experimental momentum distribution has been successfully reproduced, which emphasizes the reliability of the model.

4.3. Theoretical Input Parameters

For the calculation of the theoretical cross section with Eq. (1.6) reaction and structure inputs are necessary. The spectroscopic factors SFs give the structure information for the removal of a neutron and a proton from ^{14}O. They were calculated from the shell model in the psd-model using the YSOX interaction [87] limited to $5\,\hbar\omega$ using the KSHELL code [88]. The single-particle energy of the $\pi 1s_{1/2}$ orbit was decreased by 0.375 MeV to have a good reproduction of the low-lying energy level structure of ^{14}O. The spectroscopic factors are 1.6 and 3.4 for ^{13}N and ^{13}O, respectively. In addition, shell model calculations with the program OXBASH [89] were performed. It uses the WBT and WBP interaction [90]. The spectroscopic factor results are similar but slightly higher with 1.8 and 3.7.

For the reaction inputs the DWIA and QTC are applied to calculate the single-particle cross sections and momentum distributions. For the DWIA calculations the folding potential with the Melbourne G-matrix interaction is used to determine the distorted waves. This potential can be applied in an energy range from 30 MeV to 150 MeV. The Franey-Love interaction [91] is used to describe the nucleon-nucleon cross section for the transition process. For the non-locality of the optical potential the Perey correction [92] is applied for the bound-state and scattering wave functions. The scattering energy of the emitted nucleons is used to account for the energy dependence of the optical potentials.

For the QTC calculations, the $p+N+{}^{13}$O/^{13}N three-body final state is expressed in a basis of discretized continuum states of the $p+N$ system. The Reid93 was used to describe the interaction [93]. The incident and outgoing channels are distorted by the microscopic JLM potential, which can be applied up to 160 MeV [94]. The G-matrix folding and JLM potential is applied on the experimental differential cross section of $p+{}^{16}$O elastic scattering at 65 MeV [95] as a benchmark. The results are given in Fig. 4.5, which shows that the potentials reproduce the data well. For DWIA and QTC the single-particle wave function of the knocked-out nucleon was obtained by solving the Schrödinger equation using a Woods-Saxon potential with its depth adjusted to give the binding energy of the knocked-out nucleon. Note that recent *ab initio* calculations, such as the self-consistent Green's function theory or no-core shell model, provide a slightly enhanced inner part in the single-particle wave function than the Woods-Saxon potential [96, 97].

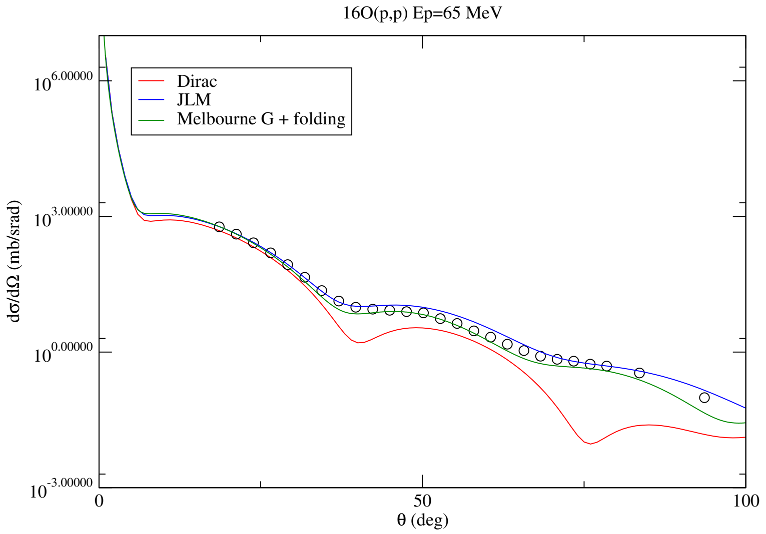

Figure 4.5.: Benchmark of the Dirac, JLM and Melbourne G + folding potentials with ^{16}O(p,p) elastic scattering data. Experimental data from Ref. [95]. Courtesy M. Gomez for the JLM and Dirac potential and K. Yoshida for the Melbourne G + folding potential calculations.

The cross section for the inelastic excitation process have been calculated with the microscopic DWIA reaction model [98]. As structure input the one-body transition (OBTDs) from the above mentioned shell model calculations is applied. The interaction of the transition is again described by the Franey-Love nucleon-nucleon effective interaction. The distorted-waves are generated with the Koning-Delaroche (KD) phenomenological optical potential, which is applicable in an energy region of 1 keV to 200 MeV [99]. The potential have been validated with inelastic scattering of a proton on a ^{12}C target. As can be seen in Fig. 4.6 (a), the potential reproduces well the differential cross section of the 2_1^+ excitation of ^{12}C measured at 120 MeV [100]. The total inelastic cross section sums up to 9(1) mb by considering eight excited states of ^{14}O (0_2^+,0_3^+,2_1^+,2_2^+,0_1^-,1_1^-,2_1^-,3_1^-), which could decay via one proton emission to ^{13}N [101]. The dominant contributions stem from the 2_1^+, 1_1^- and 3_1^- excitations. The cross section of these three states are given in Fig. 4.6 (b). The uncertainty is estimated by performing the calculation with the WBP or WBT interaction for the OBTDs and by using the M3Y nucleon-nucleon interaction, that takes the medium effects into account [102].

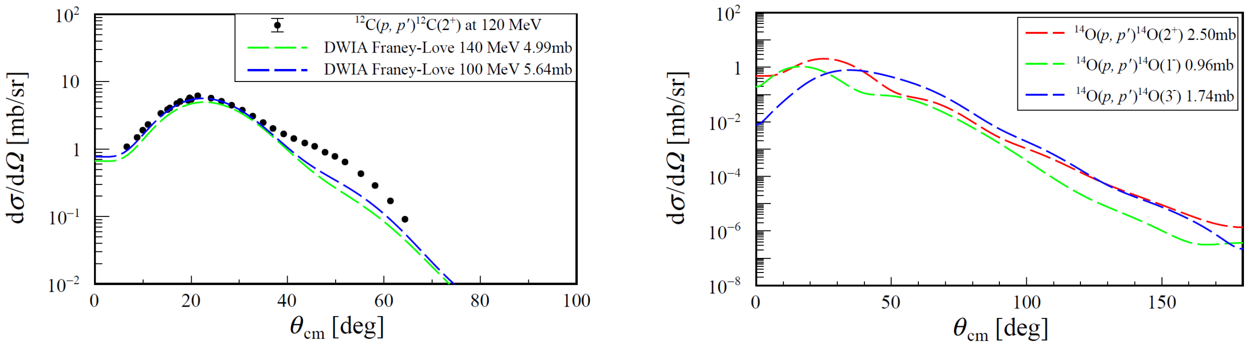

(a)

(b)

Figure 4.6.: (a) Differential cross section for ^{12}C(p,p')^{12}C(2^+). Results with nucleon-nucleon two body interaction at 100 and 140 MeV/nucleon are compared. (b) The differential cross section of ^{14}O(p,p') for the three most dominant states 2_1^+, 1_1^- and 3_1^- . For the calculation the Franey-Love interaction at 100 MeV/nucleon was used. Experimental data from Ref. [100] and inelastic calculations from Ref. [103].

4.4. Summary Theoretical Frameworks and Input

Finally, a table is given to summarize the most important differences and the input for the two theoretical frameworks:

Table 4.1.: Overview of the differences and the common aspects of DWIA and QTC.

	DWIA	QTC
Potential	Folding potential with Melbourne G-matrix interaction	JLM optical potential
Interaction	Transition process described by Franey-Love interaction	N + p + ^{13}O/^{13}N three body final state expressed in a basis of discretized continuum states of the $p+N$
Perey correction	Yes	No
Energy dependence of potential	Yes	No
Sudden approximation	Yes	No
Eikonal approximation	No	No

Results

5. Results and Interpretation

5.1. Overview of the Results

An overview of the experimental cross section results with the calculated theoretical cross-sections is given in Table 5.1. The experimental cross section for one-proton and one-neutron removal from ^{14}O have been determined in the analysis section to be 10.7(16) mb and 16.8(24) mb, and only involve the orbitals of $\pi 0\mathrm{p}_{1/2}$ and $\nu 0\mathrm{p}_{3/2}$, respectively, since both ^{13}N ($J^{\pi}_{\mathrm{g.s.}} = 3/2^{-}$) and ^{13}O ($J^{\pi}_{\mathrm{g.s.}} = 1/2^{-}$) do not exhibit bound excited states. The ratio of the measured inclusive cross sections can be qualitatively understood as consistent with the IPM occupancies: $\sigma(-\nu 0p_{3/2})/\sigma(-\pi 0p_{1/2}) = 1.57 \sim 4/2 = 2$. The experimental and theoretical momentum distributions are shown in Fig. 5.1. The experimental distributions have similar features as the momentum distributions obtained from one-nucleon removal from ^{14}O at 53 MeV/nucleon with a ^{9}Be given in Fig. 1.12 and the theoretical calculations from one-nucleon removal at 100 MeV/nucleon with a proton target in Fig. 1.13. For the removal of the deeply-bound neutron a strong asymmetric distribution is observed, where the high-momentum cut-off stems from energy conservation. The momentum distribution for the loosely-bound proton is close to symmetric. The comparison to the theoretical distributions will be discussed in the following beginning with proton removal and followed by the neutron removal reaction.

Table 5.1.: Experimental and theoretical cross sections of one-nucleon removal from ^{14}O at 94 MeV/nucleon. The theoretical cross sections, except the inelastic excitation, include the center-of-mass correction factor $A/A-1$, with A the mass number of the projectile [104]. The ratio of experimental to theoretical inclusive cross section (R$_s$) is given.

Residue	J^{π}	σ_{exp} [mb]	SF	Theory	$\sigma_{\mathrm{s.p.}}$ [mb]	σ_{th} [mb]	R$_s$
^{13}N$_{\mathrm{g.s.}}$	$1/2^{-}$	10.7(16)	1.6	DWIA	5.2	9	
				Inelastic	-	9	
				Sum		18	0.60(9)
				QTC	7.0	12	
				Inelastic	-	9	
				Sum		21	0.51(8)
^{13}O$_{\mathrm{g.s.}}$	$3/2^{-}$	16.8(24)	3.4	DWIA	6.3	23	
				Transfer	3.0	11	
				Sum		34	0.49(7)
				QTC	13.5	50	0.34(5)

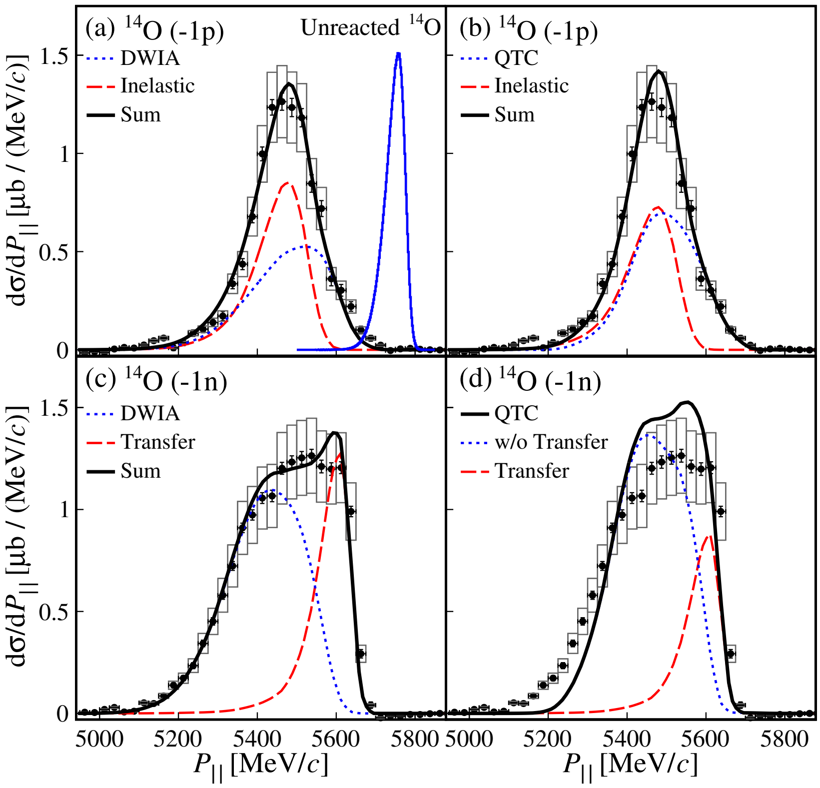

Figure 5.1.: Parallel momentum distributions of ^{13}N (a),(b) and ^{13}O (c),(d), from the one nucleon removal of ^{14}O at 94 MeV/nucleon. The black filled markers show the experimental data, and the grey empty bin the systematic uncertainties. The data are compared to the DWIA and QTC reactions model calculations (dotted lines), with additional contributions from the inelastic excitation for ^{13}N and (p,d) transfer for ^{13}O (dashed lines). The black solid lines show the total theoretical contributions. The blue solid line shows the PMD of the unreacted ^{14}O beam (shifted by - 200 MeV/c) for demonstration of the experimental response. All the theoretical calculations have been convoluted with the experimental PMD response and their integrals have been normalized to the experimental values.

5.2. Results for Proton Removal

The single-particle cross section $\sigma_{\text{s.p.}}$ for ^{14}O(p,2p)^{13}N are 5.2 mb and 7.0 mb from DWIA and QTC calculations, respectively. Furthermore, the proton separation energy is only 4.6 MeV and therefore, inelastic excitation of ^{14}O followed by proton decay to the ^{13}N ground state is additionally considered. The cross-section are summarized in Table 5.1. The theoretical one-proton removal cross section σ_{th} is the sum of the (p,2p) knockout cross section and the inelastic excitation cross section ($\sigma_{\text{inelastic}}$). The knockout cross section is calculated with Eq. (1.6). $A = 14$ in this case and for C^2S the C is usually 1, so that S is the spectroscopic factor. Both channels have a similar contribution for the loosely-bound removal reaction. With the DWIA and QTC the σ_{th} of 18 mb and 21 mb are obtained, which lead to reduction factors of $R_s = 0.60(9)$ and $R_s = 0.51(8)$.

The theoretical momentum distributions of the DWIA and QTC with the inelastic contribution are shown in Fig. 5.1, where they are compared to the experimental distribution of ^{13}N. The amplitude of the theoretical distribution is scaled by the above reduction factors. The PMDs of both the (p,p') and (p,2p) reactions are slightly asymmetric with a low momentum tail. The tail for the inelastic excitation stems mainly from the inelastic scattering of ^{14}O to large angles. The tail for the knockout reaction is due to the attractive potential of the outgoing protons and ^{13}N [52]. In addition, due to kinematic restrictions, the (p,p') PMD peak position is about 50 MeV/c lower than the peak of (p,2p). The final distribution combines the (p,p') and (p,2p) PMDs and is close to symmetric. The experimental data is well reproduced, which confirms the strong inelastic contribution to the loosely-bound proton removal. The small gap around 5200 MeV/c is due to the uncertainty of the target thickness, so that the shift of the empty target distribution has also an uncertainty of ~6 MeV/c. This can lead to a small shift of the bin subtraction, which results in the gap. By not taking the inelastic component into account, the reduction factor for the loosely-bound proton removal will be around unity, which coincides with the R_s from eikonal model based analysis [36, 105, 106]. The inelastic excitations are not explicitly treated in the eikonal model calculations, but are usually assumed in the absorptive optical potentials. It is valuable to assess the validity of this assumption in the light-ion induced one-nucleon removal reactions if the removed nucleon is loosely bound. Note, that only a given number of excited states are used for inelastic scattering. The giant resonance region is not considered, because no data could be found. There could be a contribution to the inelastic process from protons being excited into collective states. If it would be possible to calculate this contribution and add it to the results, the calculated reduction factors would reduce further.

5.3. Results for Neutron Removal

The cross sections for the deeply-bound neutron removal are also summarized in Table 5.1. The single-particle cross section $\sigma_{\text{s.p.}}$ for the reaction ^{14}O(p,pn) are 6.3 mb and 13.5 mb for DWIA and QTC, respectively. In the QTC cross section the transfer (p,d) reaction channel is included, which contributes about 3.3 mb. Without it the QTC knockout cross section amounts to 10.2 mb, which is still much larger than the cross section from the DWIA. The difference is attributed to stem from low-energy neutron core absorption. Note, the DWIA and QTC models have a good agreement for the momentum distributions of (p,pN) reaction at 420 MeV/nucleon [80]. For the study of the transfer channel, the QTC is performed with the outgoing channel coupled only to the deuteron ground state. This is equivalent to the DWBA, which has been introduced in Section 4.1. The d-^{13}O potential has been calculated with the Johnson-Soper prescription [107], in which the p-^{13}O and p-^{13}O folding potential at half of the kinetic energy of the deuteron was adopted. The obtained $\sigma_{\text{s.p.}}$ for the transfer reaction is 3(1) mb, which is translated into 11(3) mb with a SF of 3.4. The uncertainty has been estimated by using the JLM d-^{13}O potential and varying the interaction used for the deuteron wave function. The transfer (p,d) has not been considered for the DWIA channel. This is why the total cross section for the DWIA has been calculated by adding the single-particle cross section of the DWIA knockout and the transfer reaction channels with Eq. (1.6). The total cross section for QTC has been calculated directly from its single-particle cross section. The resulting cross sections are 34 mb and 50 mb for DWIA and QTC, respectively. This leads to reduction factors of $R_s = 0.49(7)$ and $R_s = 0.34(5)$.

The theoretical momentum distributions of ^{13}O from the DWIA+DWBA and QTC calculations are compared to experimental data in Fig. 5.1. The PMD of ^{13}O has a low-momentum tail and a sharp high-momentum cut off. The data are well reproduced by combining the contributions from the DWIA for the (p,pn) knockout and channel and the DWBA for the (p,d) transfer channel. The transfer channel contributes about ∼30 % to the neutron removal. As already discussed for theoretical DWIA calculations [52], the data supports the interpretation that the low-momentum tail originates from the attractive potential between the outgoing nucleons and ^{13}O. On the high-momentum side the (p,d) transfer channel creates a sharp edge. It arises from the two-body kinematics of the transfer reaction and its limit. The edge is in a region, which is kinematically not accessible for the (p,pn) knockout reaction and thus is a strong proof for a significant transfer contribution. It is also noticeable, that the high-momentum edge is much sharper than in the DWIA prediction with the phase-volume effect for the (p,pn) channel [52]. The QTC formalism treats the (p,d) transfer consistently with the (p,pn) and so it reproduces better the high-momentum side than the DWIA. Without the transfer channel the QTC high-momentum edge gets closer to the DWIA result as shown in Fig. 5.1 (d). However, the QTC is not able to reproduce the low-momentum tail as good as the DWIA. The reason might be the different treatment of the final state interaction in QTC, especially that the nucleon-residue interaction at low relative energy is not explicitly treated in the QTC formalism.

5.4. Context to other Nucleon Removal Results

For the first time, the PMD measured at a relatively high energy of $\sim$100 MeV/nucleon shows a distinctive contribution from the (p,d) transfer reaction. The transfer cross section is usually neglected at such a beam energy, since the momentum matching condition is not considered to be fulfilled [35]. The transfer reaction extracted here ($\sim$30 %) is comparable to that of the elastic removal mechanism in loosely-bound proton knockout reaction on a heavy-ion target at $\sim$100 MeV/nucleon [108, 109]. One-nucleon pickup cross sections have been measured around 60 MeV/nucleon with heavy-ion beams on ^{12}C or ^{9}Be target [110–113]. Here, the extracted one-neutron transfer cross section is much higher, which might be due to the momentum matching of the well-bound neutron. Further calculations at 300 MeV/nucleon show that the (p,d) transfer decreases to about 0.2 mb, which is negligible comparing to the contribution of the quasi-free (p,pn) knockout process [46, 79]. The (p,d) transfer contribution should thus be assessed for the neutron removal from the neutron-rich nucleus at intermediate energies, especially at energies below 100 MeV/nucleon.

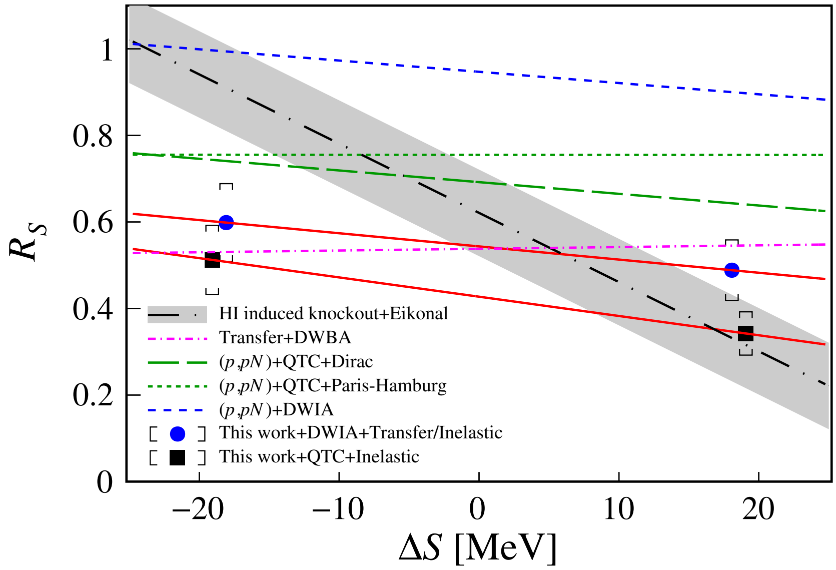

Figure 5.2.: Reduction factor R_s as a function of the proton-to-neutron separation energy asymmetry ΔS from the present work compared to trends fitted from light-ion-induced nucleon removal cross sections analysed under the eikonal approximation [36, 105, 106] (black two-dash line and grey shaded region), quasi-free (p,pN) knockout cross sections analysed with the DWIA [48, 114] (blue short dashed line) or QTC [83] (green dotted and long dashed lines) frameworks, and one-nucleon transfer cross section from Oxygen isotopes analysed within the DWBA framework [44] (purple dashed-dotted line). The blue dots and black squares show the data from the current work with the statistical and theoretical uncertainties. The correlated systematic uncertainties, mostly from target thickness, are given in square brackets. See Table 5.1 for the details. The data points are shifted by ± 0.5 MeV on the ΔS axis to avoid overlap. Note, that the inelastic scattering calculation did not consider collective states, which might contribute further to the proton removal cross section. The R_s would then be further reduced. Red solid lines are shown to guide the eyes.

The comparison from the experimental results with the theoretical calculation is illustrated by the reduction factor R_s as a function of the neutron-to-proton ratio in Fig. 5.2. The data from this work exhibits a slope of -0.0030(5)(5) MeV^{-1} for DWIA together with inelastic and transfer predictions and a slope of -0.0046(4)(7) MeV^{-1} when QTC and inelastic scattering are considered. Both slopes are slightly negative, however they are not compatible with the slope from light-ion induced nucleon removal measured at incident energies of ~70 MeV/nucleon-100 MeV/nucleon and analysed with the eikonal formalism and shell-model spectroscopic factors [36, 106]. When fitting a line through the light-ion induced nucleon removal data, one gets a slope of -0.016 MeV^{-1} and all R_s lie within a range of ± 0.1 of this slope (grey shaded area). In addition, low-energy one-nucleon transfer data analysed through the DWBA formalism with Woods-Saxon-based form factors and shell model spectroscopic factors have a slope of 0.0004(24)(12) MeV^{-1} [44]. In addition, quasifree-scattering on oxygen and nitrogen nuclei [46] analysed via the DWIA and QTC formalism is given. The slope from DWIA calculation is -0.0026(27) MeV^{-1}[48, 114], while the slope from QTC calculations exhibit slopes of -0.0027(14) MeV^{-1} and -0.00001(15) MeV^{-1} using the Dirac and Paris-Hamburg potential, respectively [83]. The slope of the data from this work is compatible to the slope from quasi-free scattering at higher incident energies. However, the R_s factor obtained in this work is systematically lower by ~25 % compared to quasi-free scattering and analysis.

Conclusion and Outlook

In this thesis a detailed study of the one-nucleon removal mechanism from the large separation-energy asymmetric nucleus ^{14}O ($\Delta S = \pm 18.55(1)$ MeV) at 94 MeV/nucleon using a proton target was presented. The measurement was performed at the SAMURAI experimental site at Radioactive Isotope Beam Factory of RIKEN, Japan. The $A-1$ residues were measured and identified in the focal plane of SAMURAI. Their momentum after the target was measured. The cross sections were determined to be 16.8(24) mb for neutron-removal and 10.7(16) mb for proton-removal. They were compared to the state-of-art (p,pN) reaction models, which are the distorted wave impulse approximation (DWIA) and quantum transfer to the continuum (QTC). Furthermore inelastic scattering and nucleon transfer calculations together with shell model spectroscopic factors are considered. Reductions factors of 0.51(8)-0.60(9) and 0.34(5)-0.49(7) were obtained for the loosely-bound proton and the deeply-bound neutron removal, respectively. A negative slope, calculated using the reduction factors with ΔS from the two measured data points, is observed, which is at tension with the one obtained from the eikonal analysis of light-ion-induced nucleon removal cross sections at incident energies of $\sim 70-100$ MeV/nucleon. The loosely-bound proton removal displays a symmetric parallel momentum distribution (PMD). The (p,p') inelastic excitation and the (p,2p) knockout reaction was found contributing almost equally for the loosely-bound proton removal. The asymmetric PMD for deeply-bound neutron removal was well reproduced by the DWIA (p,pn) calculation together with distorted-wave Born approximation (DWBA) (p,d) transfer reaction calculations. We observed a distinct contribution in the residue PMD from the (p,d) transfer reaction. The (p,d) transfer channel, that is usually neglected at beam energy around 100 MeV/nucleon, was found to contribute 30 % of the cross section.

The present work shows that the proton-induced nucleon removal from rare isotopes at energies of ~ 100 MeV/nucleon originates from several reaction mechanisms, including quasi-free scattering, inelastic scattering and transfer with similar contributions. It is expected that these contributions depend differently on the separation energy of the nucleon to be removed and the incident energy and should therefore be considered case by case. It would be of interest to investigate, how much these reaction mechanisms contribute significantly to nucleon removal when light-ion targets such as ^{9}Be and ^{12}C in this incident-energy regime are used. The findings of this work indicate that the R_s for loosely-bound nucleons removal with light-ion targets could be qualitatively explained by inelastic excitations of the projectile above the nucleon separation energy. These are not explicitly taken into account in the eikonal formalism of Ref. [36]. Furthermore, differences in the transverse momentum distributions of ^{13}O and ^{13}N have been shown in the acceptance section. However, due to time constraints they have no been pursued. It would be the next step to analyze the transverse momentum from these data. One could even go one step further and propose a full missing mass measurement to extract the momentum distribution with a higher precision by measuring the outgoing target like recoils.

Appendix

A. DAQ Lifetime

Table A.1.: Events of the DAQ lifetime correction for the *beam trigger* and *reaction trigger* for the runs 527 - 539 with the solid hydrogen target. The selected events for the residues ^{14}O, ^{13}O and ^{13}N are scaled by the respective ratio.

Run	N_{total} *beam trigger*	N_{gated} *beam trigger*	Ratio	N_{total} *reaction trigger*	N_{gated} *reaction trigger*	Ratio
527	63689784	34474800	0.54	8904997	6153110	0.69
528	34648141	18689000	0.54	4863869	3370286	0.69
529	34524376	18662600	0.54	4876905	3394831	0.7
530	34733980	18393700	0.53	5153686	3548876	0.69
531	34489846	18345500	0.53	5019647	3469964	0.69
532	35430759	18798100	0.52	5090638	3536886	0.69
533	33930379	17767300	0.52	4988414	3451423	0.69
534	33788463	17651100	0.52	4924841	3416121	0.69
535	34625960	17853500	0.51	5223146	3602164	0.69
536	35984360	18297500	0.51	5640994	3866917	0.69
537	34164870	17311200	0.51	5362593	3657367	0.68
538	28704426	14616300	0.51	4460270	3050034	0.68
539	34211638	17428000	0.51	5241897	3594672	0.69

Table A.2.: Events of the DAQ lifetime correction for the *beam trigger* and *reaction trigger* for the runs 540 - 551 with the solid hydrogen target. The selected events for the residues ^{14}O, ^{13}O and ^{13}N are scaled by the respective ratio.

Run	N_{total} *beam trigger*	N_{gated} *beam trigger*	Ratio	N_{total} *reaction trigger*	N_{gated} *reaction trigger*	Ratio
540	40461144	20585200	0.51	6281731	4300396	0.68
541	33535008	17185300	0.51	5214693	3583947	0.69
542	40310941	20539000	0.51	6408005	4369654	0.68
543	35020288	17683300	0.5	5647661	3801781	0.67
544	35020288	17632600	0.5	5754695	3821186	0.66
545	35504964	17601900	0.5	5631753	3754136	0.67
546	36966797	18569900	0.5	5977096	3937153	0.66
547	36734394	17978400	0.49	6162427	3994666	0.65
548	36236153	17821100	0.49	6061475	3957940	0.65
549	40140706	19860100	0.49	6669327	4339301	0.65
550	36370666	18112700	0.5	6116837	3972556	0.65
551	33745873	16468100	0.49	5890625	3770482	0.64

Table A.3.: Events of the DAQ lifetime correction for the *beam trigger* and *reaction trigger* for the runs without the solid hydrogen target. The selected events for the residues ^{14}O, ^{13}O and ^{13}N are scaled by the respective ratio.

Run	N_{total} *beam trigger*	N_{gated} *beam trigger*	Ratio	N_{total} *reaction trigger*	N_{gated} *reaction trigger*	Ratio
561	39657112	20011700	0.5	6429307	4269811	0.66
562	38853343	19657700	0.51	6150745	4109007	0.67
563	30263653	15380200	0.51	4743791	3179460	0.67
564	23764642	12106000	0.51	3720126	2495519	0.67
567	24931335	12612800	0.51	4020557	2669512	0.66
568	24017388	12043400	0.5	4005631	2647829	0.66
569	24709644	12413500	0.5	4140380	2738017	0.66
570	27130115	13767300	0.51	4523638	3010049	0.67
571	24494161	12328100	0.5	4099149	2688765	0.66
572	24264822	12212500	0.5	4072920	2674951	0.66
573	25564992	12879500	0.5	4297608	2816771	0.66
574	24504252	12249400	0.5	4085490	2663695	0.65

B. Target Thickness

Table B.1.: Momentum Peak position of the ^{14}O beam for the runs with solid hydrogen target

Run	Run Time [s]	Momentum Peak [MeV/c]
527	6452	6011
528	3586	6013
529	3570	6009
530	3619	6008
531	3580	6013
532	3692	6010
533	3587	6009
534	3574	6007
535	3696	6009
536	3908	6007
537	3655	6005
538	3256	6006
539	3670	6008
540	4336	6012
541	3642	6010
542	4361	6012
543	3693	6011
544	3624	6013
545	3614	6008
546	3702	6005
547	3640	6002
548	3617	6010
549	3980	6010
550	3625	6010
551	3326	6013

Table B.2.: Momentum Peak position of the ^{14}O beam for the runs without solid hydrogen target

Run	Run Time [s]	Momentum Peak [MeV/c]
561	4053	6052
562	3911	6047
563	3214	6049
564	2430	6063
567	2525	6065
568	2463	6063
569	2558	6062
570	2841	6067
571	2460	6064
572	2462	6062
573	2585	6060
574	2422	6057

C. Energyloss Water

Table C.1.: Mean value μ and standard deviation σ of the half gaussian water distribution applied for each run. The model indicates the procedure applied for the random generation of one water thickness value. The runs up to 551 are with the solid hydrogen target.

Runnumber	Model	μ [μm]	σ [μm]
527	static	265	150
528	static	267	158
529	static	278	152
530	static	275	172
531	static	266	147
532	static	277	153
533	static	275	155
534	static	281	160
535	static	275	167
536	static	271	184
537	static	276	197
538	static	275	191
539	static	282	183
540	static	266	152
541	static	274	159
542	static	273	161
543	static	268	151
544	static	265	161
545	static	277	164
546	static	287	174
547	dynamic	225	255
548	static	271	200
549	static	271	170
550	static	281	167
551	static	265	155

Table C.2.: Mean value μ and standard deviation σ of the half gaussian water distribution applied for each run. The model indicates the procedure applied for the random generation of one water thickness value. The runs starting from 561 and higher are without solid hydrogen target.

Runnumber	Model	μ [μm]	σ [μm]
561	dynamic	237	218
562	dynamic	228	258
563	dynamic	223	280
564	static	255	205
567	static	255	154
568	static	270	140
569	static	270	140
570	static	260	122
571	static	265	129
572	static	267	136
573	dynamic	222	197
574	dynamic	216	202

Bibliography

[1] B. Povh *et al.* *Particles and Nuclei*. 7. ed. Berlin: Springer, 2014.

[2] M. G. Mayer. “On Closed Shells in Nuclei. II”. In: *Phys. Rev.* 75(12) (1949).

[3] O. Haxel, J. H. D. Jensen, and H. E. Suess. “On the ”Magic Numbers” in Nuclear Structure”. In: *Phys. Rev.* 75(11) (1949).

[4] R. D. Woods and D. S. Saxon. “Diffuse Surface Optical Model for Nucleon-Nuclei Scattering”. In: *Phys. Rev.* 95(2) (1954).

[5] M. J. W. S. French J.B. and Halbert E.C. *Advances in Nuclear Physics*. Ed. by V. E. Baranger M. Boston: Springer, 1969.

[6] C. Bertulani and P. Danielewicz. *Introduction to Nuclear Reactions*. 2. ed. Boca Raton: Taylor Francis, 2021.

[7] A. Ozawa *et al.* “New Magic Number, $N = 16$, near the Neutron Drip Line”. In: *Phys. Rev. Lett.* 84(24) (2000).

[8] I. Talmi and I. Unna. “Order of Levels in the Shell Model and Spin of ^{11}Be”. In: *Phys. Rev. Lett.* 4(9) (1960).

[9] K. Tshoo *et al.* “$N = 16$ Spherical Shell Closure in ^{24}**O**”. In: *Phys. Rev. Lett.* 109(2) (2012).

[10] T. Otsuka *et al.* “Evolution of Nuclear Shells due to the Tensor Force”. In: *Phys. Rev. Lett.* 95(23) (2005).

[11] A. P. Zuker *et al.* “Nilsson-SU3 self-consistency in heavy $N = Z$ nuclei”. In: *Phys. Rev. C* 92(2) (2015).

[12] T. Otsuka and Y. Tsunoda. “The role of shell evolution in shape coexistence”. In: *J. Phys. G: Nucl. Part. Phys.* 43(2) (2016).

[13] T. Otsuka *et al.* “Evolution of shell structure in exotic nuclei”. In: *Rev. Mod. Phys.* 92(1) (2020).

[14] G. Hagen *et al.* “Continuum Effects and Three-Nucleon Forces in Neutron-Rich Oxygen Isotopes”. In: *Phys. Rev. Lett.* 108 (2012).

[15] E. Epelbaum, H.-W. Hammer, and Ulf-G. Meißner. “Modern theory of nuclear forces”. In: *Rev. Mod. Phys.* 81(4) (2009).

[16] E. Epelbaum. *Nuclear forces from chiral effective field theory: a primer*. 2010.

[17] R. Machleidt and D.R. Entem. “Chiral effective field theory and nuclear forces”. In: *Phys. Rep.* 503(1) (2011).

[18] B. R. Barrett, P. Navrátil, and J. P. Vary. “Ab initio no core shell model”. In: *Prog. Part. Nucl. Phys.* 69 (2013).

[19] A. Gezerlis *et al.* “Quantum Monte Carlo Calculations with Chiral Effective Field Theory Interactions”. In: *Phys. Rev. Lett.* 111(3) (2013).

[20] J. Carlson *et al.* “Quantum Monte Carlo methods for nuclear physics”. In: *Rev. Mod. Phys.* 87(3) (2015).

[21] W.H. Dickhoff and C. Barbieri. “Self-consistent Green’s function method for nuclei and nuclear matter”. In: *Prog. Part. Nucl. Phys.* 52(2) (2004).

[22] M. Goméz. “A Transfer to Continuum formalism for the study of (p,pn) and (p,2p) reactions on unstable nuclei”. PhD thesis. Universidad de Sevilla, 2018.

[23] A. Navin *et al.* “Direct Evidence for the Breakdown of the $N = 8$ Shell Closure in ^{12}Be”. In: *Phys. Rev. Lett.* 85(2) (2000).

[24] C. A. Bertulani and C. De Conti. “Pauli blocking and medium effects in nucleon knockout reactions”. In: *Phys. Rev. C* 81(6) (2010).

[25] T. de Forest Jr. and J.D. Walecka. “Electron scattering and nuclear structure”. In: *Adv. Phys.* 15(57) (1966).

[26] G. Jacob and Th. A. J. Maris. “Quasi-Free Scattering and Nuclear Structure. II.” In: *Rev. Mod. Phys.* 45(1) (1973).

[27] Toshimi S. and Haik S. “Prospects for electron scattering on unstable, exotic nuclei”. In: *Prog. Part. Nucl. Phys.* 96 (2017).

[28] T. Duguet and G. Hagen. “Ab initio approach to effective single-particle energies in doubly closed shell nuclei”. In: *Phys. Rev. C* 85(3) (2012).

[29] Michel Baranger. “A definition of the single-nucleon potential”. In: *Nucl. Phys. A* 149(2) (1970).

[30] L. Lapikas. “Quasi-elastic electron scattering off nuclei”. In: *Nucl. Phys. A* 553 (1993). Ed. by R. Bock *et al.*

[31] O. Benhar, A. Fabrocini, and S. Fantoni. “Occupation probabilities and hole-state strengths in nuclear matter”. In: *Phys. Rev. C* 41(1) (1990).

[32] T. Wakasa, K. Ogata, and T. Noro. “Proton-induced knockout reactions with polarized and unpolarized beams”. In: *Prog. Part. Nucl. Phys.* 96 (2017).

[33] A. Obertelli *et al.* “MINOS: A vertex tracker coupled to a thick hydrogen liquid-target for in-beam spectroscopy of exotic nuclei”. In: *Eur. Phys. J. A* 50(8) (2014).

[34] H. N. Liu *et al. STRASSE: A silicon tracker for quasi free scattering measurement at RIBF*. In Progress.

[35] T. Aumann *et al.* “Quenching of single-particle strength from direct reactions with stable and rare-isotope beams”. In: *Prog. Part. Nucl. Phys.* 118 (2021).

[36] J. A. Tostevin and A. Gade. “Updated systematics of intermediate-energy single-nucleon removal cross sections”. In: *Phys. Rev. C* 103(5) (2021).

[37] T. Aumann. “Reaction with fast radioactive beams of neutron-rich nuclei”. In: *Eur. Phys. J. A* 26 (2005).

[38] J. P. Schiffer *et al.* “Nuclear Structure Relevant to Neutrinoless Double β Decay: ^{76}Ge and ^{76}Se”. In: *Phys. Rev. Lett.* 100(11) (2008).

[39] Jenny Lee *et al.* “Neutron-Proton Asymmetry Dependence of Spectroscopic Factors in Ar Isotopes”. In: *Phys. Rev. Lett.* 104(11) (2010).

[40] F. M. Nunes, A. Deltuva, and June Hong. “Improved description of $^{34,36,46}\mathrm{Ar}(p,d)$ transfer reactions”. In: *Phys. Rev. C* 83(3) (2011).

[41] A. Gade *et al.* “Reduced Occupancy of the Deeply Bound $0d_{5/2}$ Neutron State in ^{32}Ar”. In: *Phys. Rev. Lett.* 93(4) (2004).

[42] A. Gade *et al.* “One-neutron knockout reactions on proton-rich nuclei with $N = 16$”. In: *Phys. Rev. C* 69(3) (2004).

[43] A. Gade *et al.* “Knockout from $^{46}\mathrm{Ar} : \ell = 3$ neutron removal and deviations from eikonal theory”. In: *Phys. Rev. C* 71(5) (2005).

[44] F. Flavigny *et al.* “Limited Asymmetry Dependence of Correlations from Single Nucleon Transfer”. In: *Phys. Rev. Lett.* 110(12) (2013).

[45] V. Panin *et al.* In: *Phys. Lett. B* 753 (2016).

[46] L. Atar *et al.* “Quasifree $(p, 2p)$ Reactions on Oxygen Isotopes: Observation of Isospin Independence of the Reduced Single-Particle Strength”. In: *Phys. Rev. Lett.* 120(5) (2018).

[47] P. Díaz Fernández *et al.* “Quasifree (p,pN) scattering of light neutron-rich nuclei near $N = 14$”. In: *Phys. Rev. C* 97(2) (2018).

[48] S. Kawase *et al.* “Exclusive quasi-free proton knockout from oxygen isotopes at intermediate energies”. In: *Prog. Theor. Exp. Phys.* 2018(2) (2018).

[49] M. Leuschner *et al.* “Quasielastic proton knockout from ^{16}O”. In: *Phys. Rev. C* 49(2) (1994).

[50] Z. Y. Sun *et al.* “Knockout reactions from ^{14}O at 305 MeV/nucleon”. In: *Phys. Rev. C* 90(3) (2014).

[51] F. Flavigny *et al.* “Nonsudden Limits of Heavy-Ion Induced Knockout Reactions”. In: *Phys. Rev. Lett.* 108 (2012).

[52] Kazuyuki Ogata, Kazuki Yoshida, and Kosho Minomo. “Asymmetry of the parallel momentum distribution of (p,pN) reaction residues”. In: *Phys. Rev. C* 92(3) (2015).

[53] F.G. Kondev *et al.* “The NUBASE2020 evaluation of nuclear physics properties *”. In: *Chin. Phys. C* 45(3) (2021).

[54] H. Okuno, N. Fukunishi, and O. Kamigaito. “Progress of RIBF accelerators”. In: *Prog. Theor. Exp. Phys.* 2012(1) (2012).

[55] Yasushige Y. “The RIKEN RI Beam Factory Project: A status report”. In: *Nucl. Instrum. Methods Phys. Res. B* 261(1) (2007).

[56] BigRIPS Information. URL: `https://ribf.riken.jp/BigRIPSInfo/` (visited on 05/12/2022).

[57] J.P. Dufour *et al.* “Projectile fragments isotopic separation: Application to the lise spectrometer at GANIL”. In: *Nucl. Instrum. Methods Phys. Res. A* 248(2) (1986).

[58] K.-H. Schmidt *et al.* “The momentum-loss achromat — A new method for the isotopical separation of relativistic heavy ions”. In: *Nucl. Instrum. Methods Phys. Res. A* 260(2) (1987).

[59] T. Kobayashi *et al.* “SAMURAI spectrometer for RI beam experiments”. In: *Nucl. Instrum. Methods Phys. Res. B* 317 (2013).

[60] Y. Matsuda *et al.* “Large, thin solid hydrogen target using para-H2”. In: *Nucl. Instrum. Methods Phys. Res. A* 643(1) (2011).

[61] Glenn F. Knoll. *Radiation detection and measurement*. 4. ed. New York: Wiley, 2010.

[62] W.R. Leo. *Techniques for Nuclear and Particle Physics Experiments*. 2. ed. Heidelberg: Springer Berlin, 1994.

[63] H. Geissel *et al.* “Experimental studies of heavy-ion slowing down in matter”. In: *Nucl. Instrum. Methods Phys. Res. B* 195(1) (2002).

[64] O.B. Tarasov and D. Bazin. “LISE++: Exotic beam production with fragment separators and their design”. In: *Nucl. Instrum. Methods Phys. Res. B* 376 (2016).

[65] Y. Kondo and Y. Kubota. Private communication. (2022).

[66] Titech Information. URL: `http://be.nucl.ap.titech.ac.jp/~nebula/simulator.php` (visited on 05/22/2022).

[67] S. Agostinelli *et al.* “Geant4—a simulation toolkit”. In: *Nucl. Instrum. Methods Phys. Res. A* 506(3) (2003).

[68] Rene Brun and Fons Rademakers. “ROOT — An object oriented data analysis framework”. In: *Nucl. Instrum. Methods Phys. Res. A* 389(1) (1997).

[69] C. Holm. URL: `https://root.cern.ch/doc/master/classTMultiDimFit.html` (visited on 05/22/2022).

[70] R.M. Sternheimer, M.J. Berger, and S.M. Seltzer. “Density effect for the ionization loss of charged particles in various substances”. In: *At. Data Nucl. Data Tables* 30(2) (1984).

[71] T.J. Gooding and H.G. Pugh. “The response of plastic scintillators to high-energy particles”. In: *Nucl. Instrum. Methods Phys. Res.* 7.2 (1960), pp. 189–192. ISSN: 0029-554X.

[72] N. Fukuda *et al.* “Identification and separation of radioactive isotope beams by the BigRIPS separator at the RIKEN RI Beam Factory”. In: *Nucl. Instrum. Methods Phys. Res. B* 317 (2013).

[73] K. Ogata. Private communication. (2021).

[74] A. Boudard *et al.* “Intranuclear cascade model for a comprehensive description of spallation reaction data”. In: *Phys. Rev. C* 66(4) (2002).

[75] Y. Matsuda. Private communication. (2021).

[76] A. Obertelli. “Nuclear structure from direct reactions with rare isotopes: observables, methods and highlights”. In: *Eur. Phys. J. Plus* 131(9) (2016).

[77] N. S. Chant and P. G. Roos. “Distorted-wave impulse-approximation calculations for quasifree cluster knockout reactions”. In: *Phys. Rev. C* 15(1) (1977).

[78] N. S. Chant and P. G. Roos. “Spin orbit effects in quasifree knockout reactions”. In: *Phys. Rev. C* 27(3) (1983).

[79] T. Aumann, C. A. Bertulani, and J. Ryckebusch. “Quasifree $(p,2p)$ and (p,pn) reactions with unstable nuclei”. In: *Phys. Rev. C* 88(6) (2013).

[80] K. Yoshida *et al.* “Benchmarking theoretical formalisms for (p,pn) reactions: The ^{15}C$(p,pn)^{14}$C case”. In: *Phys. Rev. C* 97(2) (2018).

[81] N. Austern *et al.* “Continuum-discretized coupled-channels calculations for three-body models of deuteron-nucleus reactions”. In: *Phys. Rep.* 154(3) (1987).

[82] A. M. Moro. “Three-body model for the analysis of quasifree scattering reactions in inverse kinematics”. In: *Phys. Rev. C* 92(4) (2015).

[83] M. Gómez-Ramos and A.M. Moro. “Binding-energy independence of reduced spectroscopic strengths derived from (p,2p) and (p,pn) reactions with nitrogen and oxygen isotopes”. In: *Phys. Lett. B* 785 (2018).

[84] S. Chen *et al.* “Quasifree Neutron Knockout from ^{54}Ca Corroborates Arising $N = 34$ Neutron Magic Number”. In: *Phys. Rev. Lett.* 123(14) (2019).

[85] Y.L. Sun *et al.* “Restoration of the natural E(1/21+) - E(3/21+) energy splitting in odd-K isotopes towards N = 40”. In: *Phys. Lett. B* 802 (2020).

[86] F. Browne *et al.* “Pairing Forces Govern Population of Doubly Magic ^{54}Ca from Direct Reactions”. In: *Phys. Rev. Lett.* 126(25) (2021).

[87] Cenxi Yuan *et al.* “Shell-model study of boron, carbon, nitrogen, and oxygen isotopes with a monopole-based universal interaction”. In: *Phys. Rev. C* 85(6) (2012).

[88] Noritaka S. *et al.* “Thick-restart block Lanczos method for large-scale shell-model calculations”. In: *Comput. Phys. Commun.* 244 (2019).

[89] B. A. Brown *et al.* In: *MSU-NSCL report no. 1289* (2004).

[90] E. K. Warburton and B. A. Brown. “Effective interactions for the 0p1s0d nuclear shell-model space”. In: *Phys. Rev. C* 46(3) (1992).

[91] M. A. Franey and W. G. Love. “Nucleon-nucleon t-matrix interaction for scattering at intermediate energies”. In: *Phys. Rev. C* 31(2) (1985).

[92] F. Perey and B. Buck. “A non-local potential model for the scattering of neutrons by nuclei”. In: *Nuclear Physics* 32 (1962), pp. 353–380. ISSN: 0029-5582.

[93] V. G. J. Stoks *et al.* “Construction of high-quality NN potential models”. In: *Phys. Rev. C* 49(6) (1994).

[94] J.-P. Jeukenne, A. Lejeune, and C. Mahaux. “Optical-model potential in finite nuclei from Reid’s hard core interaction”. In: *Phys. Rev. C* 16(1) (1977).

[95] H. Sakaguchi *et al.* “Elastic scattering of 65 MeV polarized protons”. In: *Phys. Rev. C* 26(3) (1982).

[96] C. A. Bertulani, A. Idini, and C. Barbieri. “Examination of the sensitivity of quasifree reactions to details of the bound-state overlap functions”. In: *Phys. Rev. C* 104(6) (2021).

[97] Jianguo Li, Carlos A. Bertulani, and Furong Xu. “Nuclear spectroscopy with heavy ion nucleon knockout and (p,2p) reactions”. In: *Phys. Rev. C* 105(2) (2022).

[98] R. Schaeffer and J. Raynal. “Computer program DWBA70”. In: (1970).

[99] A.J. Koning and J.P. Delaroche. “Local and global nucleon optical models from 1 keV to 200 MeV”. In: *Nucl. Phys. A* 713(3) (2003).

[100] J. R. Comfort *et al.* “Analyzing powers for the ^{12}C($\vec{p}$,p')^{12}C reaction at 120 MeV and a test of the distorted-wave impulse approximation”. In: *Phys. Rev. C* 24(5) (1981).

[101] R. J. Charity *et al.* “Invariant-mass spectroscopy of ^{14}O excited states”. In: *Phys. Rev. C* 100(6) (2019).

[102] G. Bertsch *et al.* “Interactions for inelastic scattering derived from realistic potentials”. In: *Nuclear Physics A* 284(3) (1977).

[103] Y. Sun. *Microscopic DWBA cross section for the ^{14}O(p,p’)^{14}O* reaction at ∼100 MeV/nucleon*. Unpublished.

[104] A. E. L. Dieperink and T. de Forest. “Center-of-mass effects in single-nucleon knock-out reactions”. In: *Phys. Rev. C* 10(2) (1974).

[105] A. Gade *et al.* “Reduction of spectroscopic strength: Weakly-bound and strongly-bound single-particle states studied using one-nucleon knockout reactions”. In: *Phys. Rev. C* 77(4) (2008).

[106] J. A. Tostevin and A. Gade. “Systematics of intermediate-energy single-nucleon removal cross sections”. In: *Phys. Rev. C* 90(5) (2014).

[107] R. C. Johnson and P. J. R. Soper. “Contribution of Deuteron Breakup Channels to Deuteron Stripping and Elastic Scattering”. In: *Phys. Rev. C* 1(3) (1970).

[108] D. Bazin *et al.* “Mechanisms in Knockout Reactions”. In: *Phys. Rev. Lett.* 102(23) (2009).

[109] K. Wimmer *et al.* “Elastic breakup cross sections of well-bound nucleons”. In: *Phys. Rev. C* 90(6) (2014).

[110] A. Gade *et al.* “Inverse-kinematics one-proton pickup with intermediate-energy beams: The ^{9}Be (^{20}Ne,^{21}Na $+ \gamma)X$ reaction”. In: *Phys. Rev. C* 76(6) (2007).

[111] A. Gade *et al.* “In-Beam γ-Ray Spectroscopy of Very Neutron-Rich Nuclei: Excited States in ^{46}**S** and ^{48}Ar”. In: *Phys. Rev. Lett.* 102(18) (2009).

[112] S. McDaniel *et al.* “Intermediate-energy inverse-kinematics one-proton pickup reactions on neutron-deficient fp-shell nuclei”. In: *Phys. Rev. C* 85(1) (2012).

[113] A. Gade *et al.* “Single-particle structure at $N = 29$: The structure of ^{47}Ar and first spectroscopy of ^{45}S”. In: *Phys. Rev. C* 93(5) (2016).

[114] N. T. T. Phuc, K. Yoshida, and K. Ogata. “Toward a reliable description of (p, pN) reactions in the distorted-wave impulse approximation”. In: *Phys. Rev. C* 100(6) (2019).